MICROSTRUCTURE ANALYSIS OF AN AS-SERVICED FIRST STAGE LAND BASED GAS TURBINE BLADE

by

Mehmet Güçlü Akkoyun

B.S., Mechanical Engineering, Boğaziçi University, 2012

Submitted to the Institute for Graduate Studies in
Science and Engineering in partial fulfillment of
the requirements for the degree of
Master of Science

Graduate Program in Mechanical Engineering
Boğaziçi University

2016

ACKNOWLEDGEMENTS

Firstly, I would like to express my thanks to my family members, my mother, my father, and my brother for their support and help in my life. They have always helped me during this study.

I would like to thank my thesis supervisor Assoc. Prof. Ercan Balıkçı for his valuable advices, guidance, support, and patience during this study. It was a very nice experience to work with him.

I would like to thank the other members of my thesis defense jury, Prof. Cevat Sarıoğlu, and Assoc. Prof. Nuri Ersoy, for their advices to improve this study.

Also, I thank Dr. Bilge Uluocak for her support during the scanning electron microscope studies.

Financial support for this study by BAP 6328 project is gratefully acknowledged.

ABSTRACT

MICROSTRUCTURE ANALYSIS OF AN AS-SERVICED FIRST STAGE LAND BASED GAS TURBINE BLADE

Superalloys are high temperature materials, and they are used in many industries. Gas turbine industry, aircrafts, and space vehicles are the important industries in which superalloys are used. They are preferred because of their superior properties like high temperature strength, good ductility, and high creep resistance. IN738LC is a polycrystalline nickel base superalloy which is widely used in land based gas turbines. It has a good creep strength and hot corrosion resistance.

In this study, a polycrystalline IN738LC turbine blade which has worked 80000 hours at the first stage of the hot section in an electricity producing natural gas turbine is analyzed. Specimens from the root, middle, and tip sections both on the suction and pressure sides of the blade are extracted in order to analyze the grain size and morphology variations in macro scale, and the precipitate size and morphology variations in nano scale. As a result, high/low stress/temperature regions are estimated by using these data.

Analysis shows that the base metal of the blade is coated firstly by a NiCoCrAlY layer, then a NiCrAlY layer. The final layer is a thermal barrier coating. Grain size in the cold surfaces is larger than that in the hot surfaces. Since the grain growth is aided by temperature, a larger grain size is expected in the hot surfaces. This seemingly contradictory result is attributed to recrystallization in hot surfaces. Precipitate size in the hot surfaces is larger than that in the cold surfaces. Raft formation is observed in both the suction and pressure sides of the middle and trailing edge positions, and in the stagnation point in the tip section. In the middle section, raft is observed in both the suction and pressure sides of the leading edge and middle positions, and in the stagnation point. Precipitate size in the root section is smaller than that in the middle and tip sections. Very fine precipitates have been observed in cold surfaces of the root section.

ÖZET

KULLANILMIŞ BİR BİRİNCİ KADEME EKEKTRİK ÜRETEN GAZ TÜRBİNİ BIÇAĞININ MİKROYAPI ANALİZİ

Süperalaşımlar yüksek sıcaklık malzemeleridir ve birçok endüstride kullanılırlar. Gaz türbini endüstrisi, uçaklar ve uzay araçları, süperalaşımların kullanıldığı önemli endüstrilerdir. Süperalaşımlar, yüksek sıcaklık mukavemeti, iyi süneklik ve yüksek sürünme dayanımı gibi üstün özellikleri dolayısıyla tercih edilirler. IN738LC elektrik üreten gaz türbinlerinde sıkça kullanılan çok taneli nikel esaslı bir süperalaşımdır. Yüksek sürünme mukavemetine ve sıcak korozyon dayanımına sahiptir.

Bu çalışmada, elektrik üreten bir doğal gaz santralindeki sıcak kısım birinci kademesinde 80000 saat çalışmış çok taneli bir IN738LC türbin bıçağı analiz edilmiştir. Makro düzeyde tane yapısını ve morfolojisini, nano düzeyde ise çökelti yapısını ve morfolojisini analiz etmek için bıçağın uç, orta, ve kök kesitlerinin hem emme hem de basınç taraflarından numuneler çıkarılmıştır. Sonuç olarak, bu bilgilerin kullanılmasıyla yüksek/düşük stres/sıcaklık bölgeleri tahmin edilmiştir.

Analiz, bıçağın ana metalinin önce bir NiCoCrAlY tabakasıyla, sonra da bir NiCrAlY tabakasıyla kaplandığını gösteriyor. Son tabaka ise bir ısıl bariyer kaplamasıdır. Tane boyutu soğuk yüzeylerde sıcak yüzeylerdekinden daha büyüktür. Sıcaklık, tanelerin büyümesini sağladığı için sıcak yüzeylerde daha büyük bir tane boyutu olması beklenir. Beklentiye zıt görülen bu sonuç sıcak yüzeylerde yeniden taneleşmeye bağlanabilir. Sıcak yüzeylerdeki çökelti boyutu soğuk yüzeydekilere göre daha büyüktür. Uç kesitte; orta pozisyonun ve kuyruk pozisyonunun hem emme hem basınç tarafında, ve durma noktasında yönelme gözlemlenmiştir. Orta kesitte; ön ve orta pozisyonların hem emme hem basınç tarafında, ve durma noktasında yönelme gözlemlenmiştir. Kök kesitinde çökelti boyutu orta ve uç kesittekilere göre daha küçüktür. Kök kesitinin soğuk yüzeylerinde çok küçük çökeltiler gözlemlenmiştir.

TABLE OF CONTENTS

ACKNOWLEDGEMENTS iii
ABSTRACT iv
ÖZET v
LIST OF FIGURES viii
LIST OF TABLES xv
LIST OF SYMBOLS xvi
LIST OF ACRONYMS/ABBREVIATIONS xvii
1. INTRODUCTION 1
1.1. High Temperature Materials and Superalloys 1
1.2. Turbine Blades 1
1.3. Types of Superalloys 3
1.3.1. Nickel base superalloys 3
1.3.2. Iron base superalloys 3
1.3.3. Cobalt base superalloys 4
1.4. Phases in Superalloys 4
1.4.1. Gamma (γ) Phase 4
1.4.2. Precipitate Phase 4
1.4.3. Carbides 5
1.4.4. Borides 6
1.4.5. Topologically Close Packed (TCP) Phases 6
1.5. Nucleation and Growth of Precipitates 6
1.6. Rafting 7
1.7. IN738LC Nickel Based Superalloy 8
1.8. Objectives 9
2. EXPERIMENTAL 10
3. RESULTS 16
3.1. The Coatings 16
3.2. Grain Size and Morphology 41
3.2.1. Grain Size 41

3.2.2. Grain Morphology 45
3.2.2.1. B80-SP-TT (tip section trailing edge) 46
3.2.2.2. B80-SP-TM (tip section middle position) 47
3.2.2.3. B80-SPO-TL (tip section leading edge) 48
3.2.2.4. B80-SP-MT (middle section trailing edge) 50
3.2.2.5. B80-SP-MM (middle section middle position) 52
3.2.2.6. B80-SPO-ML (middle section leading edge) 54
3.2.2.7. B80-SP-RT (root section trailing edge) 56
3.2.2.8. B80-SP-RM (root section middle position) 57
3.2.2.9. B80-SPO-RL (root section leading edge) 62
3.2.2.10. Firtree Specimen 63
3.3. Precipitate Size and Morphology 65
3.3.1. Precipitate Size 65
3.3.2. Precipitate Morphology 70
3.3.3. Precipitate Area Fraction 76
4. DISCUSSION 78
4.1. The Coatings 78
4.2. Grain Size and Morphology 80
4.3. Precipitate Size and Morphology 85
5. CONCLUSION 91
6. FUTURE WORK 92
REFERENCES 93

LIST OF FIGURES

Figure 1.1. $L1_2$ Crystal Structure 5

Figure 2.1. Specimen positions in the pressure side of the served turbine blade . 10

Figure 2.2. Specimen positions in the suction side of the served turbine blade . . 11

Figure 2.3. Trailing edge samples (B80-SP-RT) 12

Figure 2.4. Middle position samples (B80-SP-RM) 12

Figure 2.5. Leading edge samples (B80-SPO-RL) 12

Figure 2.6. Pressure side trailing edge (PT) specimens. Analyzed surfaces are shaded dark 13

Figure 2.7. Pressure side middle position (PM) specimens. Analyzed surfaces are shaded dark 13

Figure 2.8. Leading edge (PL, OL, SL) specimens. Analyzed surfaces are shaded dark 14

Figure 2.9. Representative mount for root section trailing edge (RT) specimens and their notations 15

Figure 3.1. Coating layers available in the blade 16

Figure 3.2. Layer thicknesses in SPO-TL (tip section, leading edge) position . . . 17

Figure 3.3. Coatings in SPO-TL (tip section, leading edge) position 18

Figure 3.4. Coatings in SPO-ML (middle section, leading edge) position 19

Figure 3.5. Coatings in SPO-RL (root section, leading edge) position 20

Figure 3.6. EDS analysis spots shown along the white arrow extending from the TBC to the cooling channel in the suction side, root section, leading edge, z surface specimen (B80SRLZ) 21

Figure 3.7. SEM photos of the TBC (1-3), first (4-6), second (7-14), third (15-17) coatings and the beginning of the fourth coating. The photo on the left is taken before precipitate etching and the photo on the right is taken after precipitate etching 23

Figure 3.8. SEM photo of the TBC and first coating after the precipitate etchant applied 24

Figure 3.9. SEM photo of the first and second coatings before the precipitate etchant applied 24

Figure 3.10. SEM photo of the second coating after the precipitate etchant applied 25

Figure 3.11. SEM photo of the boundary between the second and third coatings after precipitate etching. Porosity is visible along the boundary 25

Figure 3.12. SEM photo of the boundary between the third and fourth coatings after the precipitate etchant applied 26

Figure 3.13. SEM photo of the cooling channel surface before the precipitate etchant applied 27

Figure 3.14. Precipitate free region close to the cooling channel surface after the precipitate etchant applied 27

Figure 3.15. SEM photo of the boundary between the fourth coating and the base metal after the precipitate etchant applied. Base metal is seen below the scale bar 28

Figure 3.16. Coatings in the suction side root section leading edge z surface specimen (B80SRLZ) 28

Figure 3.17. SEM photos of the coatings and the metal after precipitate etching . 29

Figure 3.18. Weight percent of elements Ni, Co, Al, and Cr 31

Figure 3.19. Weight percent of elements Ta, Ti, Mo, and W 32

Figure 3.20. Weight percent of elements Y, Mn, Nb, Hf, and Zr 33

Figure 3.21. Weight percent of elements C, B, and O 34

Figure 3.22. Atomic percent of elements Ni, Co, Al, and Cr 35

Figure 3.23. Atomic percent of elements Ta, Ti, Mo, and W 36

Figure 3.24. Atomic percent of elements Y, Mn, Nb, Hf, and Zr 37

Figure 3.25. Atomic percent of elements C, B, and O 38

Figure 3.26. Grain size for the trailing edge 42

Figure 3.27. Grain size for the middle position 43

Figure 3.28. Grain size for the leading edge 43

Figure 3.29. Grain size for the tip section 44

Figure 3.30. Grain size for the middle section 44

Figure 3.31. Grain size for the root section 45

Figure 3.32. Grain morphology in PTT (Pressure side Tip section Trailing edge), a) cold surface, b) hot surface, c) z surface, d) side surface far from trailing edge, and e) side surface close to trailing edge specimens . . 46

Figure 3.33. Grain morphology in STT (Suction side Tip section Trailing edge), a) cold surface, b) hot surface, c) z surface, d) side surface far from trailing edge, and e) side surface close to trailing edge specimens . . 47

Figure 3.34. Grain morphology in PTM (Pressure side Tip section Middle position), a) cold surface, b) hot surface, c) z surface, and d) side surface specimens 48

Figure 3.35. Grain morphology in STM (Suction side Tip section Middle position), a) cold surface, b) hot surface, c) z surface, and d) side surface specimens 49

Figure 3.36. Grain morphology in PTL (Pressure side Tip section Leading edge), a) cold surface, b) hot surface, and c) z surface specimens 50

Figure 3.37. Grain morphology in STL (Suction side Tip section Leading edge), a) cold surface, b) hot surface, and c) z surface specimens 51

Figure 3.38. Grain morphology in OTL (stagnation point Tip section Leading edge), a) cold surface, b) hot surface, and c) z surface specimens . . . 52

Figure 3.39. Grain morphology in PMT (Pressure side Middle section Trailing edge), a) cold surface, b) hot surface, c) z surface, d) side surface far from trailing edge, and e) side surface close to trailing edge specimens 53

Figure 3.40. Grain morphology in SMT (Suction side Middle section Trailing edge), a) cold surface, b) hot surface, c) z surface, d) side surface far from trailing edge, and e) side surface close to trailing edge specimens 54

Figure 3.41. Grain morphology in PMM (Pressure side Middle section Middle position), a) cold surface, b) hot surface, c) z surface, and d) side surface specimens 55

Figure 3.42. Grain morphology in SMM (Suction side Middle section Middle position), a) cold surface, b) hot surface, c) z surface, and d) side surface specimens 56

Figure 3.43. Grain morphology in PML (Pressure side Middle section Leading edge), a) cold surface, b) hot surface, and c) z surface specimens . . . 57

Figure 3.44. Grain morphology in SML (Suction side Middle section Leading edge), a) cold surface, b) hot surface, and c) z surface specimens . . . 58

Figure 3.45. Grain morphology in OML (stagnation point Middle section Leading edge), a) cold surface, b) hot surface, and c) z surface specimens . . . 58

Figure 3.46. Grain morphology in PRT (Pressure side Root section Trailing edge), a) cold surface, b) hot surface, c) z surface, d) side surface far from trailing edge, and e) side surface close to trailing edge specimens . . 59

Figure 3.47. Grain morphology in SRT (Suction side Root section Trailing edge), a) cold surface, b) hot surface, c) z surface, d) side surface far from trailing edge, and e) side surface close to trailing edge specimens . . 59

Figure 3.48. Grain morphology in PRM (Pressure side Root section Middle position), a) cold surface, b) hot surface, c) z surface, and d) side surface specimens 60

Figure 3.49. Grain morphology in SRM (Suction side Root section Middle position), a) cold surface, b) hot surface, c) z surface, and d) side surface specimens 61

Figure 3.50. Grain morphology in PRL (Pressure side Root section Leading edge), a) cold surface, b) hot surface, and c) z surface specimens 62

Figure 3.51. Grain morphology in SRL (Suction side Root section Leading edge), a) cold surface, b) hot surface, and c) z surface specimens 63

Figure 3.52. Grain morphology in ORL (stagnation point Root section Leading edge), a) cold surface, b) hot surface, and c) z surface specimens . . 64

Figure 3.53. Grain morphology in firtree specimen 64

Figure 3.54. Precipitate size for the trailing edge position 66

Figure 3.55. Precipitate size for the middle position 67

Figure 3.56. Precipitate size for the leading edge position 67

Figure 3.57. Precipitate size for specimens in the tip section 68

Figure 3.58. Precipitate size for specimens in the middle section 69

Figure 3.59. Precipitate size for specimens in the root section 69

Figure 3.60. Precipitate size for specimens in the tip, middle, and root sections . 70

Figure 3.61. Precipitate microstructure in the tip section specimens 72

Figure 3.62. Precipitate microstructure in the middle section specimens 73

Figure 3.63. Precipitate microstructure in the root section specimens 74

Figure 3.64. Formation of very fine precipitates in suction side, root section, trailing edge, cold surface 75

Figure 3.65. Formation of very fine precipitates in suction side, root section, trailing edge, hot surface 75

Figure 3.66. Microstructure in pressure side, root section, trailing edge, outer side surface specimen 76

Figure 3.67. Microstructure in the firtree specimen 76

Figure 3.68. Precipitate area fraction vs. position 77

Figure 4.1. The cross section of the unused blade for the pressure side tip section 78

Figure 4.2. Base metal thickness in the pressure side tip section leading edge position for the unused blade 79

Figure 4.3. Recrystallization in the pressure side, tip section, middle position specimen for the used blade. Recrystallized grains are shown with white arrows 83

Figure 4.4. Microstructure of the coating on the base metal in the stagnation point tip section 88

Figure 4.5. Microstructure of the coating on the base metal in the stagnation point middle section 88

Figure 4.6. Precipitate size distribution in the pressure side root section leading edge cold surface specimen 89

Figure 4.7. Precipitate morphology in the virgin blade 90

LIST OF TABLES

Table 1.1. Elements present in IN738LC superalloy 8

Table 3.1. EDS analysis spots in Figure 3.6 22

Table 3.2. Element weight percent vs. position 39

Table 3.3. Element atomic percent vs. position 40

Table 3.4. Average grain size in microns 41

Table 3.5. Average precipitate diameter (nm) vs. position 65

Table 3.6. Precipitate area fraction vs. position 77

Table 4.1. The grain size values for the used and unused blades in the pressure side tip section 84

Table 4.2. Thickness of the base metal in millimeters 84

Table 4.3. Precipitate morphology on hot surface 86

Table 4.4. Precipitate morphology on cold surface 87

LIST OF SYMBOLS

a	Matrix lattice parameter
a’	Precipitate lattice parameter
k	Rate constant
r_0	Initial average radius
r_t	The radius at time *t*
t	Time
T_m	Melting temperature
T_{op}	Operation temperature
α	Primary phase
δ	Lattice misfit

LIST OF ACRONYMS/ABBREVIATIONS

ASTM	American Society for Testing and Materials
EDM	Electrical discharge machine
EDS/EDAX	Energy dispersive X-ray spectroscopy
ESEM	Environmental
et al.	And others
FCC	Face centered cubic
FEG	Field emission gun
LE	Leading edge
LSW	Lifshitz, Slyozof, and Wagner
pp.	pages
SEM	Scanning electron microscope
TBC	Thermal barrier coating
TCP	Topologically close packed
TE	Trailing edge
vs.	versus
wt	weight

1. INTRODUCTION

1.1. High Temperature Materials and Superalloys

Advanced aviation engines and land-based gas turbines can increase their efficiency by operating at highest possible temperatures [1]. Of course, this necessitates utilization of materials that can operate at high temperatures. A characteristic of high temperature materials is to operate at temperatures close to their melting point, T_m. T_{op}/T_m for these materials should be greater than 0.6 where T_{op} is the operation temperature. Properties required in high temperature materials are the resistance to mechanical degradation for long periods of times and tolerance for severe operating conditions.

Superalloys are within the high temperature materials category and generally possess high operating temperatures, good ductility, impact resistance, high and low cycle fatigue resistance, thermal fatigue, and creep resistance [2].

The most widespread use for superalloys is the gas turbine industry [2]. Besides aircraft, marine, industrial and vehicular gas turbines, superalloys are also used in space vehicles, rocket engines, experimental aircraft, nuclear reactors, submarines, steam power plants, petrochemical equipment, and other high temperature applications [2].

1.2. Turbine Blades

Turbine blades are manufactured in conventionally cast, directionally solidified, or single crystal forms. Intergranular cavitation, void formation, slip under stress and increased chemical activity occur along grain boundaries at high temperatures. Therefore, it has become a necessity to eliminate grain boundaries from turbine blades. As a result, directionally solidified and single crystal turbine blades with improved creep strength have recently replaced the conventionally cast ones in high temperature applications [3-5]. Still, land based gas turbines use polycrystalline blades.

Turbine blades are exposed to environmentally induced degradation while operating. These exposition types are hot corrosion and high temperature oxidation [4]. Hot corrosion is a rapid attack which is related with alkali metal contaminants that react with sulfur in the fuel and resulting in formation of molten sulfates [4, 6]. When alkali metal contaminants and sulfur do not exist in the environment, high temperature oxidation is the dominant degradation type. The oxidation is dependent on the rates of anion and cation transport that happens through the lattice or along grain boundaries in the oxide. Oxidation becomes more rapid if the temperature is higher [4, 5].

In order to provide the required hot corrosion and oxidation resistance, coatings are utilized in the turbine blades. Coating is a layer of material on the surface of the turbine blade which prevents the contact between environment and turbine blade. Elements in the coating react with the oxygen in the environment and form a protective oxide layer. In other words, coating is a source of elements forming an oxide layer that prevents diffusion of harmful elements like oxygen, nitrogen, sulfur into the turbine blade [4, 6].

Aluminide (diffusion) coatings, overlay coatings, and thermal barrier coatings are three types of coating available in turbine blades [4, 5, 7]. Aluminide (diffusion) coating relies on the interdiffusion between the deposited Al and Ni in the base metal. As a result of this interdiffusion, a resistant NiAl outer aluminide layer is formed [4-6]. In overlay coatings, an alloy with predetermined composition is applied on the turbine blade. Elements required to form the protective layer are available in the applied alloy. Therefore, interdiffusion is not needed. Interdiffusion is only needed at the interface so that the coating attaches to the surface of the turbine blade [4, 6]. The coatings are called MCrAlY where M is Ni, Co, or Ni + Co [4]. In a research [8], NiCrAlY, CoCrAlY, and NiCoCrAlY coated specimens were put in corrosive environment and their durability were measured. Among them, NiCoCrAlY coated specimen showed the best hot corrosion resistance.

Thermal barrier coatings are ceramic outer protective layers usually ZrO_2 [4-6] and also Y_2O_3 [4]. This is a multilayer coating system which means there is an additional inner metallic layer (bond coat) between the thermal barrier coating and the turbine blade [4-6]. Thermal barrier coatings have low thermal conductivity, so they serve as a barrier to heat. Bond coat provides oxidation resistance if spallation of ceramic occurs [6].

Thickness of the coating was observed to be an important design parameter [9, 10]. When the thickness of the coating becomes more than a certain value, its protective effect starts to decrease. Gurrappa et al. [10] have showed this by observing NiCoCrAlY coated specimens with 100, 200, 300 and 400 μm thicknesses of thermal barrier coating under corrosive environment. Among these specimens, 300 μm thick thermal barrier coating has showed the maximum life. If the thickness is improved furthermore, adherence problems will result in a shorter life.

1.3. Types of Superalloys

Generally, there are more than ten alloying elements in superalloys, making them the most complex structured materials. These alloys are composed of a gamma (γ) matrix and other phases embedded in the matrix such as gamma prime (γ') precipitates, carbides, oxides, etc. Three types of superalloys are classified according to the base element, nickel, iron, and cobalt [1].

1.3.1. Nickel base superalloys

Nickel is the base element in these superalloys. In addition to nickel; cobalt, iron, chromium, ruthenium, molybdenum, rhenium, and tungsten are available in the matrix phase (γ phase). Aluminum, titanium, and tantalum form an $L1_2$ ordered Ni_3(Al, Ti, Ta) γ' precipitate phase. Also, a γ'' ordered precipitate phase forms in the high niobium composition alloys with DO_{22} superlattice structure. Carbides, borides, and topologically close packed phases (TCP) are also present in nickel based superalloys [1].

1.3.2. Iron base superalloys

Iron is the major element in these superalloys. About 25% nickel is available in iron base superalloys to stabilize the austenitic matrix. Also, about 15% chromium provides corrosion resistance. Moderate amount of molybdenum is contained for solid solution strengthening. Small amounts of aluminum, titanium, and niobium are added for precipitation hardening. Aluminum and titanium are formers of γ' precipitate phase whereas niobium is γ'' precipitate former [2].

1.3.3. Cobalt base superalloys

Main element is cobalt in this type of superalloys. Chromium is available for surface stabilization. Tungsten is required for solid solution strengthening. Nickel and molybdenum are also available in cobalt base superalloys. Titanium, zirconium, columbium, tantalum and carbon are carbide phase former elements. These superalloys are strengthened by solid solution and carbide strengthening [2].

Sato et al. [11] have introduced precipitate strengthening in cobalt base superalloys. γ' Co_3(Al, W) having $L1_2$ structure precipitates in the γ face centered cubic cobalt matrix. This γ/ γ' structure is similar to that in nickel base superalloys.

It has been observed that high temperature strength of precipitate strengthened new cobalt based superalloys is comparable to that of nickel base superalloys [11-13]. Of course, this discovery is expected to lead to the development of a new class of high temperature superalloy [11-16].

1.4. Phases in Superalloys

1.4.1. Gamma (γ) Phase

This matrix phase has a face centered cubic (FCC) structure. The matrix phase is continuous so that other phases reside in this phase. Aluminum and chromium in the matrix form a protective scale on the surface and therefore increase oxidation resistance. Some elements present in the matrix for solid solution strengthening are cobalt, iron, chromium, molybdenum, tungsten, vanadium, aluminum, titanium, ruthenium and rhenium [1, 2].

1.4.2. Precipitate Phase

Precipitation hardening is the most important strengthening mechanism in superalloys. In nickel base superalloys, primary strengthening precipitate is Ni_3(Al, Ti, Ta) and it is called γ'. This precipitate phase is generally coherent with the matrix. γ' phase has $L1_2$ ordered face centered cubic crystal structure in which nickel atoms are at the face

centers and aluminum atoms are at the corners of the cube. As a result, there are six 1/2 Ni atoms at the face centers and eight 1/8 Al atoms at the corners. Therefore, three Ni atoms and one Al atom are available in the unit cell resulting in $L1_2$ structure [1, 6]. In Figure 1.1, $L1_2$ structure is given [1].

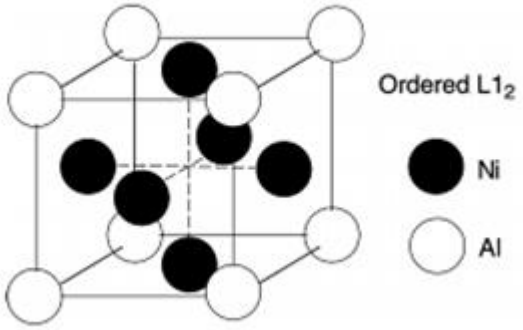

Figure 1.1. $L1_2$ Crystal Structure.

If the lattice parameters of γ and γ' are close, then γ/γ' interface protects coherency and interface energy is low. Coherency between the γ/γ' interface gives rise to misfit strain. The lattice misfit, δ, is defined as:

$$\delta = 2(a' - a) / (a' + a) \tag{1.1}$$

In this equation, a is matrix lattice parameter and a' is the precipitate lattice parameter. The lattice misfit is positive if the lattice parameter of the precipitate is greater than that of the matrix. If the lattice misfit is small, then γ/γ' interface is coherent and coherency strains are formed at the γ/γ' interface resulting in strengthening [1].

1.4.3. Carbides

Most important types of carbides are MC, M_6C, $M_{23}C_6$, M_7C_3, where M represents a metal atom such as Cr, Mo, Ti, Ta, Hf. MC carbide precipitates from the liquid phase at high temperatures. Therefore, carbides are usually found in interdendritic regions and there is no orientation relationship with the matrix. $M_{23}C_6$ usually precipitates on matrix phase grain boundaries. Carbides are called grain boundary strengtheners, because preferred location of carbides at grain boundaries leads to an increase in rupture strength through prevention of grain boundary sliding [1].

1.4.4. Borides

They are of the form M_3B_2 where M implies a metal. Similar to carbides, borides prefer to form at matrix grain boundaries which results in increased rupture strength with prevented grain boundary sliding, therefore borides, like carbides, are grain boundary strengtheners [1].

1.4.5. Topologically Close Packed (TCP) Phases

High amount of Cr, Mo, W, Re leads to the formation of TCP phases. In other words, TCP phases are rich in terms of elements that have high melting temperature. TCP phases contain tetragonal σ phase and rhombohedral μ phase. μ phase has the form A_6B_7, examples are W_6Co_7, Mo_6Co_7. Examples of σ phase are Cr_2Ru, $Cr_{61}Co_{39}$, $Re_{67}Mo_{33}$. TCP phases are not desired in superalloys because they have a brittle character and reduce the amount of strengthening elements in the solid solution matrix. They lead to crack initiation during cyclic loading [1, 17].

1.5. Nucleation and Growth of Precipitates

Precipitate nucleation is a solid state phase transformation where atoms accumulate in regions via diffusion and form physically and chemically distinct regions in a matrix. Nucleation is of two types which are homogeneous nucleation and heterogeneous nucleation [18].

If there are sites available for nucleation, for example, excess vacancies, dislocations, grain boundaries, stacking faults, inclusions, and free surfaces impurity particles, then the nucleation is called heterogeneous. If no heterogeneous nucleation sites are available, then nuclei will form homogeneously in a matrix which is called homogeneous nucleation. The latter mechanism requires higher energy [18].

During nucleation when embryos grow beyond a critical size, they become nuclei and start to grow to precipitates. A precipitate possesses strain energy due to lattice misfit and interface energy due to formation of an interface between precipitate and matrix. Sum

of the strain energy and interface energy determines the precipitate morphology during growth [18, 19].

Ostwald ripening (coarsening) process begins after the growth process finishes. In this process, volumetric ratio of precipitates remains constant and precipitates decrease in number. Coarsening of precipitates occurs in accordance with Ostwald ripening mechanism in which large precipitates grow by consuming small precipitates [20, 21]. This can be explained with Gibbs-Thomson effect. If particle size is small, it has a high curvature and solute concentration around that particle. Therefore, concentration gradients form and solute atoms diffuse from high concentration regions to low concentration regions resulting in the growth of the coarse particles and shrinkage of the fine particles [18].

Separate studies of Lifshitz and Slyozof [20] and Wagner [21] give a theory that relates precipitate coarsening with time. According to LSW theory, a relation between particle radius and time is stated below.

$$r_t^3 - r_0^3 = kt \tag{1.2}$$

In this equation, t is time, r_t is the radius at time t, r_0 is initial average radius and k is rate constant.

1.6. Rafting

Rafting is defined as the preferential alignment of the precipitates in certain directions [1, 22-30]. Rafting is affected by sign of lattice misfit and applied stress. When the sign of the misfit and applied stress are the same, the rafts develop parallel to the direction of applied stress and called P type, otherwise they form perpendicular to the stress direction and called N type [1].

When stress is applied, elastic interactions occur between the matrix and precipitate [22-24]. Change in the lattice strain energy and change of the interatomic potential energy are equivalent. As a result, change of the interatomic potential energy, change of the

interfacial energy and change in the misfit stress on the interface can be considered as a driving force for the diffusion of elements leading to rafting [23].

Let us consider tension in [001] direction in a negative misfit alloy. Then, coherent strain energy decreases in the γ/γ' interface of (001) plane. The released energy from this plane causes diffusion of Al and Ta atoms from (001) plane to (010) and (100) planes. This results in the growth of γ' phase in the [100] and [010] directions and N type rafting forms. The elements like Mo and Cr diffuse in the opposite direction. This counter diffusion mechanism resulted by the released misfit energy causes rafting. If the stress was compressive, diffusion of Al and Ta would occur from (010) and (100) planes to (001) plane, causing P type rafting. Also, effect of changing the sign of the misfit is equivalent to changing the sign of the stress. It can be concluded that rafting of precipitates depend on the signs of applied stress and misfit [22, 24].

1.7. IN738LC Nickel Based Superalloy

IN738 is a nickel base superalloy. It is polycrystalline. There are two types of this superalloy, IN738C has a high carbon content (nominal 0.17 wt% C) and IN738LC has a low carbon content (nominal 0.11 wt% C) [31].

Melting temperature of IN738LC is in the range of 1232-1315°C, and it has an operation temperature up to 980°C. It is important to note that IN738LC is a positive misfit alloy. IN738LC is usually used in land based turbine parts, example given, nozzle guide vanes and rotary blades. It is designed for the gas turbine industry to have good creep strength up to 1000°C and also to withstand long-time exposure to hot corrosion [31]. Composition of IN738LC is given in Table 1.1 [31].

Table 1.1. Elements present in IN738LC superalloy.

Element	Ni	Cr	Co	Mo	W	Ta	Nb	Al	Ti	B	Zr	C
Wt%	Balance	15,7-16,3	8,0-9,0	1,5-2,0	2,4-2,8	1,5-2,0	0,6-1,1	3,2-3,7	3,2-3,7	0,007-0,012	0,03-0,08	0,09-0,13

1.8. Objectives

Microstructure of an as-serviced, nickel-based turbine blade made of polycrystalline superalloy IN738LC will be investigated in grain and precipitate scale. Blade has worked 80,000 hours at first stage of the hot section in an electricity producing natural gas turbine. Results of this study will contribute to life prediction efforts for IN738LC first stage turbine blades. Also, this research investigates rafting in a polycrystalline superalloy. As rafting is usually studied in the literature using single crystal alloys, this current research will be a unique contribution to the literature.

This study is expected to provide:

- Determination of the microstructure variations in the blade to consequently predict the high/low stress/temperature regions.
- Comparison to available experimental/numerical results.
- Feed data to numerical and analytical models.
- Better life planning of the turbine blades.

2. EXPERIMENTAL

Microstructure of a hot section, first stage serviced turbine blade was analyzed. This blade served 80,000 hours. The blade has internal cooling channels and is coated with a thermal barrier coating (TBC).

A total of nine samples was extracted from the blade by an electrical discharge machine (EDM) at three sections along blade axis, near the root, at mid-length, and near the tip. Specimens from the leading edge, trailing edge, and mid way between the two and both from the suction side and pressure side were obtained. As a result, specimens from 18 different positions of the blade were obtained. Also, one specimen from the firtree region was obtained. A three dimensional right handed coordinate system was assigned to the blade. In this coordinate system, positive x direction is from pressure side to suction side, positive y direction is from the leading edge to the trailing edge and, positive z direction is from the root level to the tip level. Positive z direction is also called as blade axis. Positions of specimens obtained from pressure side and suction side of 80,000 hours operated blade are given in Figure 2.1 and Figure 2.2, respectively. Coordinate system mentioned is also given in these figures. Location of the firtree specimen can be seen in Figure 2.2.

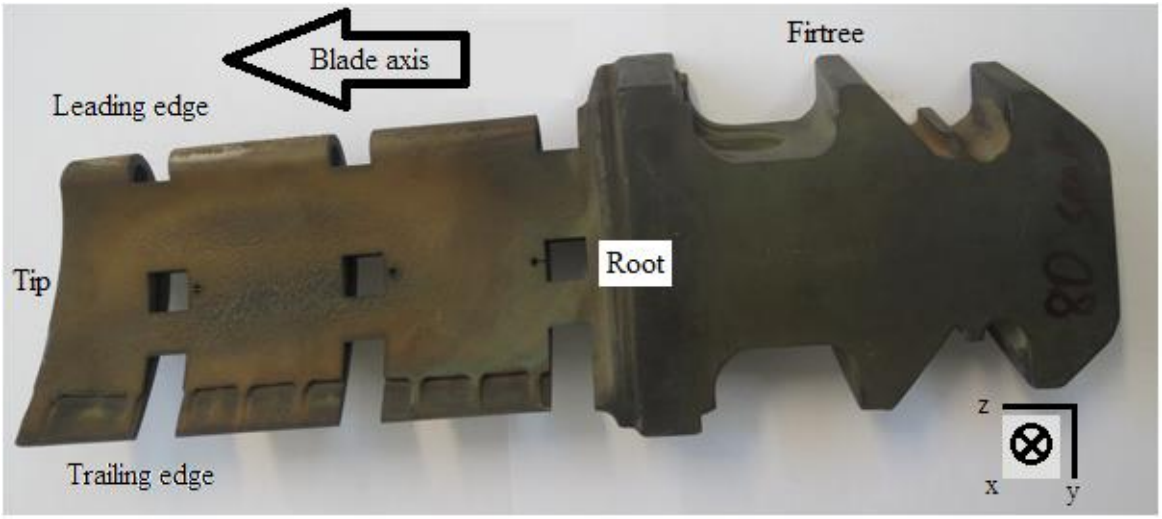

Figure 2.1. Specimen positions in the pressure side of the served turbine blade.

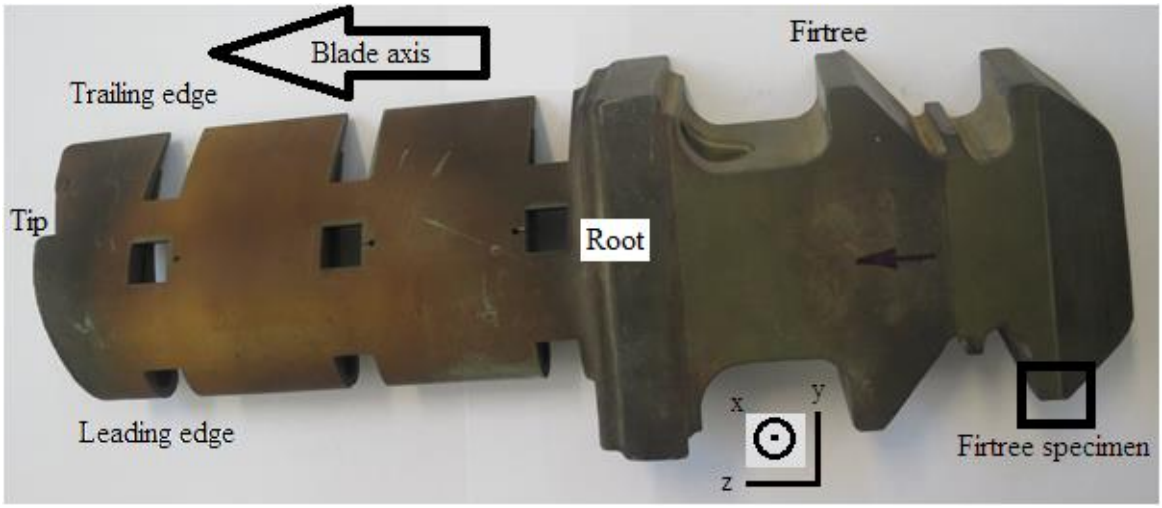

Figure 2.2. Specimen positions in the suction side of the served turbine blade.

A notation was developed to identify each specimen, which starts with B80 that gives time of service (80,000 hours). Then, the letters S, P, or O follow to show that specimen is from the suction side, pressure side or stagnation point of the blade, respectively. It should be noted that stagnation point specimens are only available at the leading edge. Then, one of the letters R, M, or T is used to indicate that the specimen is a root section, middle section, or tip section specimen, respectively. Following letter is one of the T, M, or L meaning that the specimen is a trailing edge, middle position, or leading edge specimen, respectively. One last letter is H, C, or Z. H indicates hot surface, C indicates cold surface, and Z is used for the surface perpendicular to the blade axis. Few additional letters are used for specific locations. For middle position specimens, S indicates the side surface that is perpendicular to y axis. For trailing edge specimens, I indicates the side surface close to inner part of the blade and O indicates the side surface close to the trailing edge or outer part of the blade.

In Figures 2.3-2.5, photos of trailing edge, middle position, and leading edge specimens of the root level are given respectively.

These samples shown in Figures 2.3-2.5 initially cut by the EDM were further sectioned by a precision diamond wafering disc in order to expose different surfaces for microstructure observation. Since cooling air passes through the cooling channels of the turbine blades during operation, microstructure of cooled surface is expected to differ from that of the hot surface which is TBC coated.

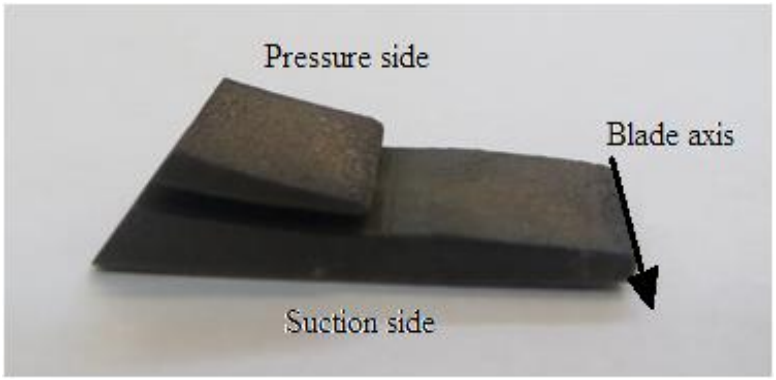

Figure 2.3. Trailing edge samples (B80-SP-RT).

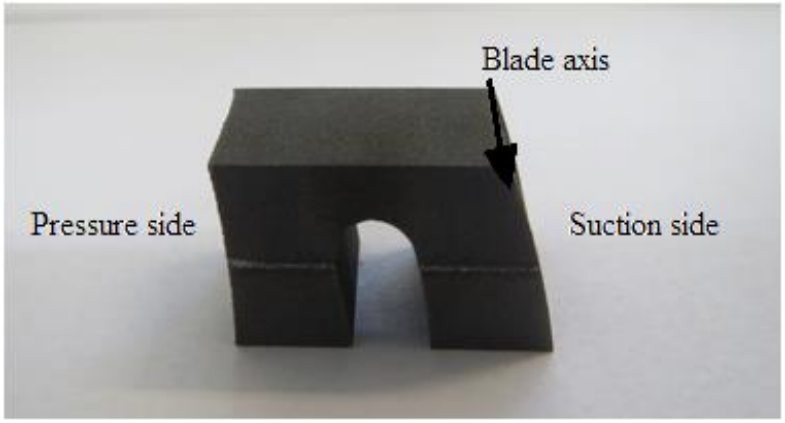

Figure 2.4. Middle position samples (B80-SP-RM).

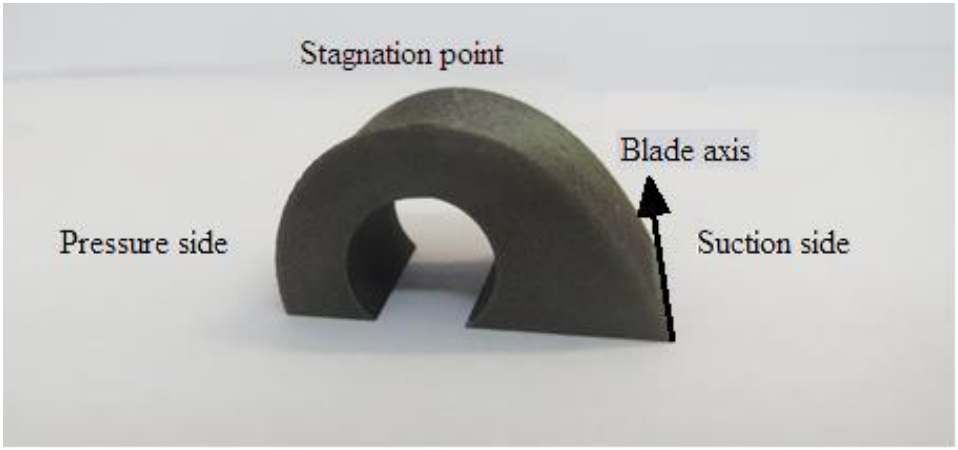

Figure 2.5. Leading edge samples (B80-SPO-RL).

For trailing edge specimens, hot surface, cold surface, surface perpendicular to blade axis, surface close to trailing edge, and surface far from trailing edge were observed. These surfaces are given in Figure 2.6. Dashed lines represent cut surfaces by the diamond disc. Dark shading indicates analyzed surfaces.

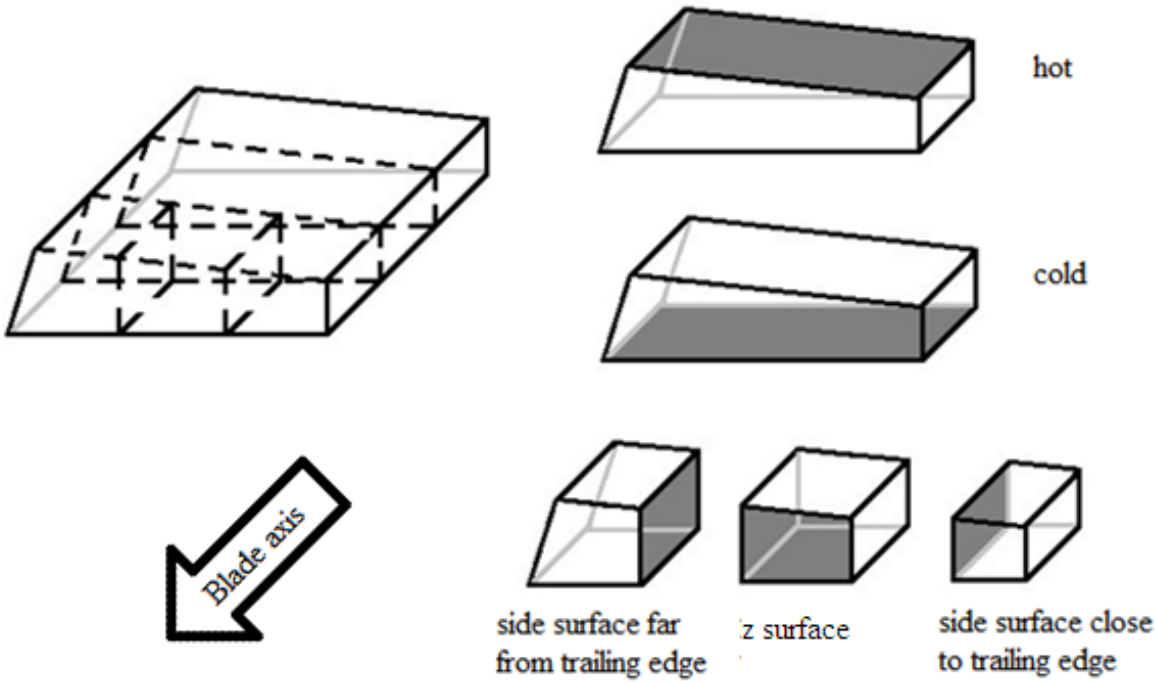

Figure 2.6. Pressure side trailing edge (PT) specimens. Analyzed surfaces are shaded dark.

For middle position specimens, hot surface, cold surface, z surface, and side surface (surface perpendicular to y axis) were observed. These surfaces are given in Figure 2.7.

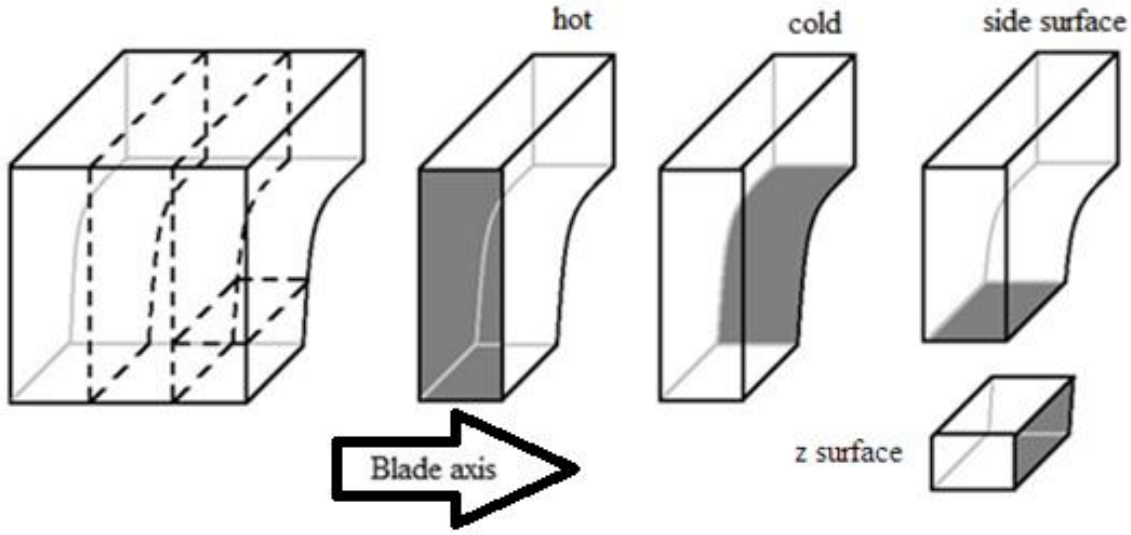

Figure 2.7. Pressure side middle position (PM) specimens. Analyzed surfaces are shaded dark.

Leading edge specimens were cut by a diamond disc and three pieces were obtained. These were suction side specimens, stagnation point specimens and pressure side specimens. Hot surface, cold surface and z surface were observed for pressure side specimens, suction side specimens and stagnation point specimens. Figure 2.8 shows surfaces analyzed for leading edge specimens.

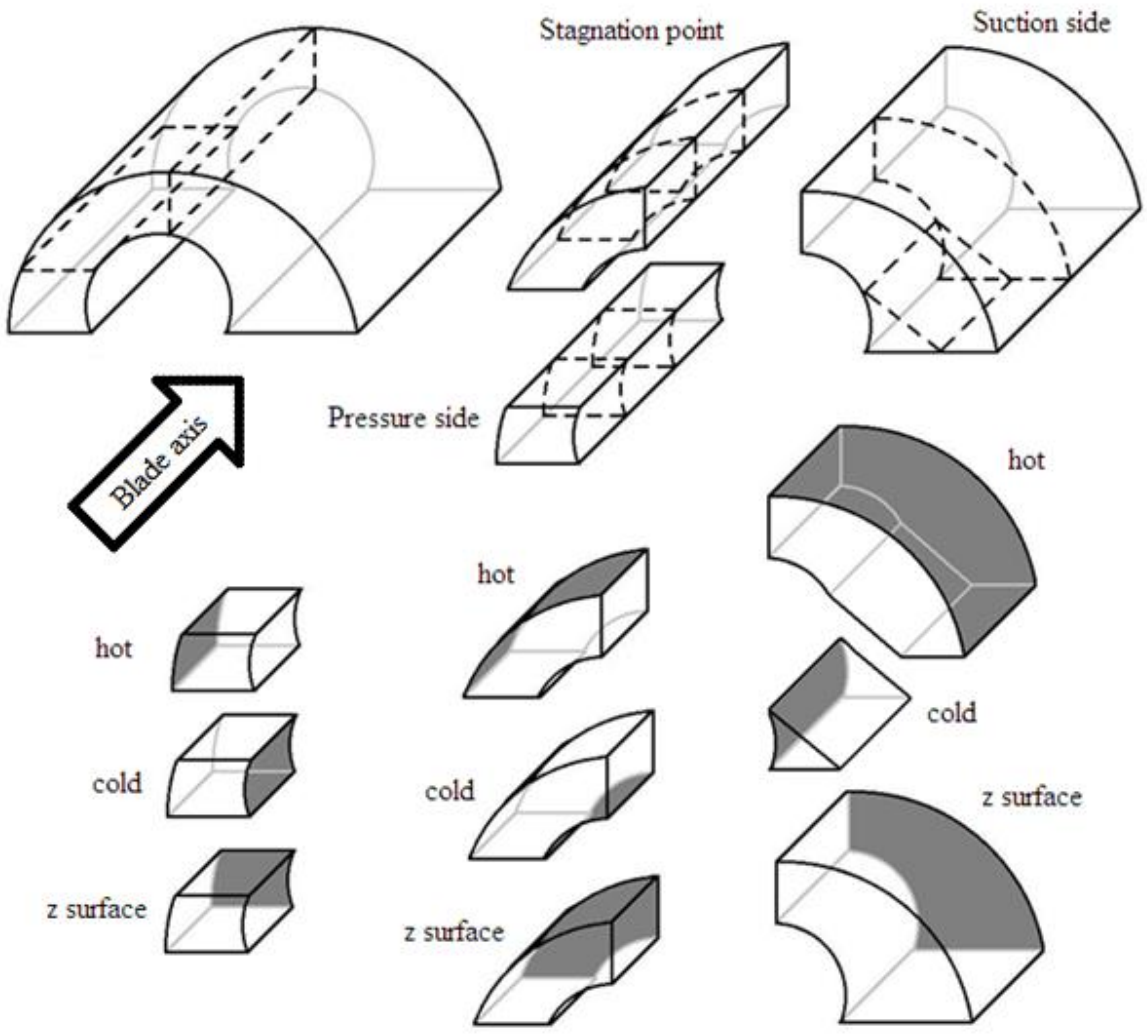

Figure 2.8. Leading edge (PL, OL, SL) specimens. Analyzed surfaces are shaded dark.

After cutting with a diamond disc, specimens were cold mounted, ground by grinding papers, and polished by alumina powders. It should be noted that there were thick coatings available on the hot surface. These coating layers have been fully ground in order to study grain size/morphology for hot surfaces.

A representative mount for root section trailing edge specimens and their notations are shown in Figure 2.9. As can be seen, all sectioned specimens from a specimen are mounted together.

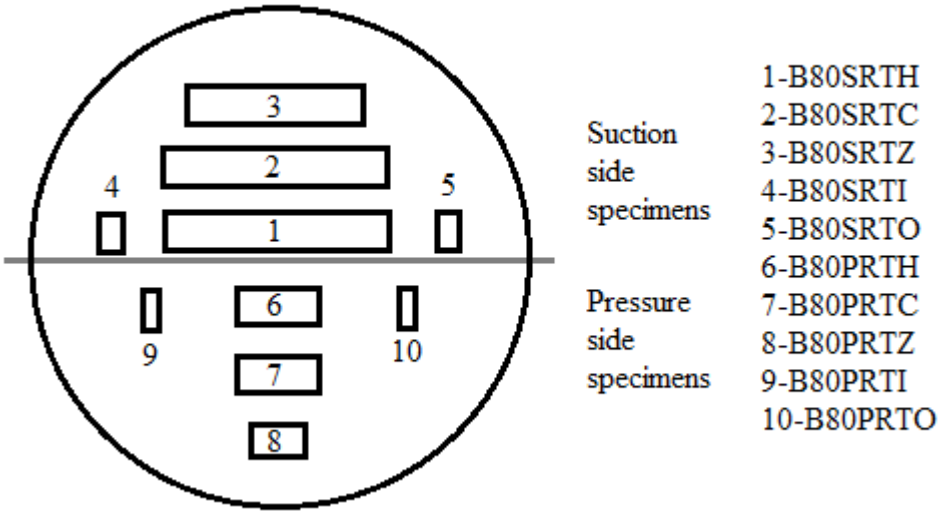

Figure 2.9. Representative mount for root section trailing edge (RT) specimens and their notations.

After these steps, grain boundary observation of specimens under light microscope was carried out to determine the grain size. Marble's reagent was used for grain boundary observations. Composition of Marble's reagent is 10 g $CuSO_4$ + 50 ml HCl + 50 ml H_2O.

Then, scanning electron microscope observations of specimens was completed to identify the precipitate structure. Back scattered electron mode of Philips XL30 ESEM FEG/EDAX system was used for this purpose. For precipitate observations, etchant having composition 33 ml HNO_3+ 33 ml CH_3COOH + 33 ml H_2O + 1 ml HF was used.

Also, semi quantitative determination of composition by energy dispersive spectroscopy technique of EDAX system was completed.

3. RESULTS

3.1. The Coatings

Optical microscope and SEM images show that the blade consists of a very thin ceramic TBC layer bounded to the base metal via four additional layers. Figure 3.1 shows the tip section of the blade and these layers are visible. The thermal barrier coating seperates these layers from the environment. Four coatings are available under the TBC. First three coatings under the TBC have almost constant thickness. These coatings are more easily differentiated in SEM photos than optical microscope photos. There is a fourth layer on the base metal with a varying thickness, which is only available in the leading edge position. The thickness of this layer is maximum at the stagnation point; it decreases and then disappears while moving toward the trailing edge both on the pressure and suction sides, so this layer is not observed in the middle and trailing edge positions.

Layer thicknesses in the tip section leading edge position are given in detail in Figure 3.2. Total thickness of the first, second and third layers, the thickness of the fourth layer, and the thickness of the base metal are given in the photo.

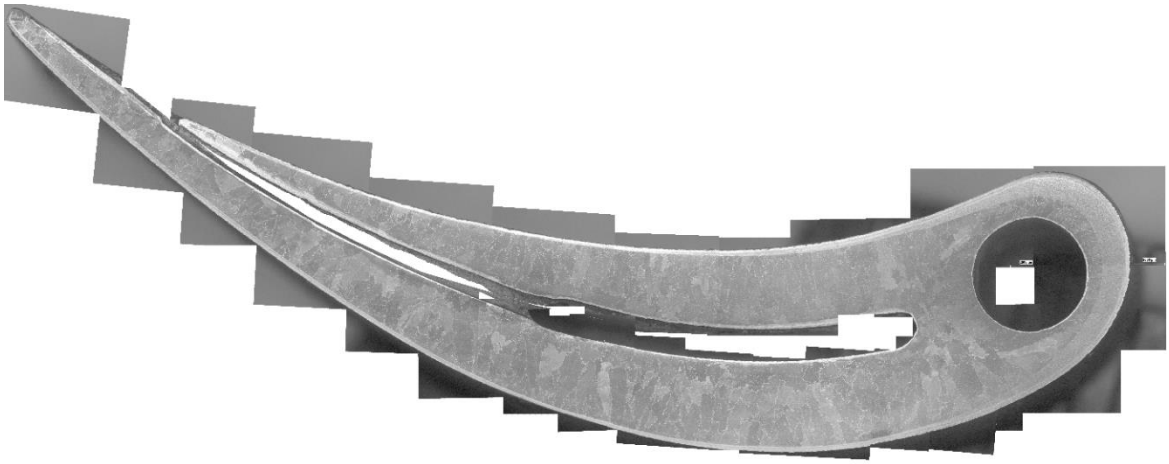

Figure 3.1. Coating layers available in the blade.

Figures 3.3, 3.4, and 3.5 respectively give the combined leading edge pictures of tip section, middle section, and root section and show the coatings.

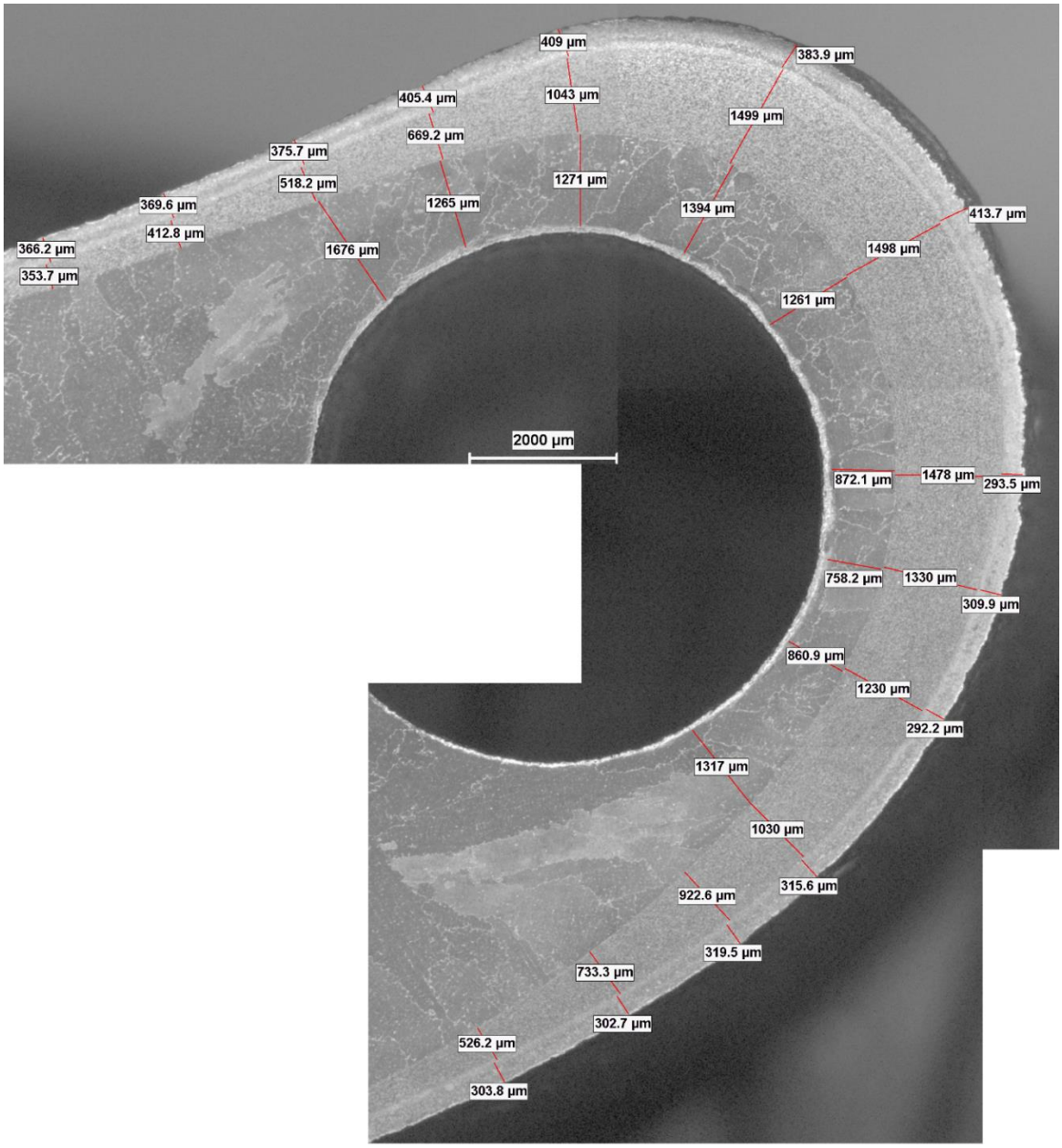

Figure 3.2. Layer thicknesses in SPO-TL (tip section, leading edge) position.

In order to determine the composition of the coatings and the metal, an EDS analysis was conducted. The analysis was completed on the suction side, root section, leading edge, z surface specimen (B80SRLZ). Photograph of this specimen is given in Figure 3.6. Composition values at several positions were obtained along the white arrow shown in Figure 3.6. The distances of these positions from the TBC are given in Table 3.1.

SEM photos of the TBC, first three coatings and the beginning of the fourth coating are given in Figure 3.7. Also, analysis points from 1 to 17 are given in the figure. First

three points 1-3 (10 to 30 microns) are in the thermal barrier coating. Points 4 and 5 (40 and 80 microns) belong to the first coating and this layer ends at 110 microns. Figure 3.8 gives SEM photo of the TBC and first coating after the application of the precipitate etchant. It is seen in this figure that the matrix is free of precipitates.

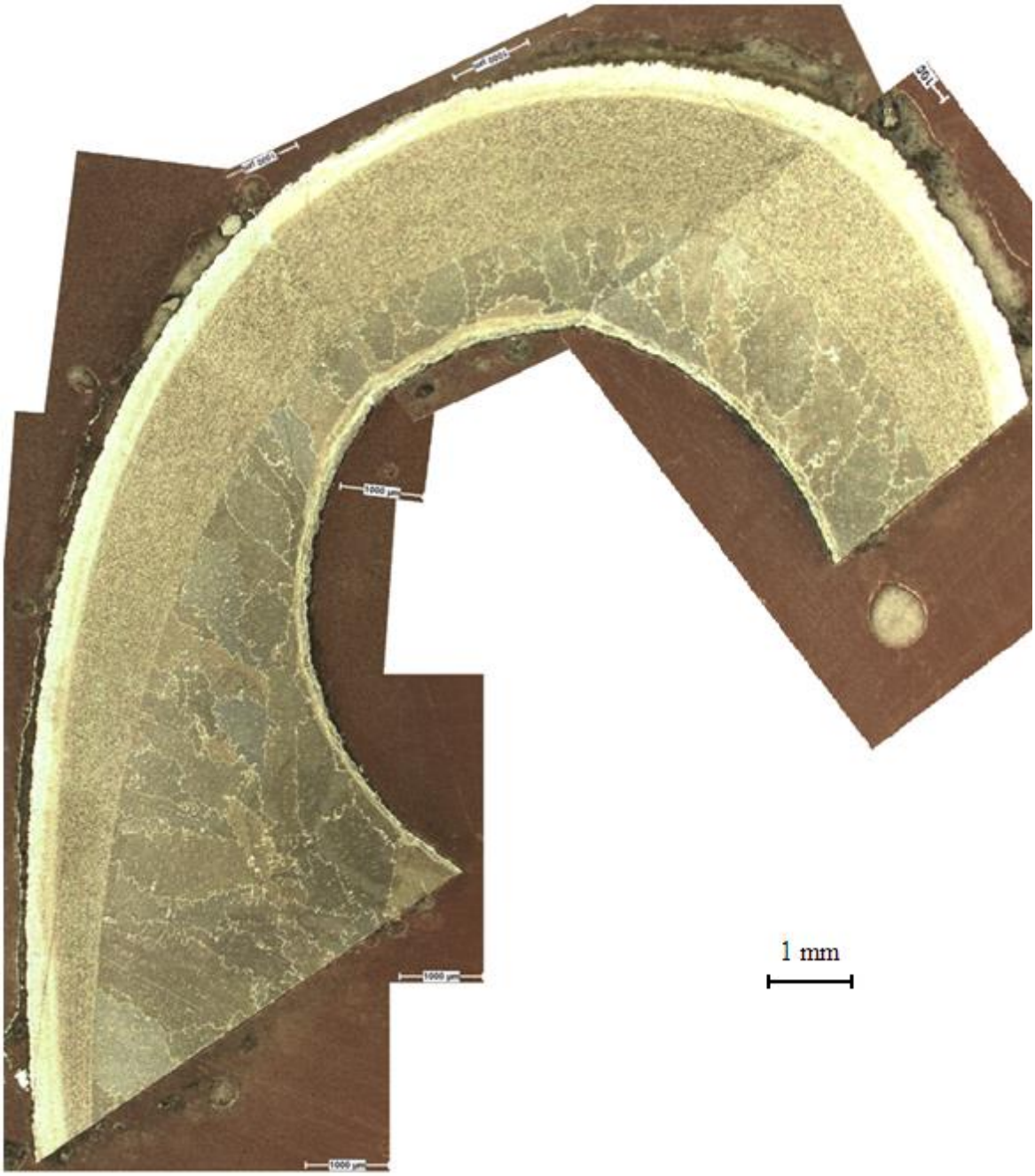

Figure 3.3. Coatings in SPO-TL (tip section, leading edge) position.

Point 6 (120 microns) is just the beginning of the second coating. This coating continues to point 14 (300 microns). SEM photo in Figure 3.9 gives the second coating and

its boundary with the first coating. The photo is taken before precipitate etching. SEM photo in Figure 3.10 is taken after precipitate etching and give the microstructure of the second coating. Precipitates in the second coating are seen in this figure.

Dark particles have been observed in Figure 3.9. Number of these particles in the first coating is much less than that in the second coating. An EDS analysis, done on few of these particles, has indicated that these are α-Cr particles. These Particles have not been observed in the other coating layers.

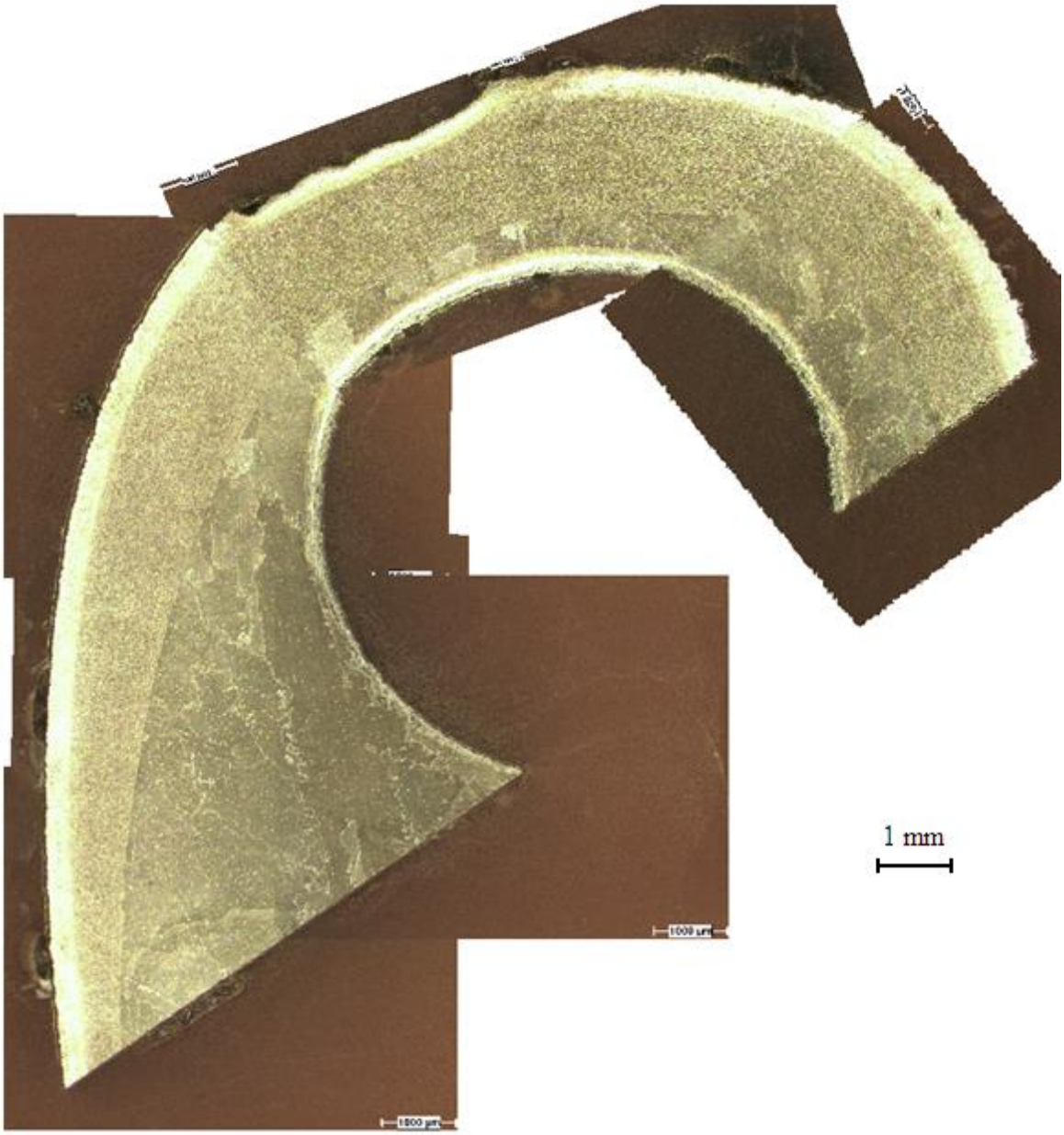

Figure 3.4. Coatings in SPO-ML (middle section, leading edge) position.

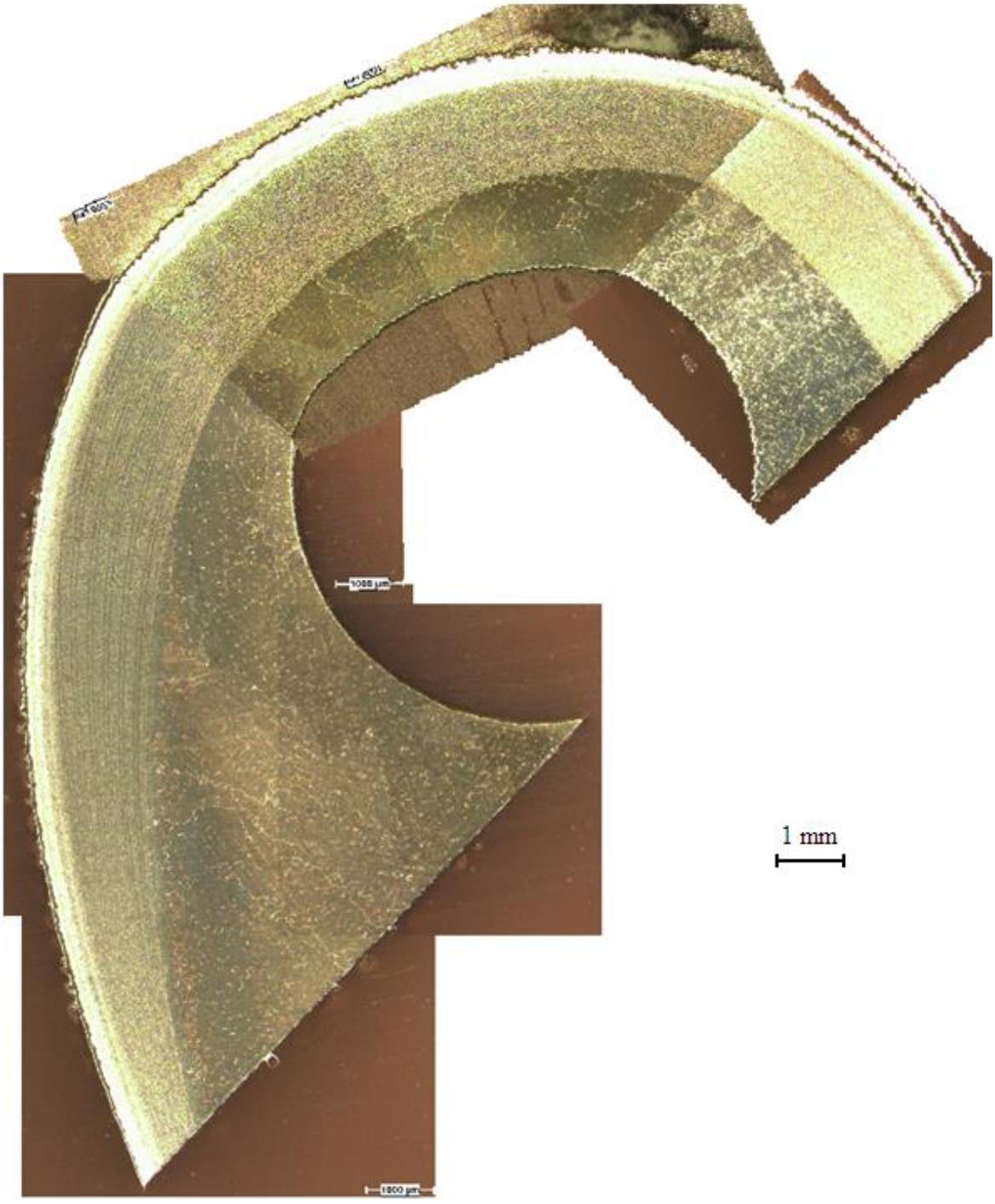

Figure 3.5. Coatings in SPO-RL (root section, leading edge) position.

Points from 15 to 17 (330 to 390 microns) give data for the third coating. This coating has a thickness of approximately 100 microns. Figures 3.11 and 3.12 give the SEM photos of the third coating after the precipitate etchant is applied; at the boundary with the second coating and fourth coating, respectively. Then, the fourth coating starts and includes points 18 to 25 (590 to 1990 microns).

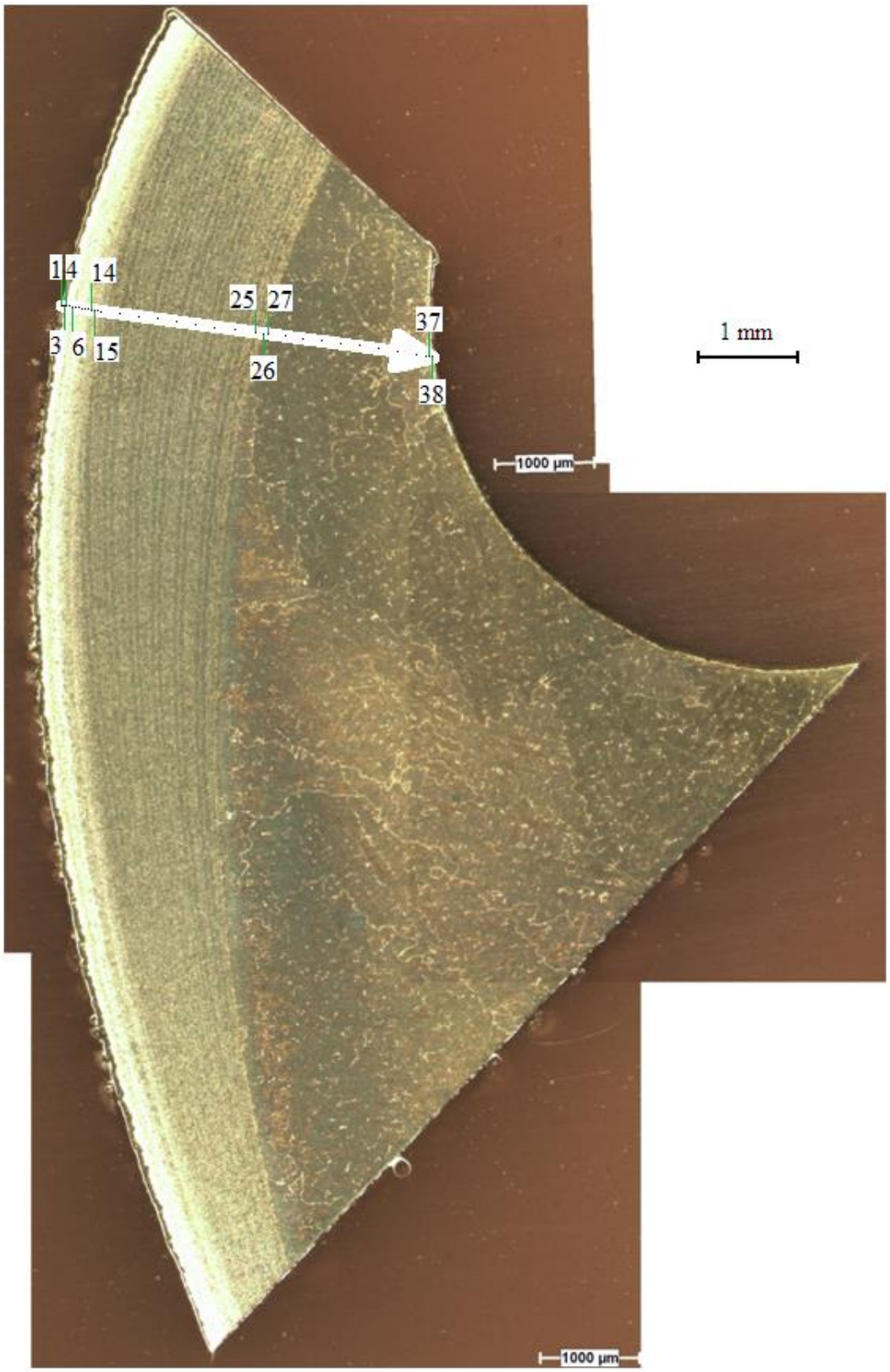

Figure 3.6. EDS analysis spots shown along the white arrow extending from the TBC to the cooling channel in the suction side, root section, leading edge, z surface specimen (B80SRLZ).

Table 3.1. EDS analysis spots in Figure 3.6.

No	1	2	3	4	5	6	7	8	9	10	11	12	13	14	15	16	17	18	19	20	21	22	23	24	25	26	27	28	29	30	31	32	33	34	35	36	37	38
μm	10	20	30	40	80	120	150	180	180	180	220	240	270	300	330	360	390	590	790	990	1190	1390	1590	1790	1990	2050	2090	2290	2490	2690	2890	3090	3290	3490	3690	3790	3810	3820
Coating	TBC			1st		2nd									3rd			4th								Boundary	Base metal											Cooling channel
Type	NiAl $NiAl_2$ Al_2O_3			Transition		NiCrAlY									Transition			NiCoCrAlY								Transition	Base metal											Chromia

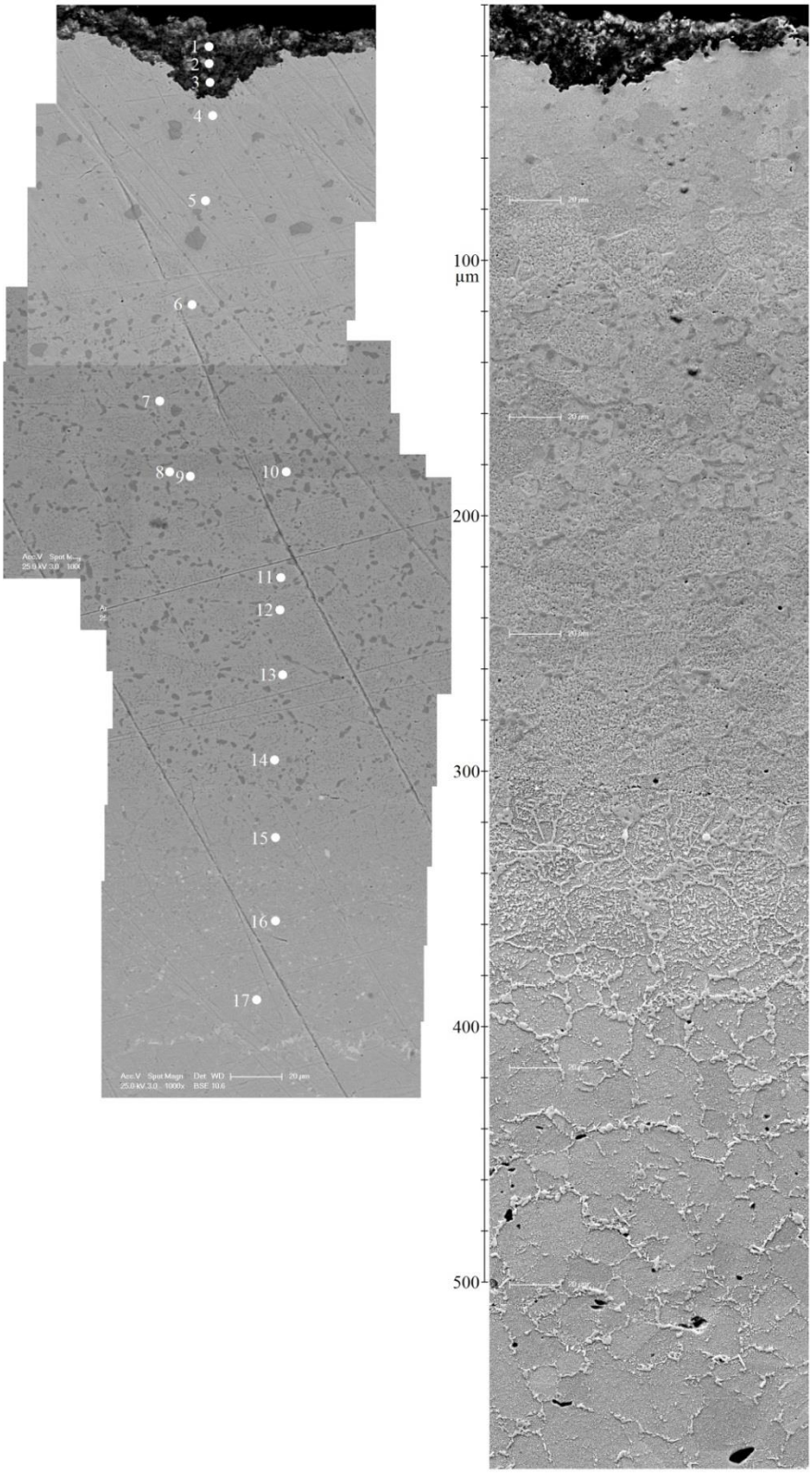

Figure 3.7. SEM photos of the TBC (1-3), first (4-6), second (7-14), third (15-17) coatings and the beginning of the fourth coating. The photo on the left is taken before precipitate etching and the photo on the right is taken after precipitate etching.

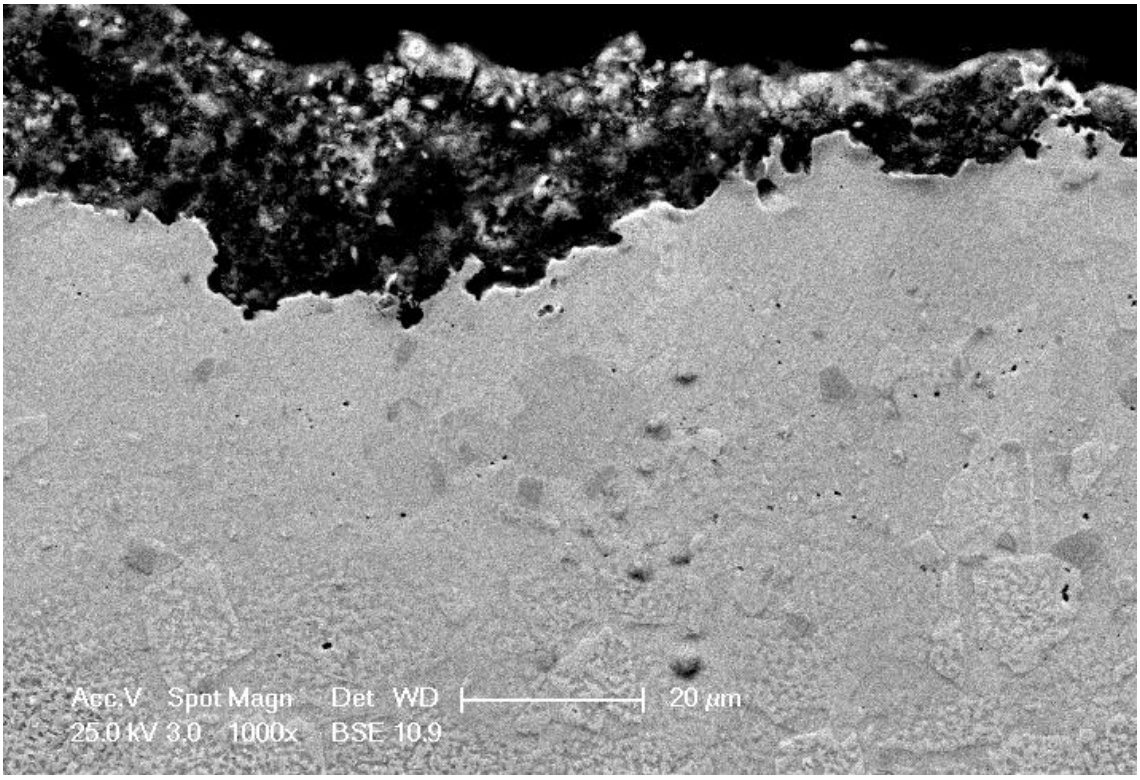

Figure 3.8. SEM photo of the TBC and first coating after the precipitate etchant applied.

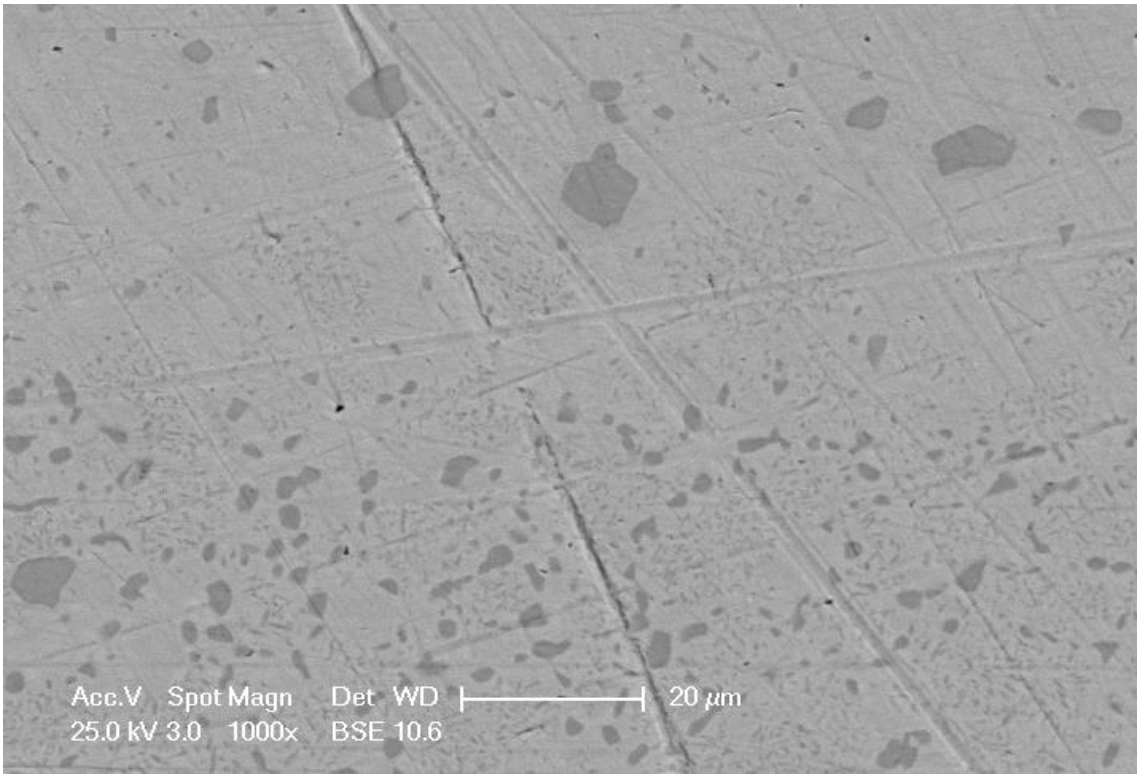

Figure 3.9. SEM photo of the first and second coatings before the precipitate etchant applied.

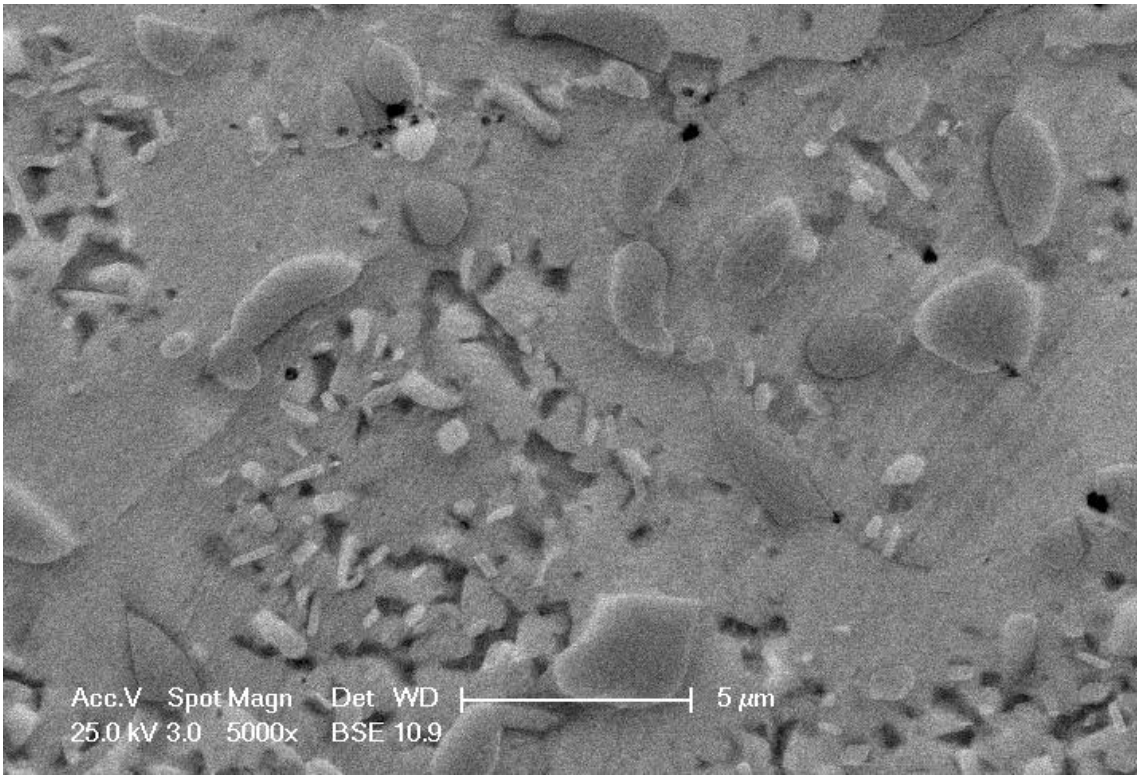

Figure 3.10. SEM photo of the second coating after the precipitate etchant applied.

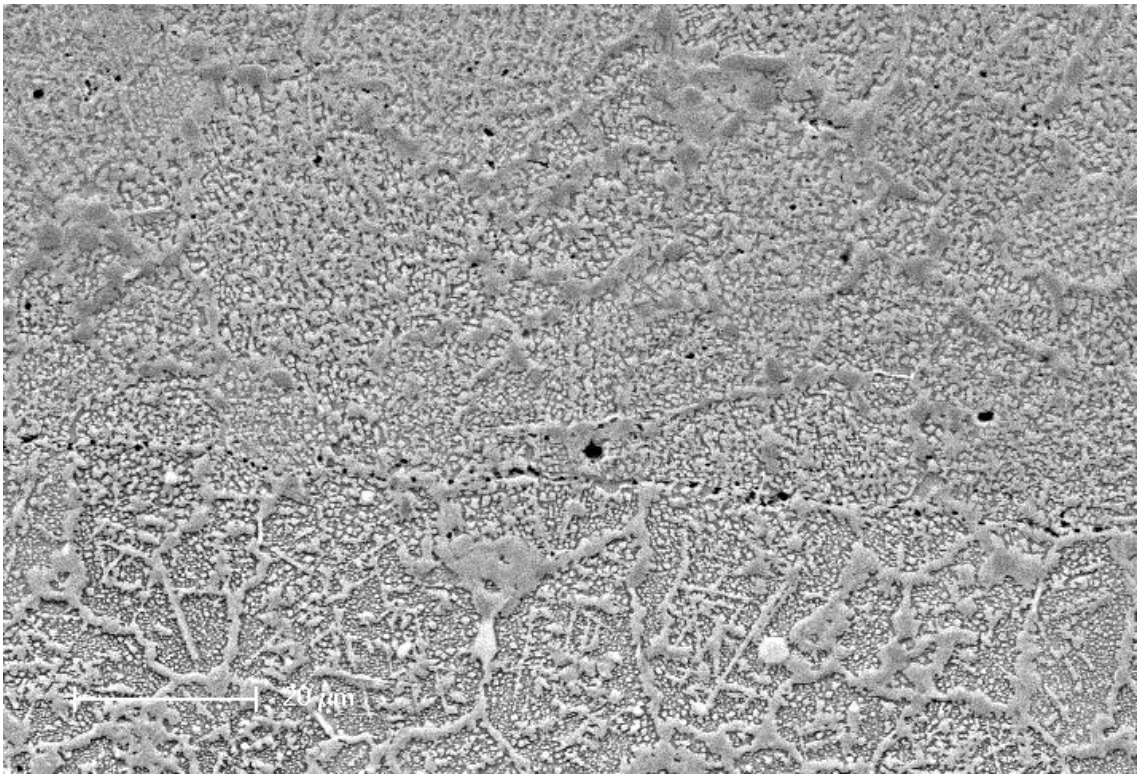

Figure 3.11. SEM photo of the boundary between the second and third coatings after precipitate etching. Porosity is visible along the boundary.

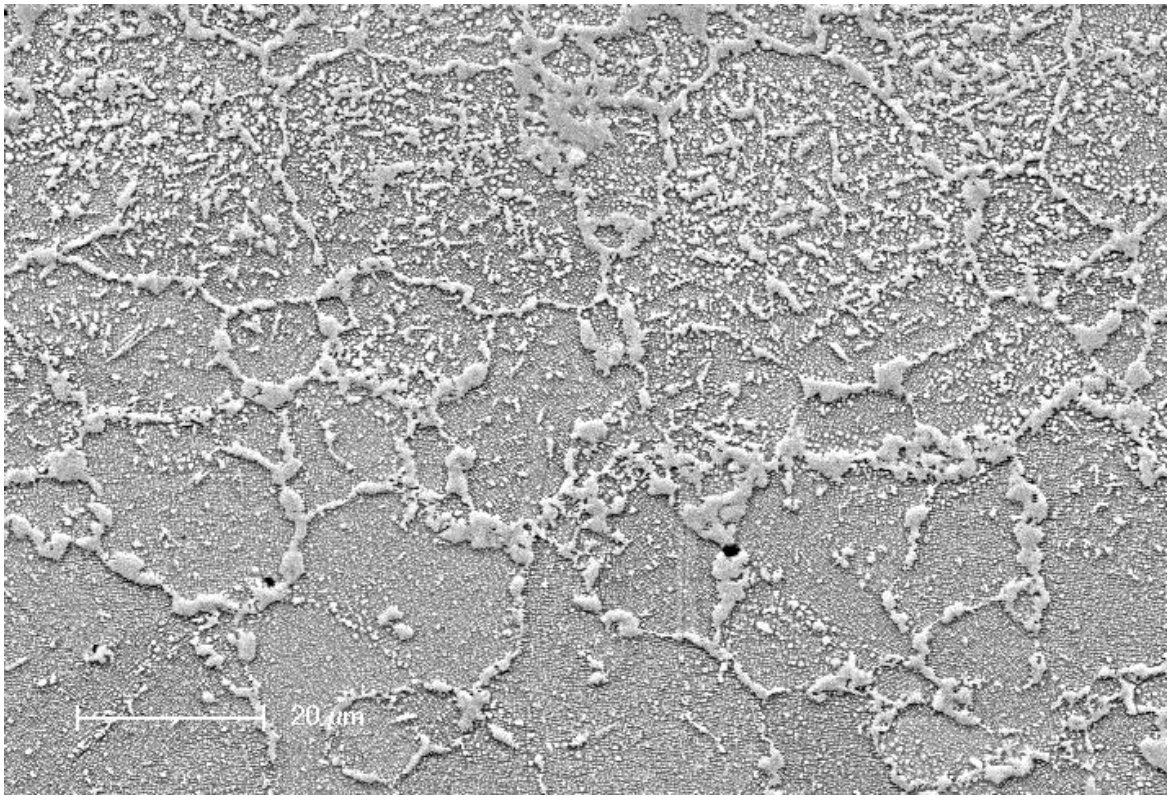

Figure 3.12. SEM photo of the boundary between the third and fourth coatings after the precipitate etchant applied.

Position 26 (2050 microns) is the boundary between the fourth coating and the base metal. From 27 to 37 (2090 to 3810 microns), composition data for metal is available. The final position is at the cooling channel surface (3820 microns). This position is shown in Figure 3.13 showing the SEM photo taken before the precipitate etching. SEM photo taken at the cooling channel surface after precipitate etching is given in Figure 3.14. A precipitate free region in the matrix is observed close to the cooling channel surface.

Figure 3.15 shows the SEM photo after the precipitate etching at the boundary of the fourth coating and the base metal. The boundary is at the bottom of the picture. Similar to the base metal, precipitates are seen in the fourth coating.

Figure 3.16 shows the mentioned coatings from the suction side, root section, leading edge, z surface specimen. It can be seen in the figure that the fourth layer is composed by a combination of thin layers.

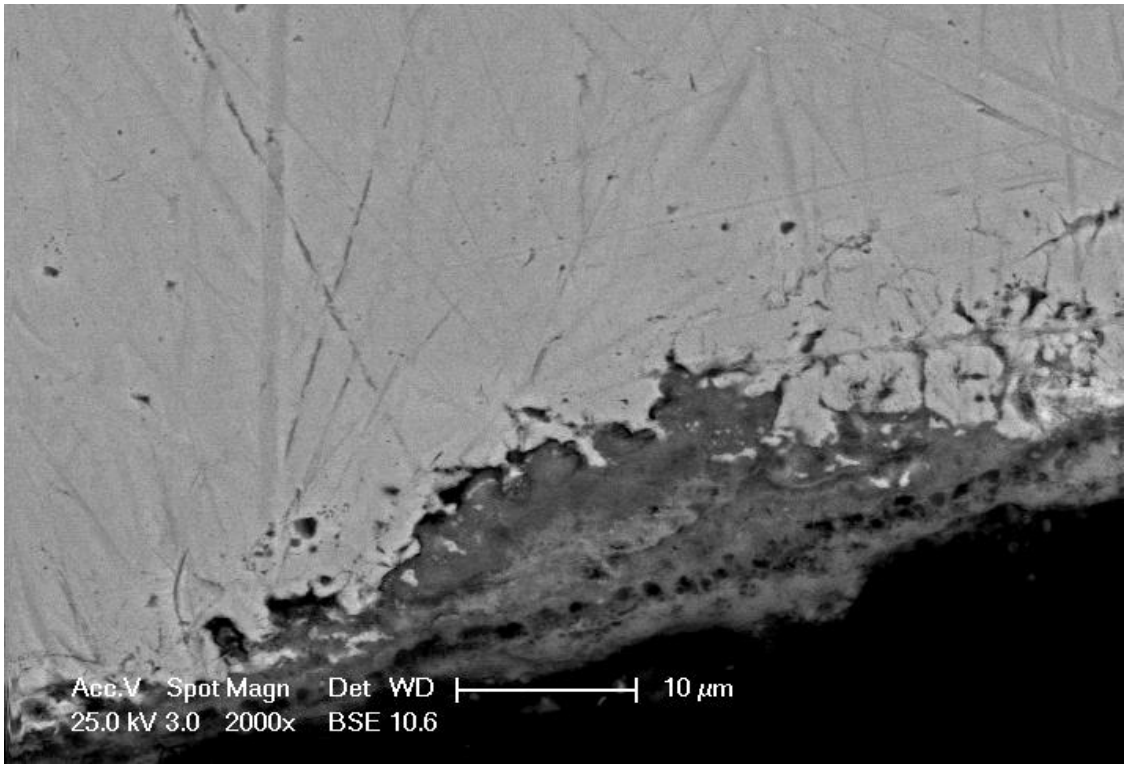

Figure 3.13. SEM photo of the cooling channel surface before the precipitate etchant applied.

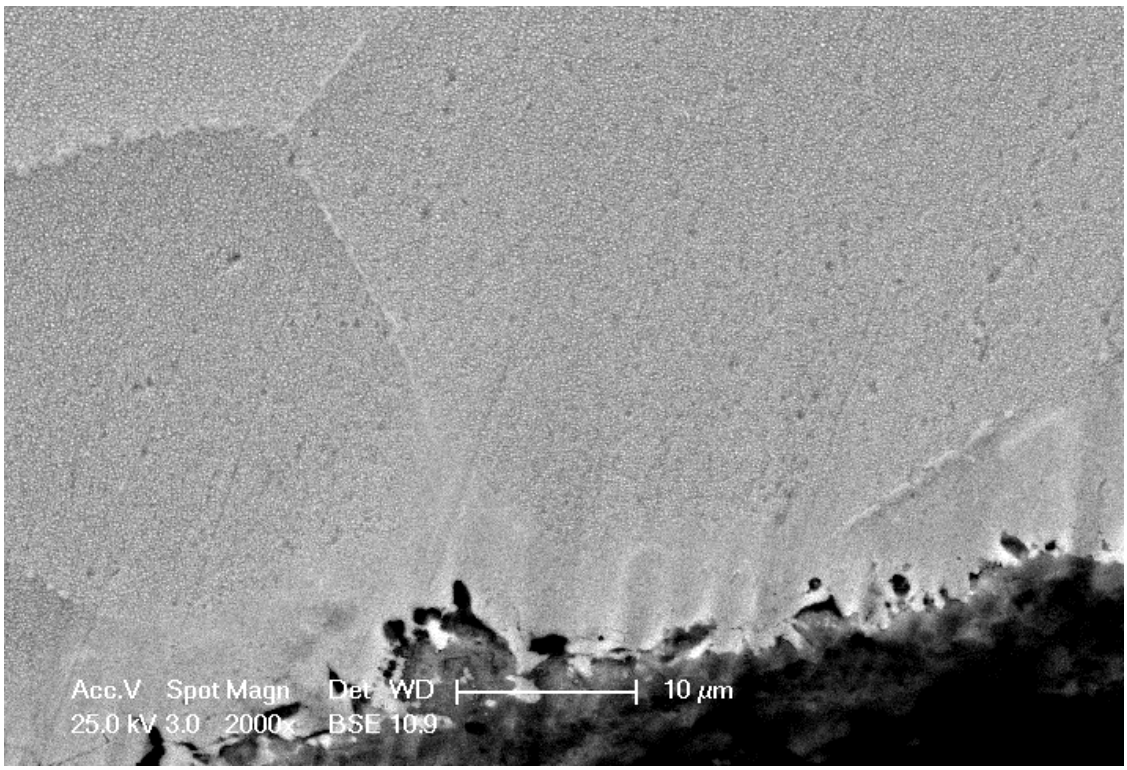

Figure 3.14. Precipitate free region close to the cooling channel surface after the precipitate etchant applied.

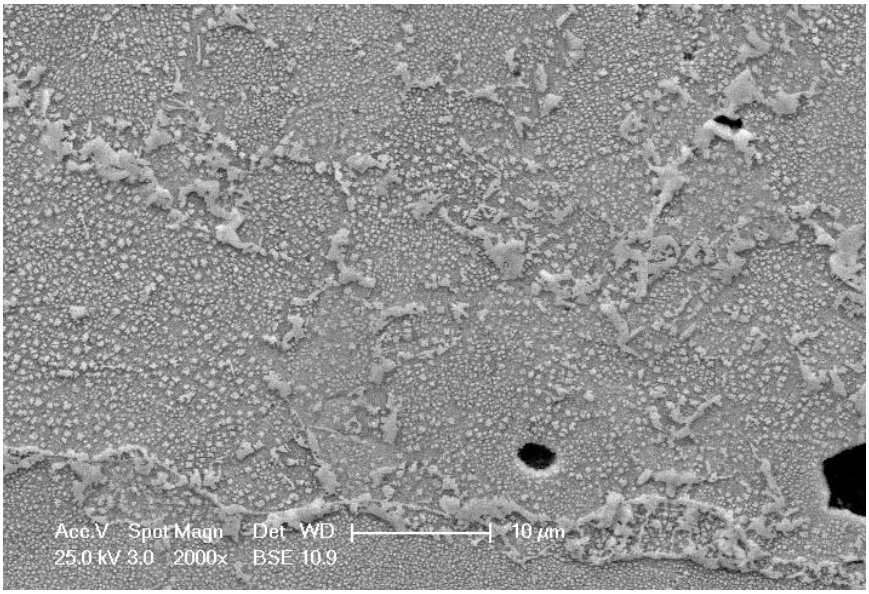

Figure 3.15. SEM photo of the boundary between the fourth coating and the base metal after the precipitate etchant applied. Base metal is seen below the scale bar.

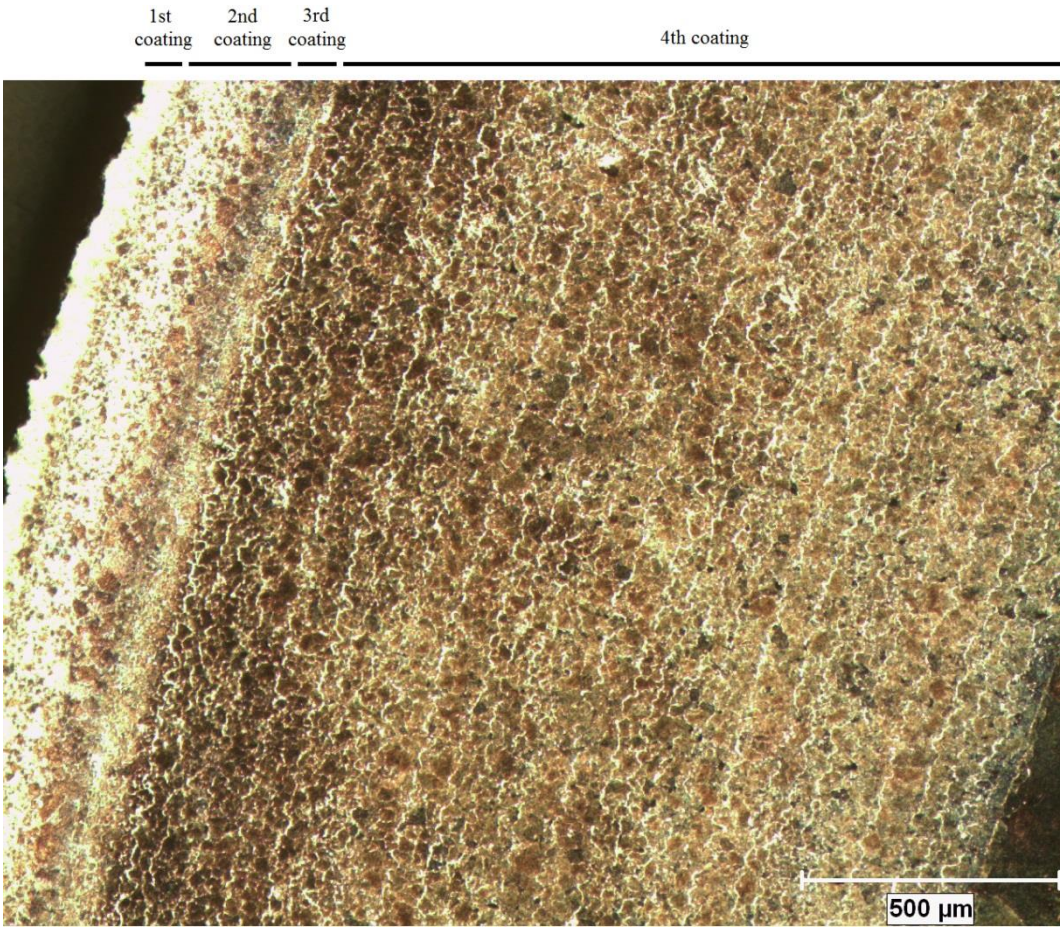

Figure 3.16. Coatings in the suction side root section leading edge z surface specimen (B80SRLZ).

Figure 3.17 gives a combined series of SEM photos showing all the coatings in detail after precipitate etching. It should be noted that the distance from the TBC to the cooling channel surface in Figures 3.6 and 3.17 are different. The paths analyzed in these figures are different, however, their positions are close to each other and they accurately show the coatings.

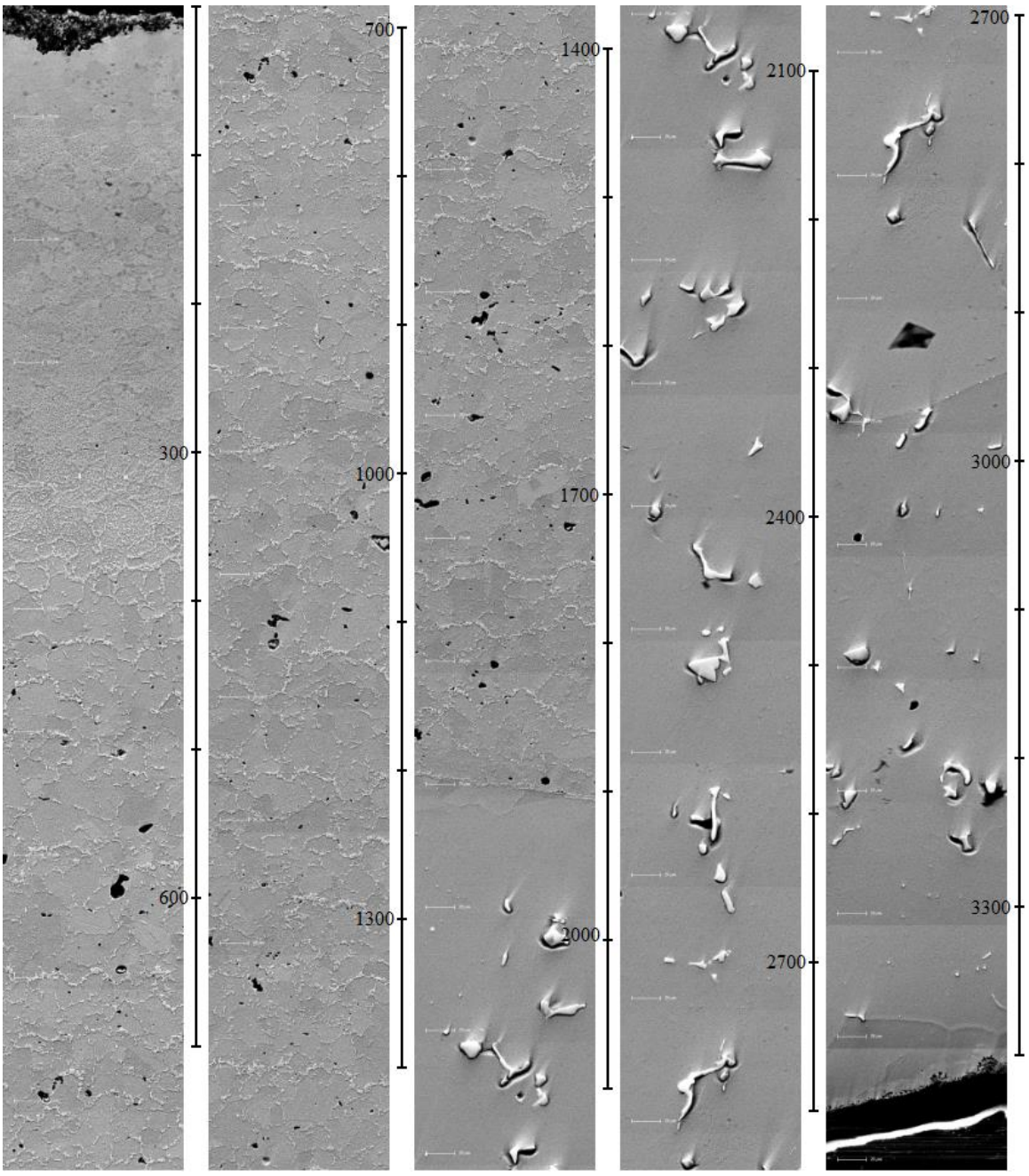

Figure 3.17. SEM photos of the coatings and the metal after precipitate etching.

The composition in terms of element weight percent vs. position data can be found in Figures 3.18, 3.19, 3.20, and 3.21. The composition in terms of atomic percent vs. position is given in Figures 3.22, 3.23, 3.24, and 3.25. Also, the weight and atomic percent compositions of elements in determined positions are given in Tables 3.2 and 3.3 respectively.

In the thermal barrier coating, amounts of aluminum, oxygen, carbon, and yttrium (≈ 2 wt %) are high. In the first coating, amount of these elements decreases, but the amount of nickel and chromium increases to 60 wt % and 12 wt %, respectively. The amount of nickel is lower in the second coating (52 wt %) and fourth coating (42 wt %) than the first coating (60 wt %). The amount of nickel in the base metal is almost the same as in the fourth coating. A gradual increase in the amount of cobalt happens in the third coating; less than 1 wt % in the first and second coatings, becomes 16 wt % in the fourth coating. Cobalt amount in the fourth layer and base metal are almost the same. Chromium composition is about 3 wt % in the TBC, it increases to 12 wt % in the first coating, becomes 20 wt % in the second coating. It gradually decreases in the third coating, becomes 17 wt % in the fourth coating, and then becomes 20 wt % in the base metal. Amount of aluminum is about 4-5 wt % in the first and second coatings, it gradually decreases in the third coating, becomes 2 wt % at the fourth coating and remains the same at the base metal. At 2050 micron position, which is the boundary between the fourth coating and the base metal, amount of molybdenum is the highest, 11.75 weight percent. Also, a decrease in the amounts of nickel and cobalt is observed at this point. The amount of tantalum is 4 wt % at the TBC, it rises to 11 wt % in the first coating, decreases to 8 wt % in the second coating and 7 wt % in the third coating. It further decreases to 3 wt % in the fourth coating. It jumps to 5 wt % at the boundary between the fourth coating and the base metal, and it is between 2-3 wt % in the base metal. The amount of titanium is less than 1 wt % in the TBC and first two coatings. It gradually increases in the third coating, becomes 4 wt % in the fourth coating, attains a maximum (6.5 wt %) at the boundary between the fourth coating and base metal, and drops to 3 wt % in the base metal. The amount of tungsten is less than 1 wt % in the TBC and first two coatings, similar to titanium. It increases to 3 wt % at the third coating and remains between 2-3 wt % in the fourth coating and the base metal. At the final point which is 3820 micron, amounts of nickel and cobalt critically decrease. An increase in the amounts of chromium and oxygen occurs.

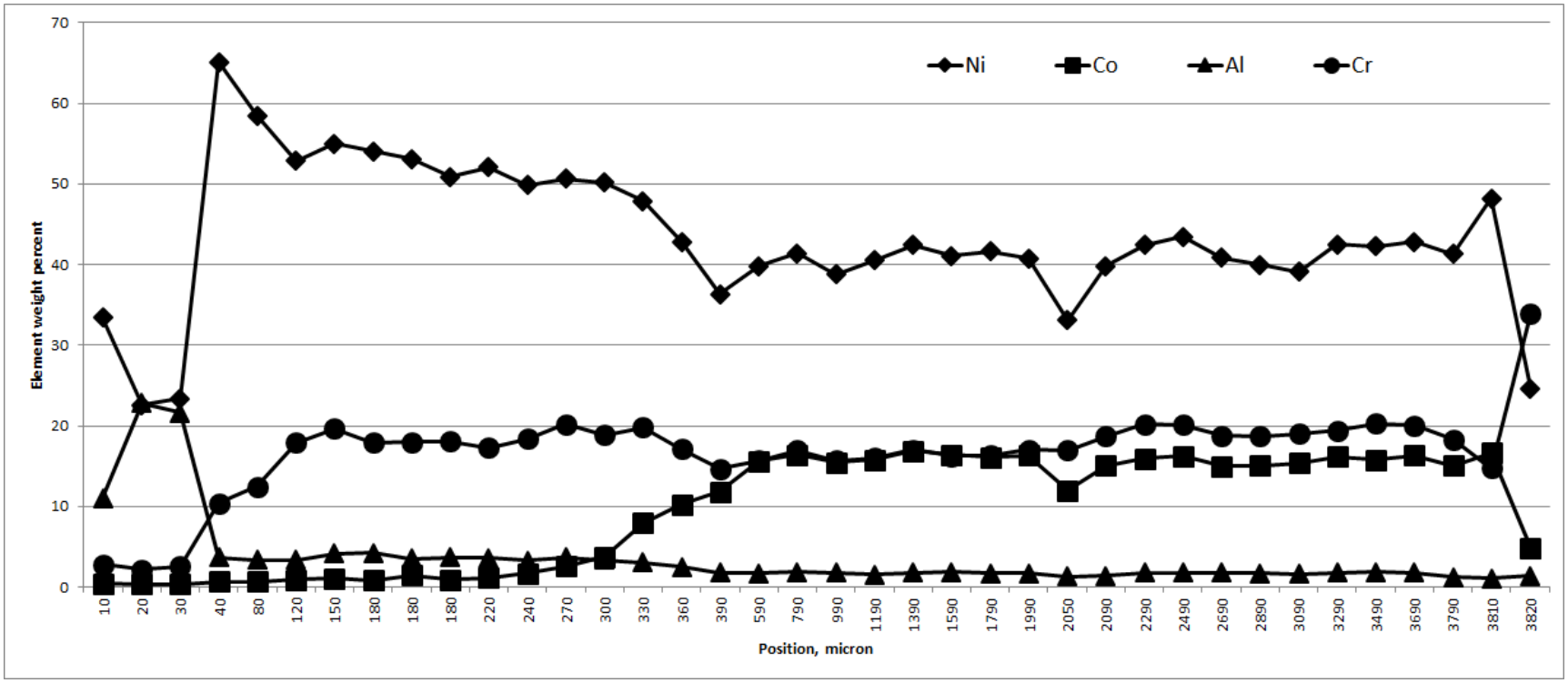

Figure 3.18. Weight percent of elements Ni, Co, Al, and Cr.

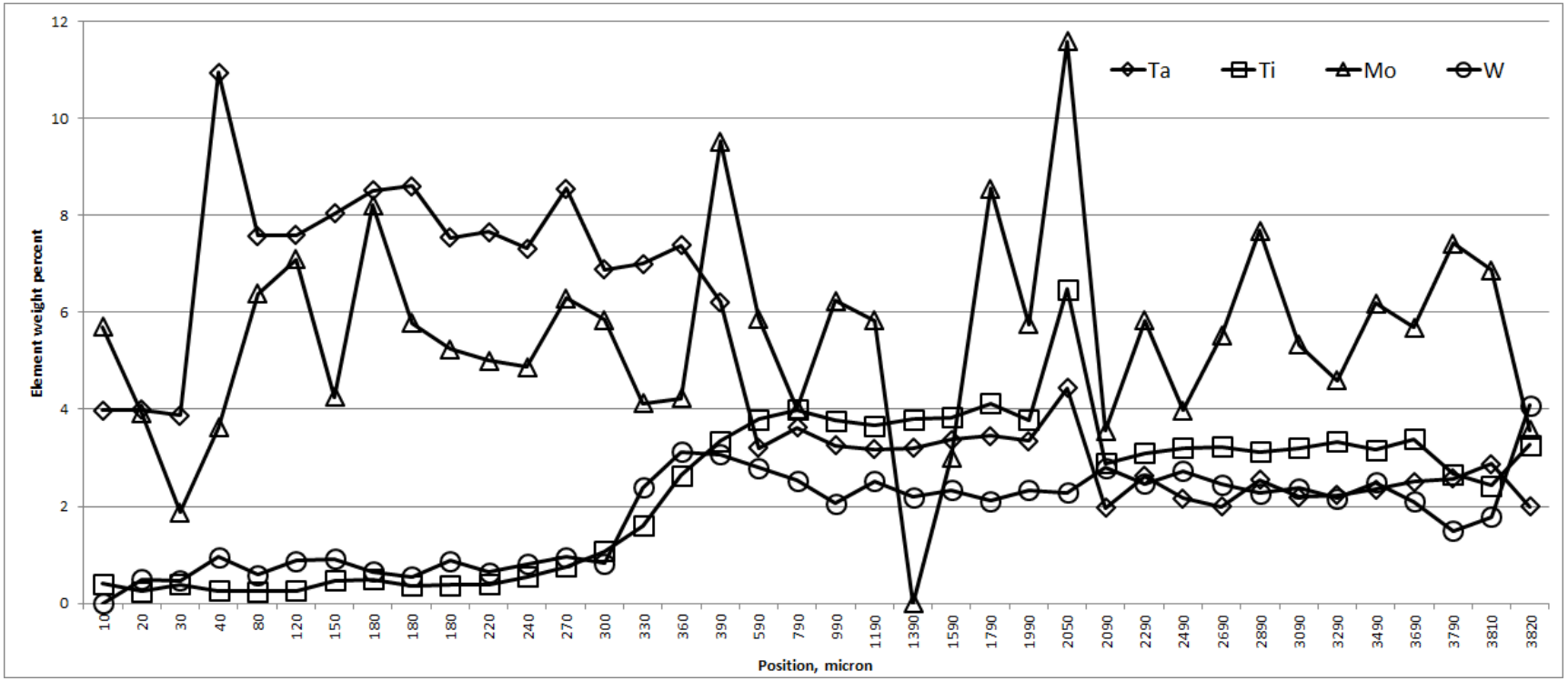

Figure 3.19. Weight percent of elements Ta, Ti, Mo, and W.

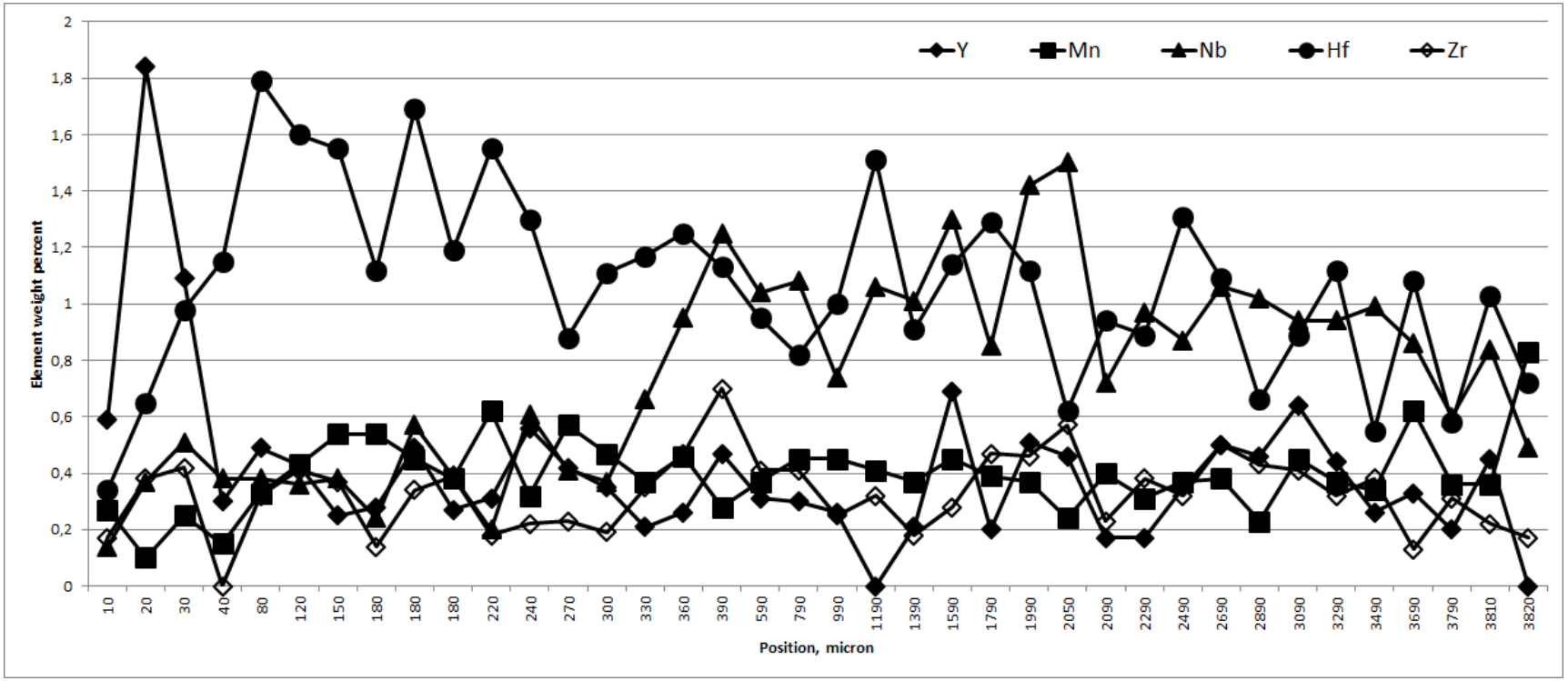

Figure 3.20. Weight percent of elements Y, Mn, Nb, Hf, and Zr.

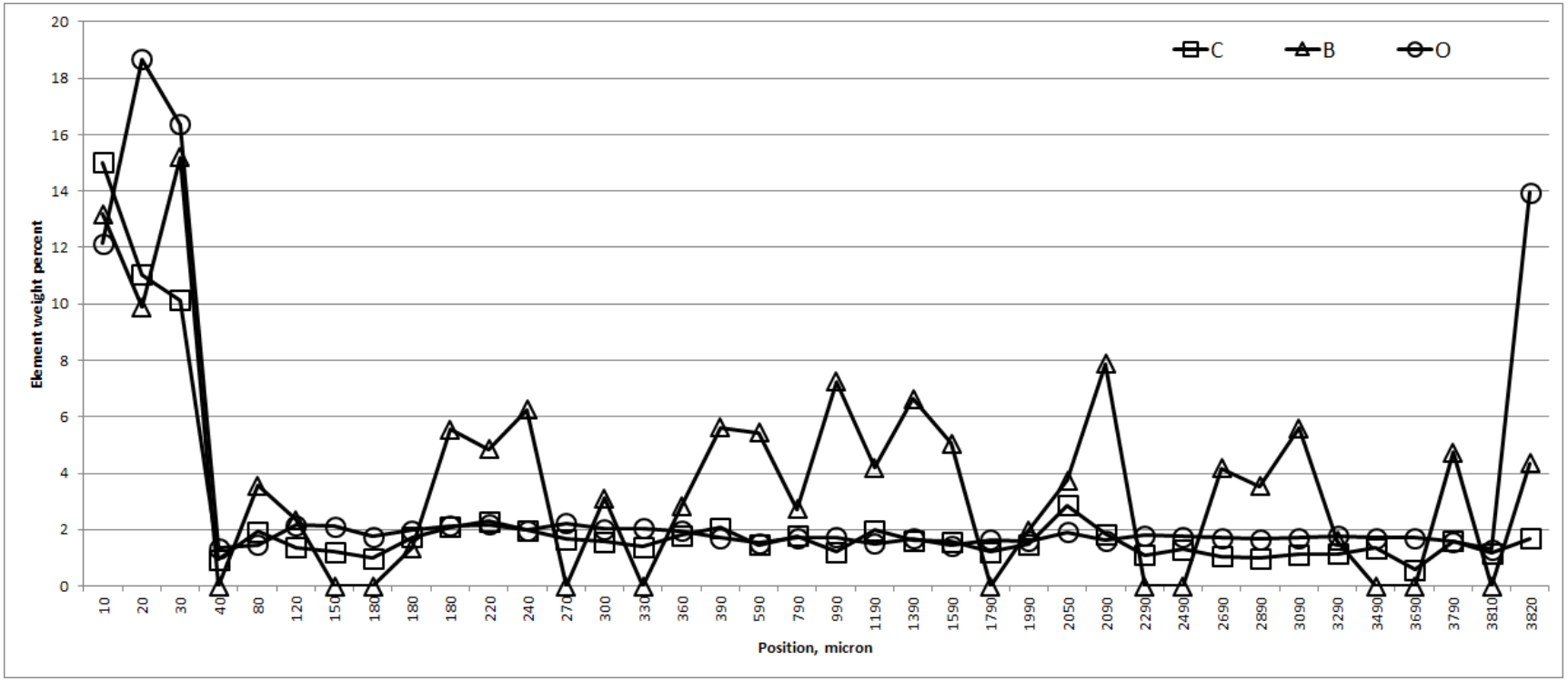

Figure 3.21. Weight percent of elements C, B, and O.

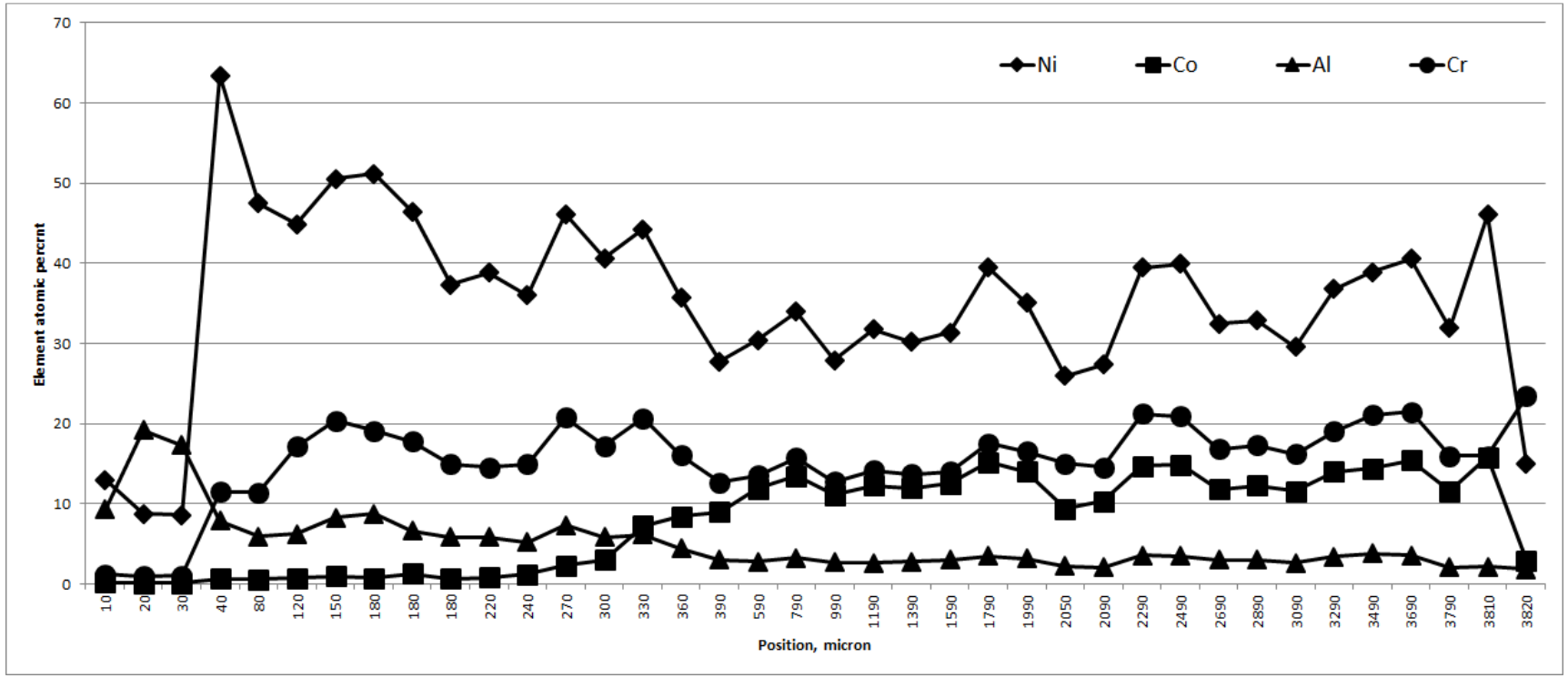

Figure 3.22. Atomic percent of elements Ni, Co, Al, and Cr.

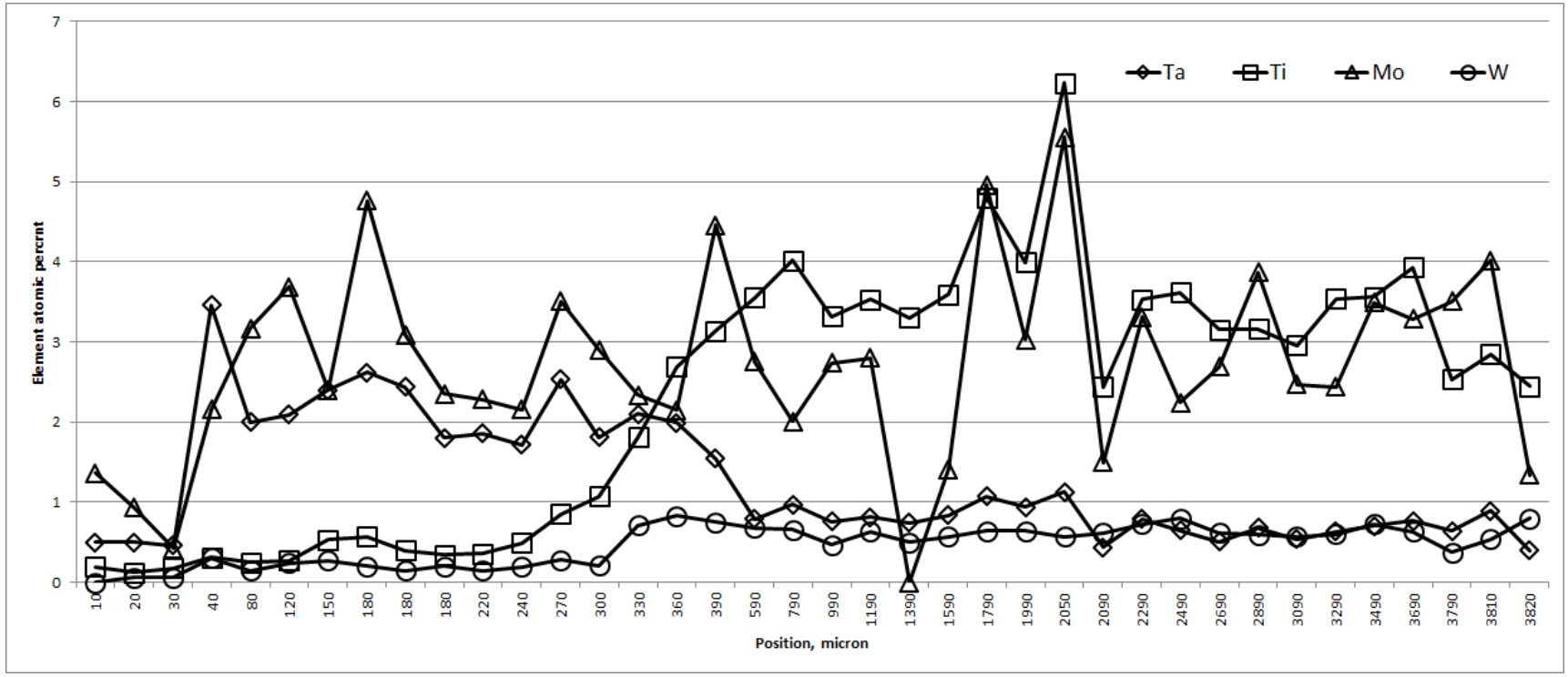

Figure 3.23. Atomic percent of elements Ta, Ti, Mo, and W.

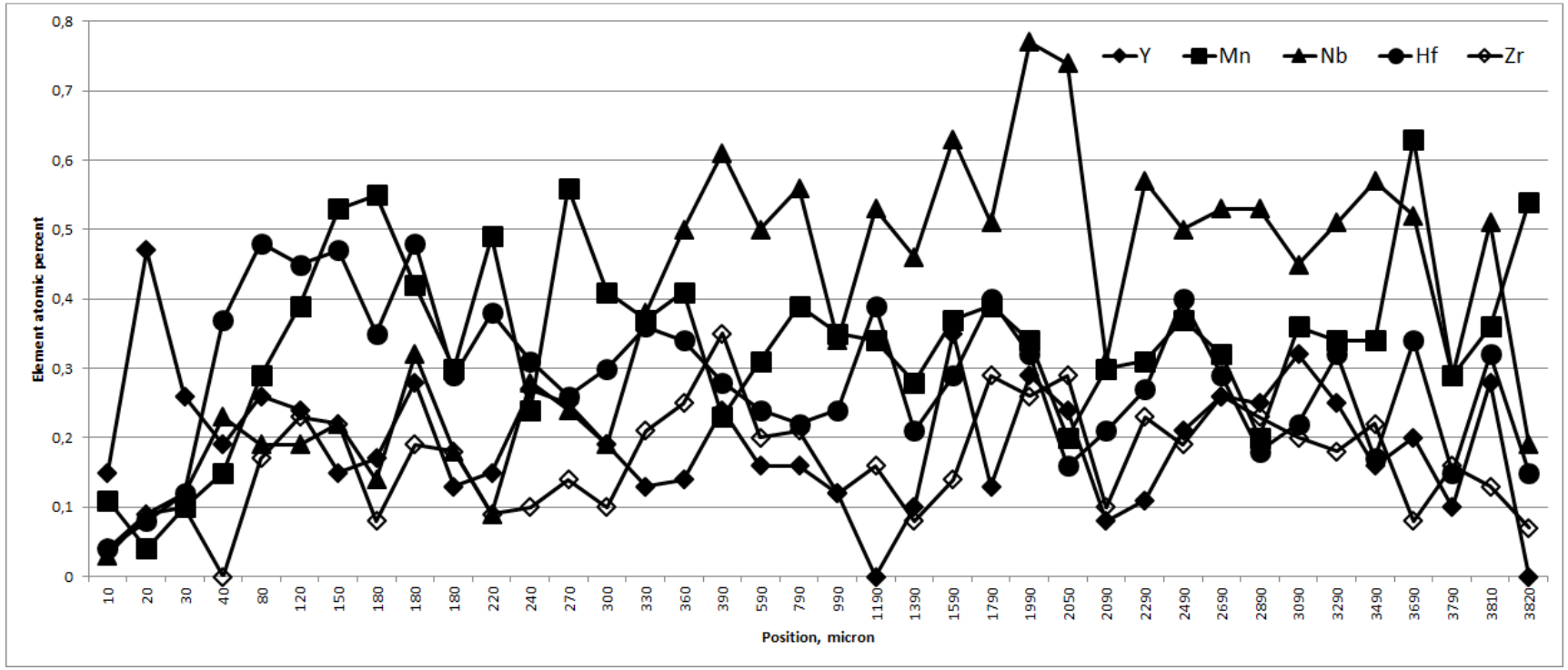

Figure 3.24. Atomic percent of elements Y, Mn, Nb, Hf, and Zr.

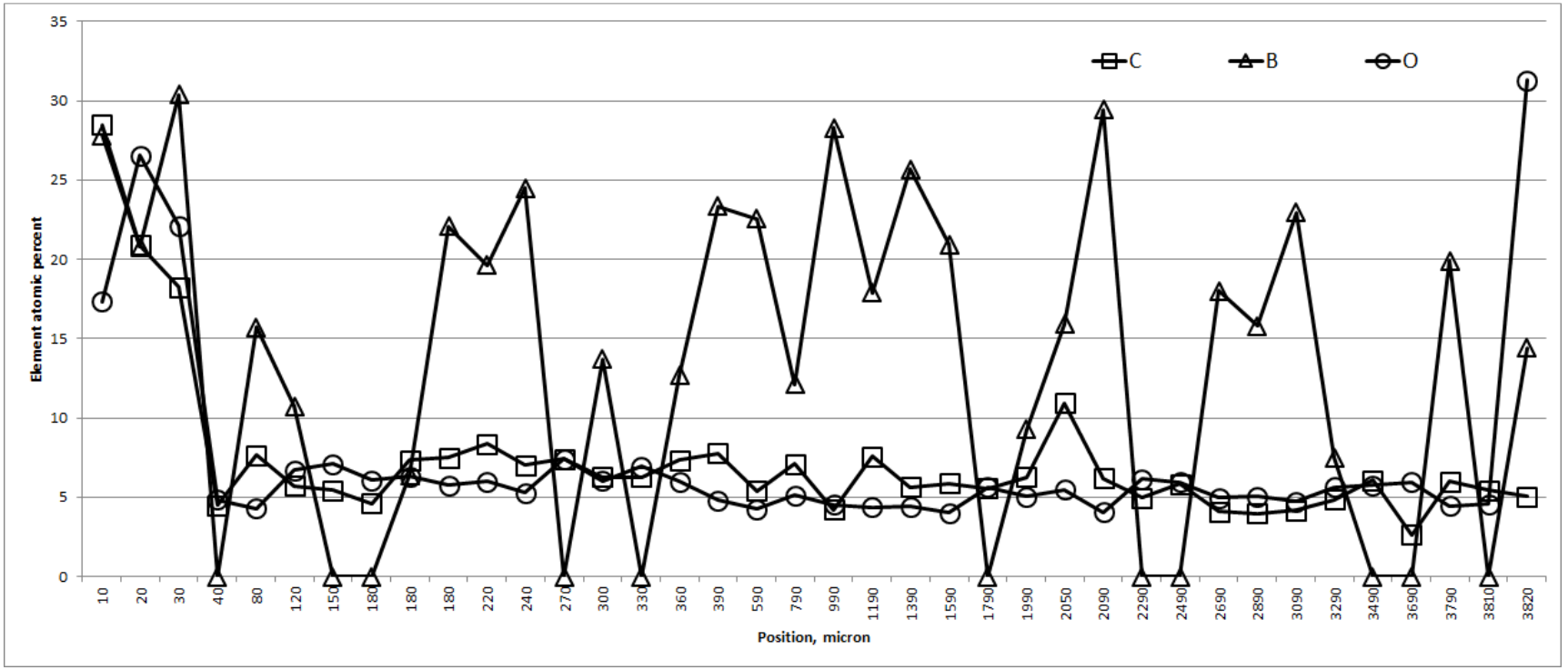

Figure 3.25. Atomic percent of elements C, B, and O.

Table 3.2. Element weight percent vs. position.

Position		Element weight percent															
No	μm	B	C	O	Al	Ta	W	Y	Zr	Nb	Ti	Cr	Mn	Co	Ni	Hf	Mo
1	10	13	15	12	11	4	0	0.6	0.2	0.1	0.4	2.8	0.3	0.4	33	0.3	5.7
2	20	9.9	11	19	23	4	0.5	1.8	0.4	0.4	0.3	2.2	0.1	0.4	23	0.7	3.9
3	30	15	10	16	22	3.9	0.5	1.1	0.4	0.5	0.4	2.6	0.3	0.4	23	1	1.9
4	40	0	1	1.4	3.7	11	1	0.3	0	0.4	0.3	10	0.2	0.7	65	1.2	3.6
5	80	3.6	1.9	1.5	3.4	7.6	0.6	0.5	0.3	0.4	0.3	12	0.3	0.7	58	1.8	6.4
6	120	2.3	1.4	2.2	3.4	7.6	0.9	0.4	0.4	0.4	0.3	18	0.4	0.9	53	1.6	7.1
7	150	0	1.2	2.1	4.1	8	0.9	0.3	0.4	0.4	0.5	20	0.5	1.1	55	1.6	4.3
8	180	0	1	1.8	4.3	8.5	0.7	0.3	0.1	0.2	0.5	18	0.5	0.8	54	1.1	8.2
9	180	1.4	1.7	2	3.5	8.6	0.6	0.5	0.3	0.6	0.4	18	0.5	1.5	53	1.7	5.8
10	180	5.5	2.1	2.1	3.7	7.5	0.9	0.3	0.4	0.4	0.4	18	0.4	0.9	51	1.2	5.2
11	220	4.8	2.3	2.2	3.6	7.7	0.6	0.3	0.2	0.2	0.4	17	0.6	1.2	52	1.6	5
12	240	6.2	2	2	3.3	7.3	0.8	0.6	0.2	0.6	0.6	18	0.3	1.7	50	1.3	4.9
13	270	0	1.7	2.2	3.7	8.6	1	0.4	0.2	0.4	0.8	20	0.6	2.6	51	0.9	6.3
14	300	3.1	1.6	2	3.3	6.9	0.8	0.4	0.2	0.4	1.1	19	0.5	3.8	50	1.1	5.9
15	330	0	1.4	2.1	3.1	7	2.4	0.2	0.4	0.7	1.6	20	0.4	7.9	48	1.2	4.1
16	360	2.8	1.8	2	2.5	7.4	3.1	0.3	0.5	1	2.6	17	0.5	10	43	1.3	4.2
17	390	5.6	2.1	1.7	1.8	6.2	3.1	0.5	0.7	1.3	3.4	15	0.3	12	36	1.1	9.5
18	590	5.4	1.5	1.5	1.7	3.2	2.8	0.3	0.4	1	3.8	16	0.4	16	40	1	5.9
19	790	2.7	1.8	1.7	1.8	3.6	2.5	0.3	0.4	1.1	4	17	0.5	16	41	0.8	4
20	990	7.2	1.2	1.7	1.8	3.3	2.1	0.3	0.3	0.7	3.8	16	0.5	15	39	1	6.2
21	1190	4.2	2	1.5	1.6	3.2	2.5	0	0.3	1.1	3.7	16	0.4	16	41	1.5	5.8
22	1390	6.6	1.6	1.7	1.8	3.2	2.2	0.2	0.2	1	3.8	17	0.4	17	42	0.9	0
23	1590	5	1.6	1.4	1.8	3.4	2.3	0.7	0.3	1.3	3.8	16	0.5	16	41	1.1	3
24	1790	0	1.2	1.6	1.7	3.5	2.1	0.2	0.5	0.9	4.1	16	0.4	16	42	1.3	8.6
25	1990	2	1.5	1.6	1.7	3.4	2.3	0.5	0.5	1.4	3.8	17	0.4	16	41	1.1	5.8
26	2050	3.7	2.9	1.9	1.3	4.4	2.3	0.5	0.6	1.5	6.5	17	0.2	12	33	0.6	12
27	2090	7.9	1.8	1.6	1.4	2	2.8	0.2	0.2	0.7	2.9	19	0.4	15	40	0.9	3.6
28	2290	0	1.1	1.8	1.8	2.6	2.5	0.2	0.4	1	3.1	20	0.3	16	42	0.9	5.8
29	2490	0	1.3	1.8	1.8	2.2	2.7	0.4	0.3	0.9	3.2	20	0.4	16	43	1.3	4
30	2690	4.2	1.1	1.7	1.8	2	2.5	0.5	0.5	1.1	3.2	19	0.4	15	41	1.1	5.5
31	2890	3.5	1	1.7	1.7	2.5	2.3	0.5	0.4	1	3.1	19	0.2	15	40	0.7	7.7
32	3090	5.6	1.1	1.7	1.6	2.2	2.4	0.6	0.4	0.9	3.2	19	0.5	15	39	0.9	5.3
33	3290	1.6	1.2	1.8	1.8	2.2	2.2	0.4	0.3	0.9	3.3	19	0.4	16	42	1.1	4.6
34	3490	0	1.4	1.7	1.9	2.4	2.5	0.3	0.4	1	3.2	20	0.3	16	42	0.6	6.2
35	3690	0	0.6	1.7	1.8	2.5	2.1	0.3	0.1	0.9	3.4	20	0.6	16	43	1.1	5.7
36	3790	4.7	1.6	1.6	1.2	2.6	1.5	0.2	0.3	0.6	2.7	18	0.4	15	41	0.6	7.4
37	3810	0	1.2	1.3	1.1	2.9	1.8	0.5	0.2	0.8	2.4	15	0.4	17	48	1	6.9
38	3820	4.3	1.7	14	1.4	2	4.1	0	0.2	0.5	3.3	34	0.8	4.9	25	0.7	3.6

Table 3.3. Element atomic percent vs. position.

Position		Element atomic percent															
No	μm	B	C	O	Al	Ta	W	Y	Zr	Nb	Ti	Cr	Mn	Co	Ni	Hf	Mo
1	10	28	28	17	9.3	0.5	0	0.2	0	0	0.2	1.2	0.1	0.2	13	0	1.4
2	20	21	21	27	19	0.5	0.1	0.5	0.1	0.1	0.1	1	0	0.1	8.7	0.1	0.9
3	30	30	18	22	17	0.5	0.1	0.3	0.1	0.1	0.2	1.1	0.1	0.1	8.6	0.1	0.4
4	40	0	4.5	4.8	7.9	3.5	0.3	0.2	0	0.2	0.3	11	0.2	0.7	63	0.4	2.2
5	80	16	7.7	4.3	5.9	2	0.2	0.3	0.2	0.2	0.3	11	0.3	0.6	47	0.5	3.2
6	120	11	5.7	6.7	6.3	2.1	0.2	0.2	0.2	0.2	0.3	17	0.4	0.8	45	0.5	3.7
7	150	0	5.4	7.1	8.3	2.4	0.3	0.2	0.2	0.2	0.5	20	0.5	1	51	0.5	2.4
8	180	0	4.6	6.1	8.8	2.6	0.2	0.2	0.1	0.1	0.6	19	0.6	0.8	51	0.4	4.8
9	180	6.4	7.4	6.3	6.7	2.4	0.2	0.3	0.2	0.3	0.4	18	0.4	1.3	46	0.5	3.1
10	180	22	7.5	5.8	5.9	1.8	0.2	0.1	0.2	0.2	0.3	15	0.3	0.7	37	0.3	2.4
11	220	20	8.4	6	5.8	1.9	0.2	0.2	0.1	0.1	0.4	15	0.5	0.9	39	0.4	2.3
12	240	24	7	5.3	5.2	1.7	0.2	0.3	0.1	0.3	0.5	15	0.2	1.2	36	0.3	2.2
13	270	0	7.4	7.4	7.3	2.5	0.3	0.3	0.1	0.2	0.9	21	0.6	2.3	46	0.3	3.5
14	300	14	6.3	6	5.9	1.8	0.2	0.2	0.1	0.2	1.1	17	0.4	3.1	41	0.3	2.9
15	330	0	6.3	6.9	6.2	2.1	0.7	0.1	0.2	0.4	1.8	21	0.4	7.3	44	0.4	2.3
16	360	13	7.3	6	4.5	2	0.8	0.1	0.3	0.5	2.7	16	0.4	8.5	36	0.3	2.2
17	390	23	7.8	4.8	3	1.5	0.8	0.2	0.4	0.6	3.1	13	0.2	9	28	0.3	4.5
18	590	23	5.4	4.2	2.8	0.8	0.7	0.2	0.2	0.5	3.6	14	0.3	12	30	0.2	2.8
19	790	12	7.1	5.1	3.3	1	0.7	0.2	0.2	0.6	4	16	0.4	13	34	0.2	2
20	990	28	4.2	4.5	2.7	0.8	0.5	0.1	0.1	0.3	3.3	13	0.4	11	28	0.2	2.7
21	1190	18	7.6	4.4	2.7	0.8	0.6	0	0.2	0.5	3.5	14	0.3	12	32	0.4	2.8
22	1390	26	5.6	4.4	2.8	0.7	0.5	0.1	0.1	0.5	3.3	14	0.3	12	30	0.2	0
23	1590	21	5.9	4	3	0.8	0.6	0.4	0.1	0.6	3.6	14	0.4	13	31	0.3	1.4
24	1790	0	5.6	5.7	3.5	1.1	0.6	0.1	0.3	0.5	4.8	18	0.4	15	39	0.4	5
25	1990	9.3	6.3	5.1	3.2	0.9	0.6	0.3	0.3	0.8	4	17	0.3	14	35	0.3	3
26	2050	16	11	5.5	2.3	1.1	0.6	0.2	0.3	0.7	6.2	15	0.2	9.4	26	0.2	5.6
27	2090	29	6.2	4.1	2.1	0.4	0.6	0.1	0.1	0.3	2.4	15	0.3	10	27	0.2	1.5
28	2290	0	5	6.2	3.6	0.8	0.7	0.1	0.2	0.6	3.5	21	0.3	15	39	0.3	3.3
29	2490	0	5.8	5.9	3.5	0.7	0.8	0.2	0.2	0.5	3.6	21	0.4	15	40	0.4	2.2
30	2690	18	4.1	5	3	0.5	0.6	0.3	0.3	0.5	3.2	17	0.3	12	33	0.3	2.7
31	2890	16	4	5	3	0.7	0.6	0.3	0.2	0.5	3.2	17	0.2	12	33	0.2	3.9
32	3090	23	4.2	4.7	2.7	0.5	0.6	0.3	0.2	0.5	3	16	0.4	12	30	0.2	2.5
33	3290	7.5	4.9	5.6	3.4	0.6	0.6	0.3	0.2	0.5	3.5	19	0.3	14	37	0.3	2.4
34	3490	0	6.1	5.8	3.8	0.7	0.7	0.2	0.2	0.6	3.6	21	0.3	14	39	0.2	3.5
35	3690	0	2.6	5.9	3.6	0.8	0.6	0.2	0.1	0.5	3.9	21	0.6	15	41	0.3	3.3
36	3790	20	6	4.5	2.1	0.6	0.4	0.1	0.2	0.3	2.5	16	0.3	12	32	0.2	3.5
37	3810	0	5.5	4.6	2.2	0.9	0.5	0.3	0.1	0.5	2.9	16	0.4	16	46	0.3	4
38	3820	14	5	31	1.9	0.4	0.8	0	0.1	0.2	2.5	23	0.5	3	15	0.2	1.3

3.2. Grain Size and Morphology

3.2.1. Grain Size

Average grain size was determined according to ASTM E112 by image J software which was developed by Research Services Branch of National Institute of Mental Health in USA [32]. Grains at the boundary in a photo of a specimen were considered as a half grain and grains not intersected by the boundary of a specimen were considered as one grain. Then, number of grains was divided into the area covered by these grains to determine an average grain size for specimens with a spherical equivalent shape assumption. Intercept method was used in some positions. Table 3.4 below shows the average grain size for predetermined positions.

Table 3.4. Average grain size in microns.

Side →		Pressure				Suction		
Positions → / Sections ↓		Trailing edge	Middle	Leading edge	Stagnation	Leading edge	Middle	Trailing edge
Tip	Hot	514	554	469	276	562	515	491
	Cold	624	1060	715	481	957	917	629
Middle	Hot	569	587	376	699	475	639	582
	Cold	696	1325	610	786	616	900	726
Root	Hot	787	509	503	522	1001	569	637
	Cold	800	1096	813	697	1378	1108	778
Firtree		923						

General observation shows that hot surface grains are finer than cold surface grains.

Along the trailing edge, both in the suction and pressure sides, the hot surface grains are finer than the cold surface grains. While moving from the tip of the blade to the root on the trailing edge, the grain size increases for both the hot and cold surfaces both in the suction and pressure sides. This behavior is given in Figure 3.26. It should be noted that

the size for the hot and cold surfaces at the pressure side root section is almost the same, while the size for these surfaces on the suction side is noticeably different.

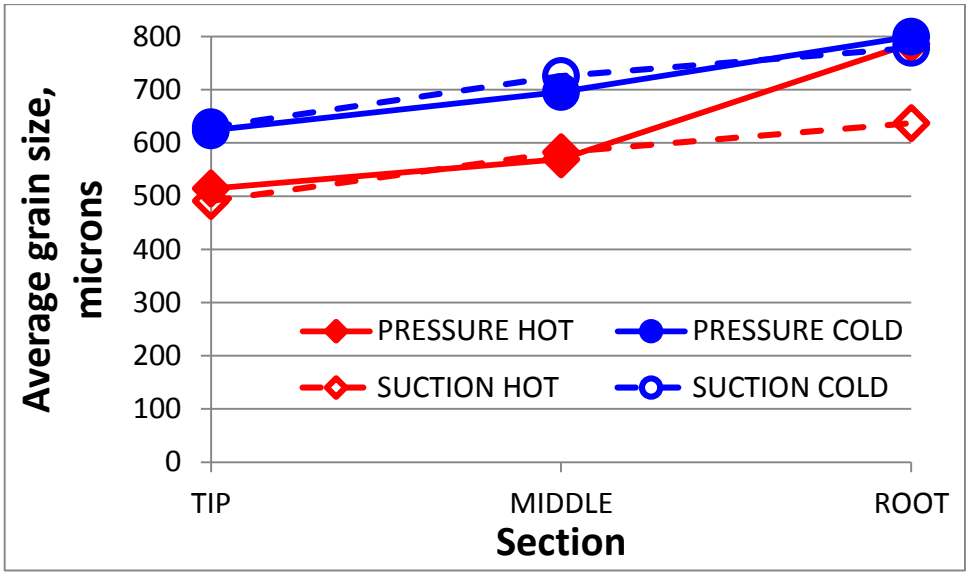

Figure 3.26. Grain size for the trailing edge.

Figure 3.27 gives the grain size in the middle position specimens. Along the middle position of the blade, the cold surface grains are coarser than the hot surface grains both in the suction and pressure sides. On the pressure side, middle section grain size is greater than the other two sections, and this is more pronounced for the cold surface. A similar trend is seen for the suction side hot surfaces, but for the cold surface of the suction side, root section has significantly larger grains than the other two sections above it. The difference in the grain size between the hot surface and cold surface for the middle position is larger compared to the trailing edge.

Figure 3.28 shows the grain size in the leading edge specimens. Both in the suction and pressure sides and in the stagnation point, the hot surface grains are finer than the cold surface grains. For both the pressure and suction sides, the middle section has the smallest grain size for both the hot and cold surfaces. However, the grains are the largest at the middle section for both the hot and cold surfaces.

Figures 3.29 to 3.31 replot the data already presented in Figures 3.26 to 3.28 containing positions for transverse planes at the three sections along the blade length, namely the tip, middle, and root.

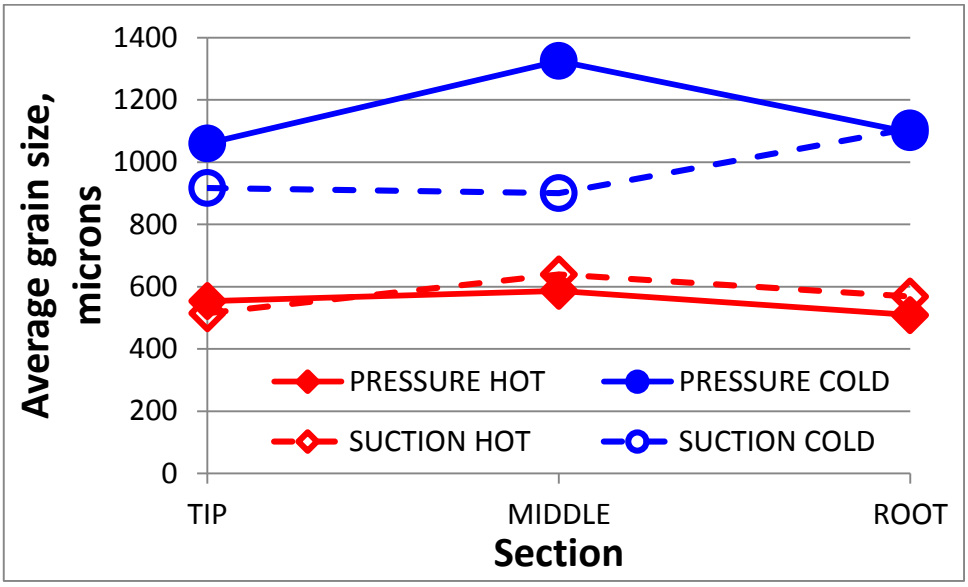

Figure 3.27. Grain size for the middle position.

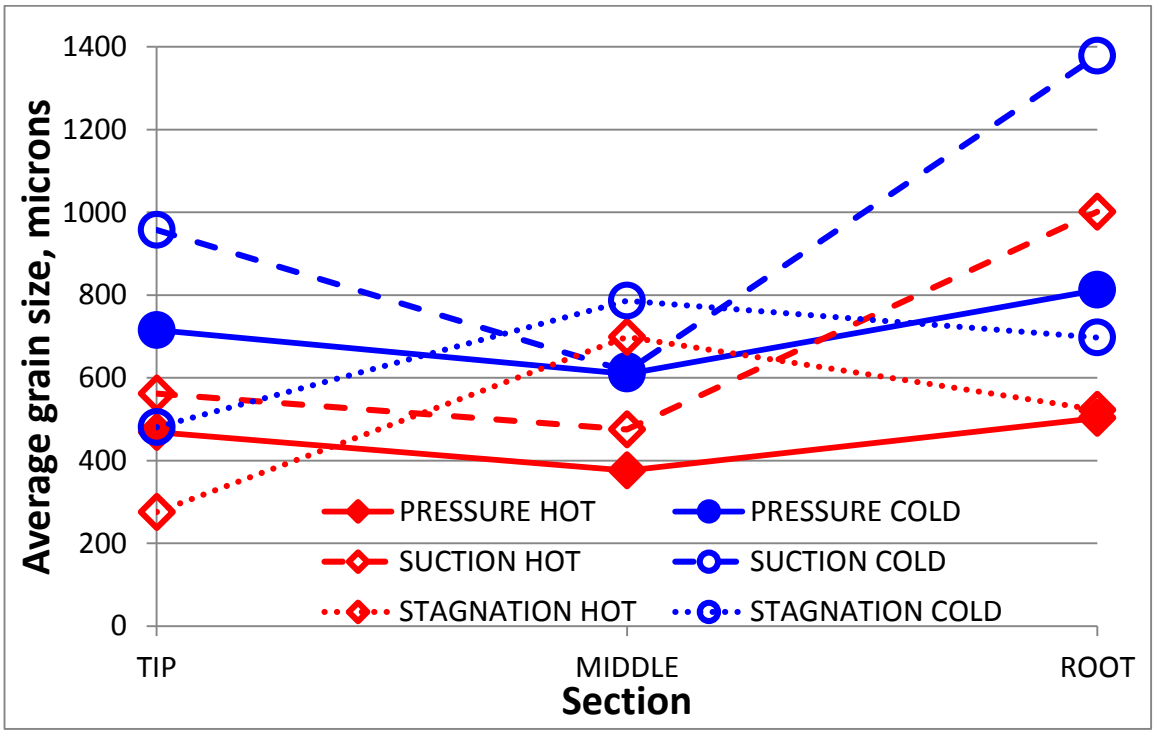

Figure 3.28. Grain size for the leading edge.

Figure 3.29 gives the grain size for the tip section specimens. The cold surface grains are coarser than the hot surface grains along the tip section. The size is the smallest in the stagnation point for both the hot and cold surfaces. In the pressure side, the grains are the largest in the middle position for both the hot and cold surfaces. However, the size is the largest for the leading edge in the suction side of both the hot and cold surfaces.

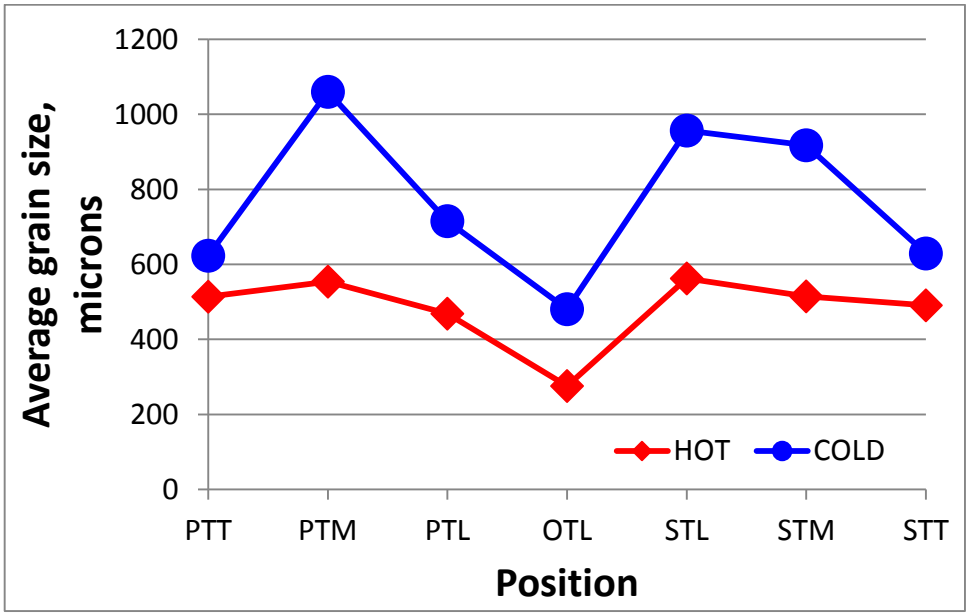

Figure 3.29. Grain size for the tip section.

The grain size for the middle section is given in Figure 3.30. The cold surface grains are larger than the hot surface grains in all positions. The middle position cold surface grains are the largest at both the pressure and suction sides. In the hot surface, the stagnation point has the largest grains. The largest grains in both the pressure and suction sides are at the middle position.

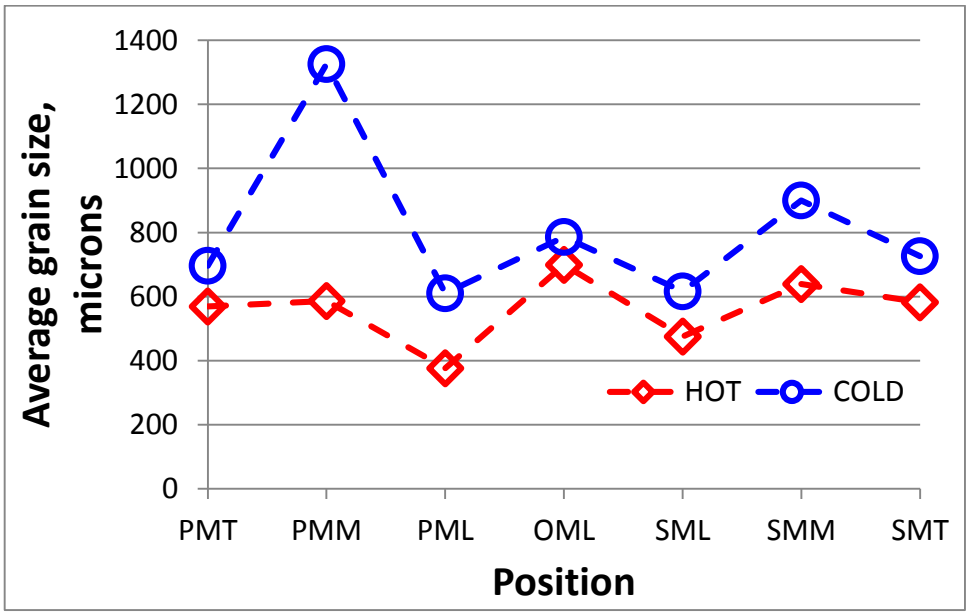

Figure 3.30. Grain size for the middle section.

The grain size for the root section specimens is illustrated in Figure 3.31. The cold surface grains are larger than the hot surface grains. The suction side leading edge specimens have the largest grain size for both the hot and cold surfaces. The grain size for the pressure side trailing edge specimens is almost equal for the hot and cold surfaces, although the grain size in the cold surface is slightly larger.

The average grain size for the firtree specimen is 0.923 mm. This size is greater than the size for the hot surface specimens in all sections.

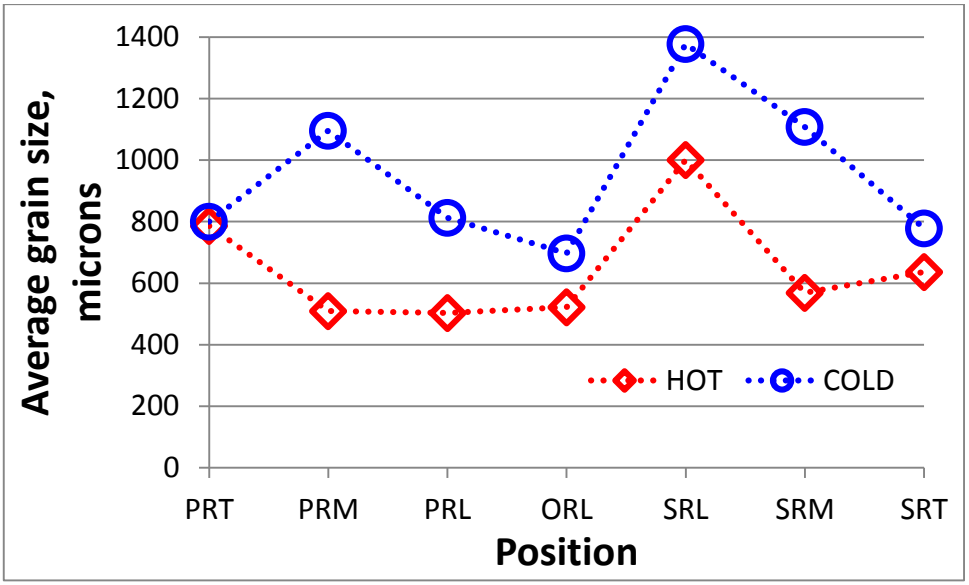

Figure 3.31. Grain size for the root section.

3.2.2. Grain Morphology

After the removal of the coatings on the hot surface with the help of grinding, the morphology of grains in the base metal was studied. It should be noted that the fourth coating includes very fine grains as seen in Figures 3.12, 3.15 and 3.16. No grain structure was observable within the other coatings.

Grains of the base metal in the hot and cold surfaces are equiaxed in shape. As already stated, cold surface grains are larger in size than the hot surface grains. In the z surface and side surface specimens, usually there are elongated grains extending from the hot surface to the cold surface.

3.2.2.1. B80-SP-TT (tip section trailing edge). In Figures 3.32 and 3.33, photographs of pressure side specimens and suction side specimens are given, respectively.

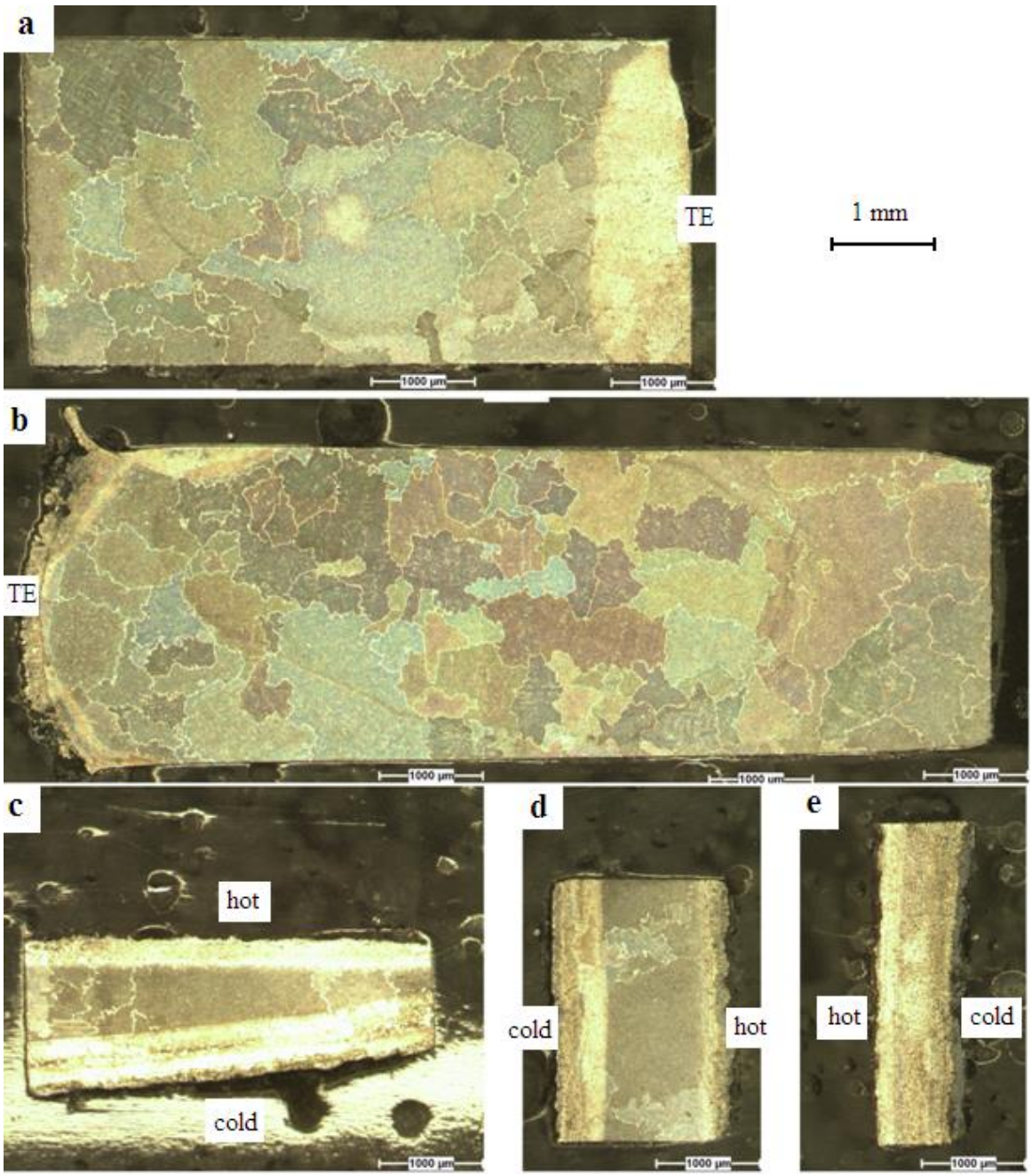

Figure 3.32. Grain morphology in PTT (Pressure side Tip section Trailing edge), a) cold surface, b) hot surface, c) z surface, d) side surface far from trailing edge, and e) side surface close to trailing edge specimens.

In the pressure side, the cold surface and hot surface specimens have equiaxed grains, with finer grains on the hot surface. There are a few number of grains in the z

surface and side surface far from trailing edge specimens, and elongated grains are not seen. Grain boundaries in the side surface close to the trailing edge specimen are not observable due to overgrinding.

In the suction side, the cold and hot surface specimens both have equiaxed grains. The grain size in the cold surface specimen is larger than that in the hot surface specimen. In the hot surface specimen, grains are finer near the trailing edge. There are fine grains at the upper part (hot surface) and coarse grains at the lower part (cold surface) in the z surface specimen. The side surface far from the trailing edge and side surface close to the trailing edge specimens have equiaxed grains. The distance between these specimens is about 15 mm and grains become finer close to the trailing edge.

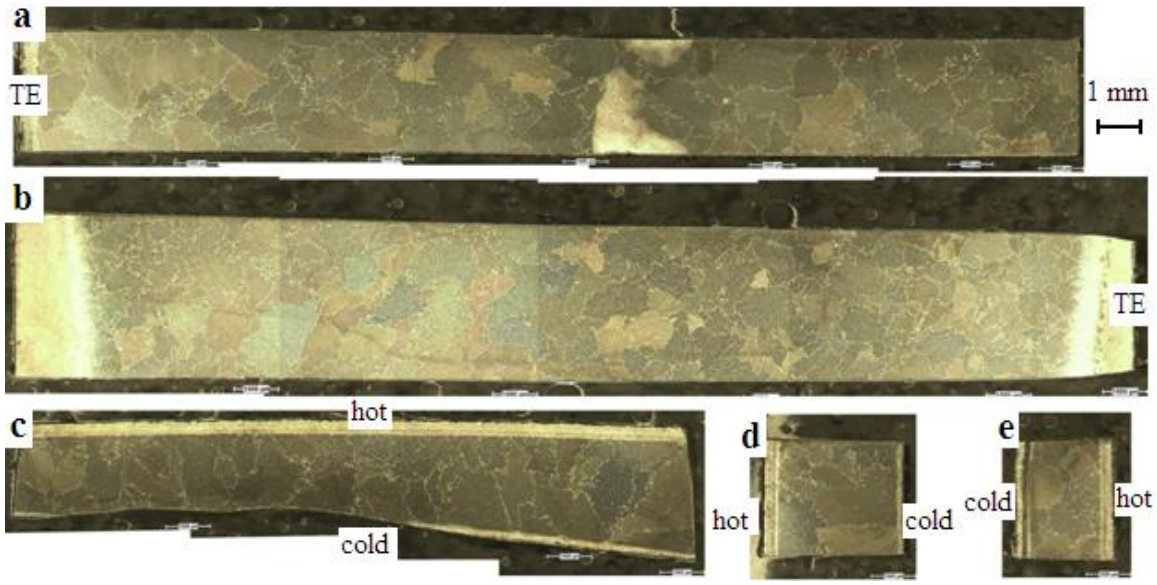

Figure 3.33. Grain morphology in STT (Suction side Tip section Trailing edge), a) cold surface, b) hot surface, c) z surface, d) side surface far from trailing edge, and e) side surface close to trailing edge specimens.

3.2.2.2. B80-SP-TM (tip section middle position). Photographs of the pressure side specimens and suction side specimens are given respectively in Figures 3.34 and 3.35.

In both the pressure and suction sides, the cold surface specimen has coarser grains than hot surface specimen. Both the cold and hot surface specimens have equiaxed grains. In the z and side surface specimens, there are elongated grains starting from the hot surface

and going to the middle part of the specimens. The grains become equiaxed and coarse close to the cold surface.

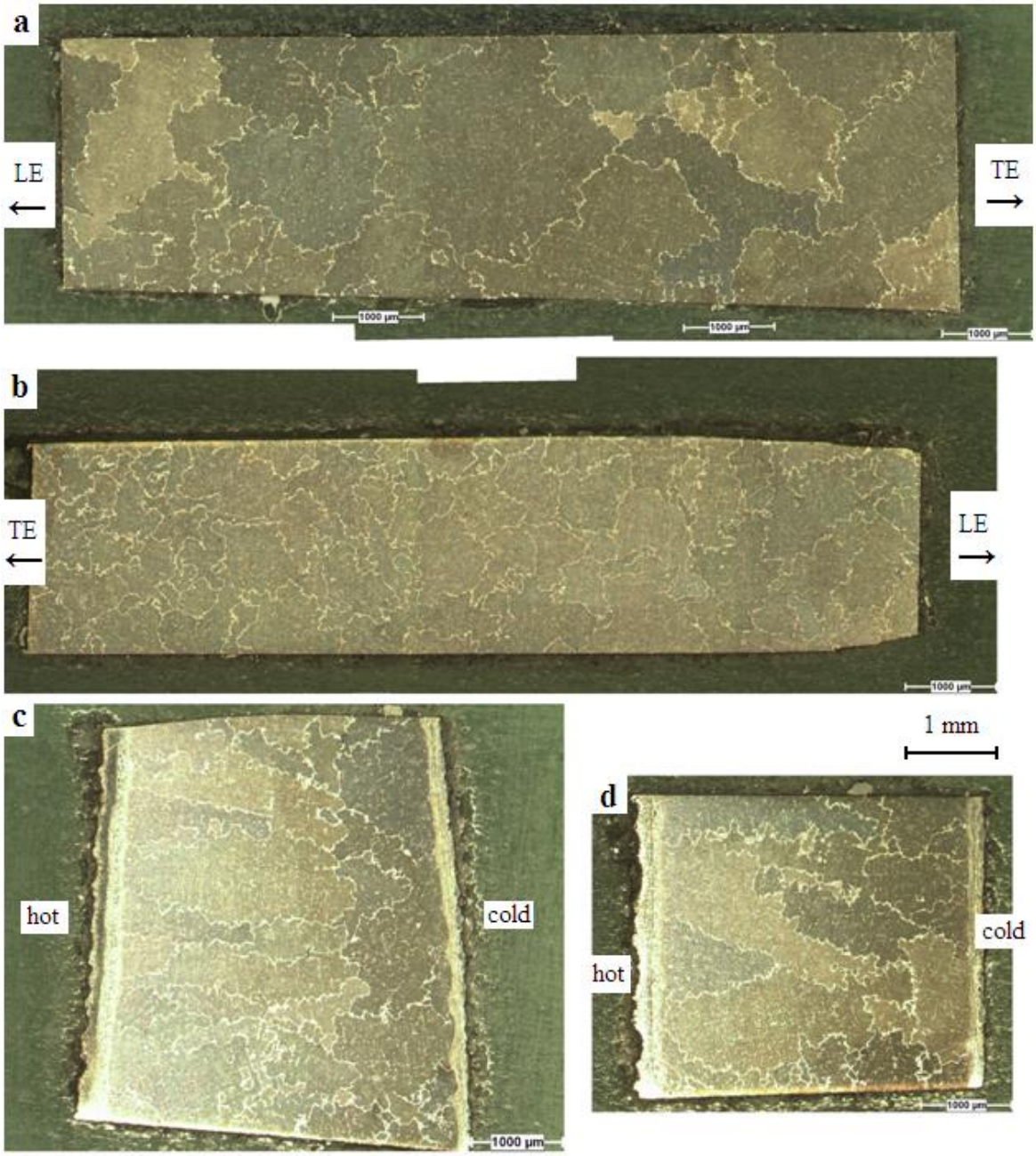

Figure 3.34. Grain morphology in PTM (Pressure side Tip section Middle position), a) cold surface, b) hot surface, c) z surface, and d) side surface specimens.

3.2.2.3. B80-SPO-TL (tip section leading edge). Figures 3.36, 3.37, and 3.38 respectively show the pressure side specimens, suction side specimens, and stagnation point specimens.

The cold and hot surface specimens of the pressure side have equiaxed grains. In z surface specimen of pressure side, there are elongated grains. TBC and bond layers are also visible in the Z surface. Due to overgrinding, a complete photo could not be obtained for the hot surface specimen.

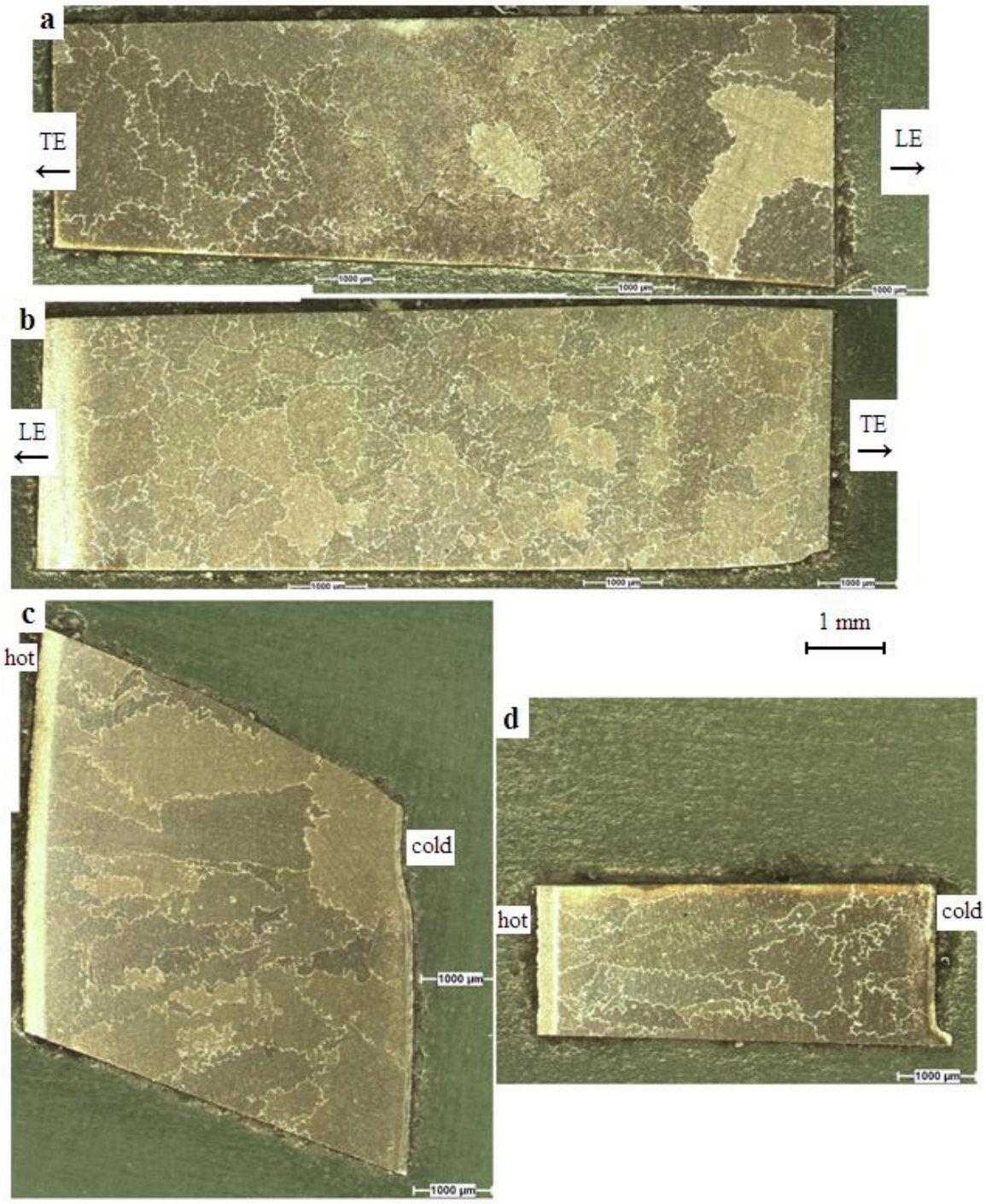

Figure 3.35. Grain morphology in STM (Suction side Tip section Middle position), a) cold surface, b) hot surface, c) z surface, and d) side surface specimens.

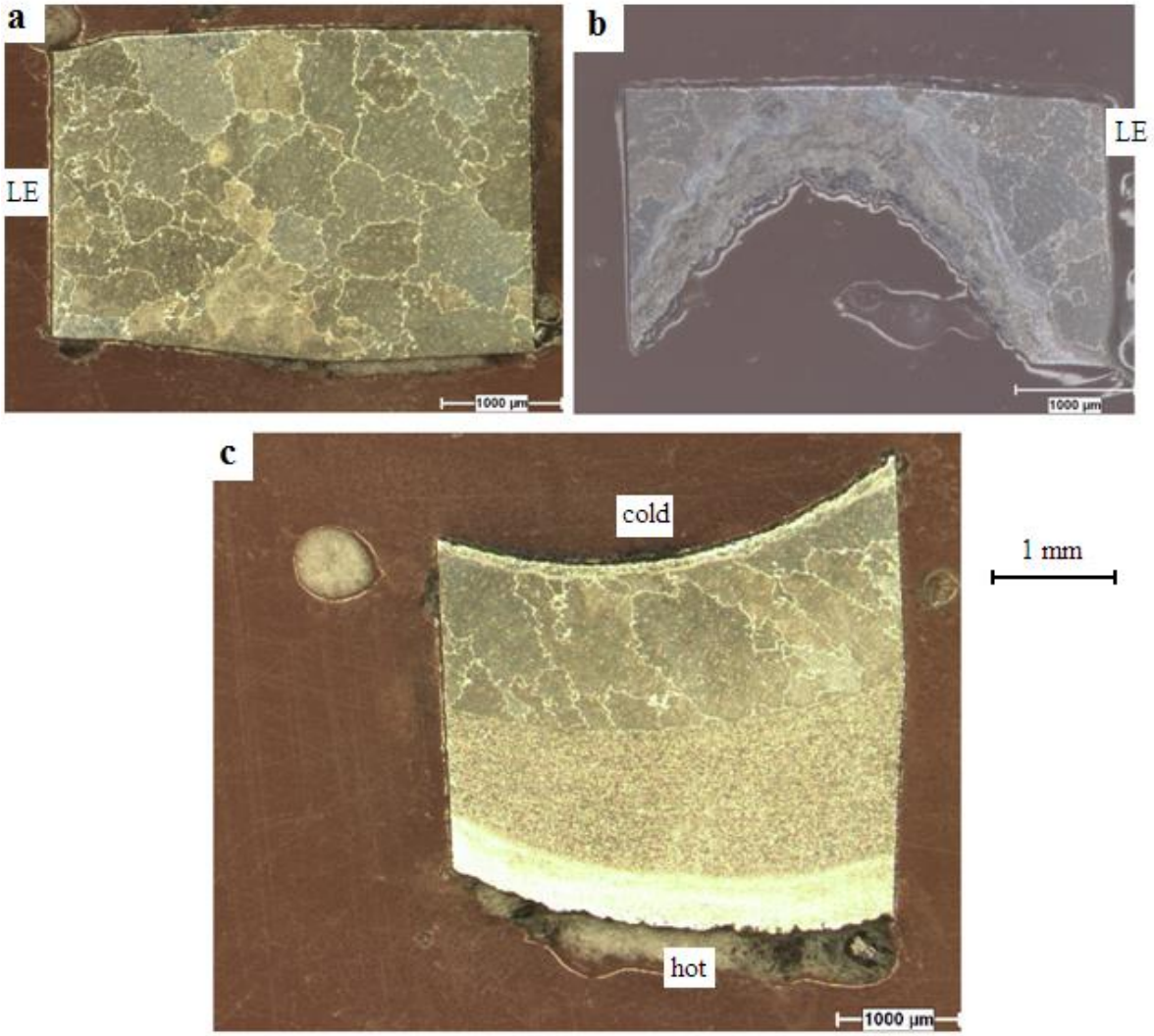

Figure 3.36. Grain morphology in PTL (Pressure side Tip section Leading edge), a) cold surface, b) hot surface, and c) z surface specimens.

There are equiaxed grains in the hot surface of the suction side. The cold surface specimen includes a few equiaxed grains. In the suction side, the z surface specimen has elongated grains toward hot surface, and equiaxed ones near the cold surface.

The cold, hot and z surface specimens of the stagnation point have all equiaxed grain morphology.

3.2.2.4. B80-SP-MT (middle section trailing edge). Photographs of the pressure side and suction side specimens are shown in Figure 3.39 and Figure 3.40, respectively.

In the pressure side, the hot surface specimen has finer grains than cold surface specimen; they both have the equiaxed grains. The z surface, the side surface far from the trailing edge, and the side surface close to the trailing edge specimens have equiaxed grains.

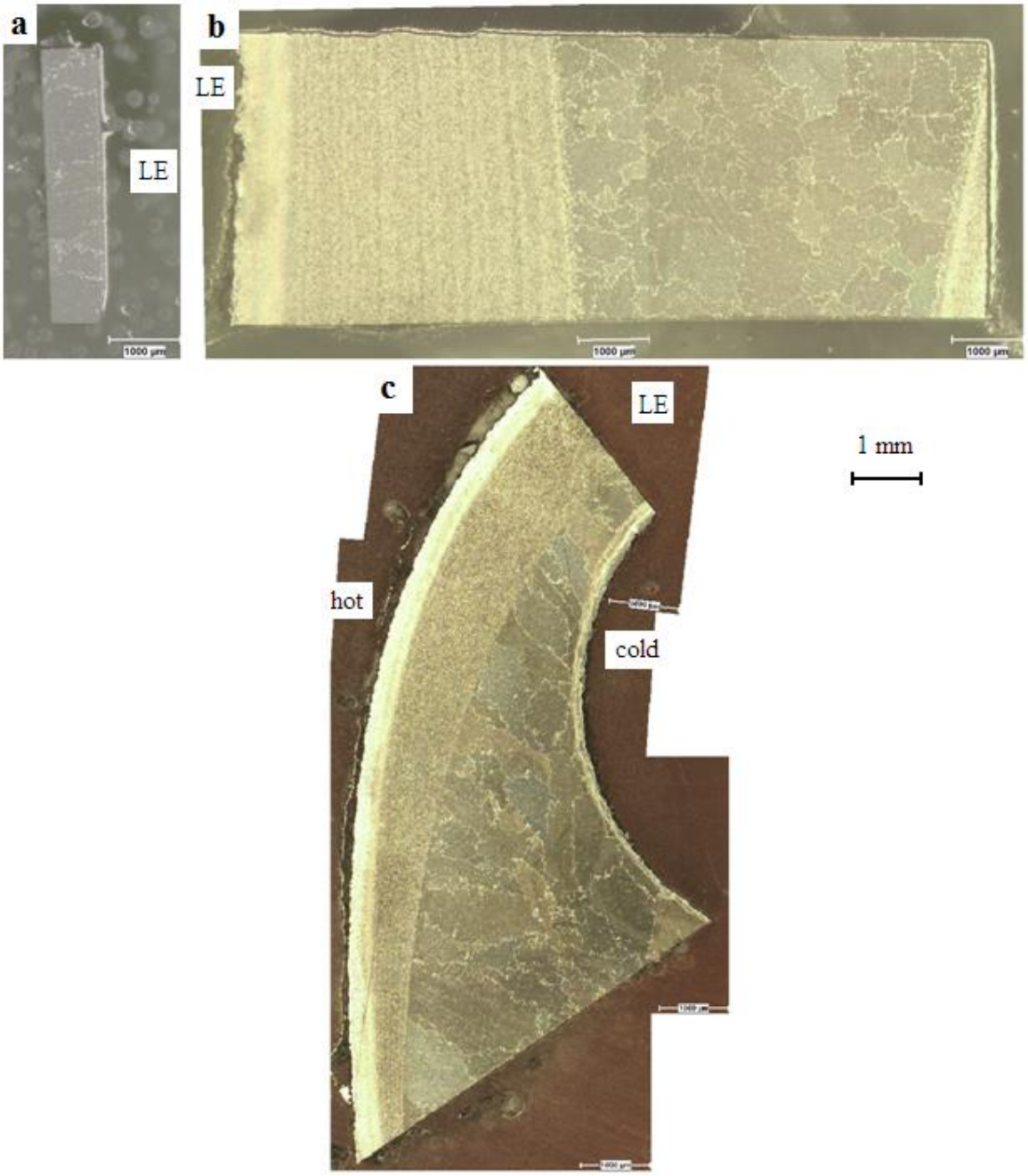

Figure 3.37. Grain morphology in STL (Suction side Tip section Leading edge), a) cold surface, b) hot surface, and c) z surface specimens.

In the suction side, the cold surface specimen has elongated and fine grains toward the trailing edge, the remaining part has equiaxed grains. The hot surface specimen has finer grains than the cold surface specimen, and the elongation is not observed in this specimen. In the z-surface specimen, there are both elongated and equiaxed grains. Side surface far from trailing edge and side surface close to trailing edge specimens have equiaxed grains. Side surface close to trailing edge specimen has finer grains than side surface far from trailing edge. Distance between these specimens is about 16 mm.

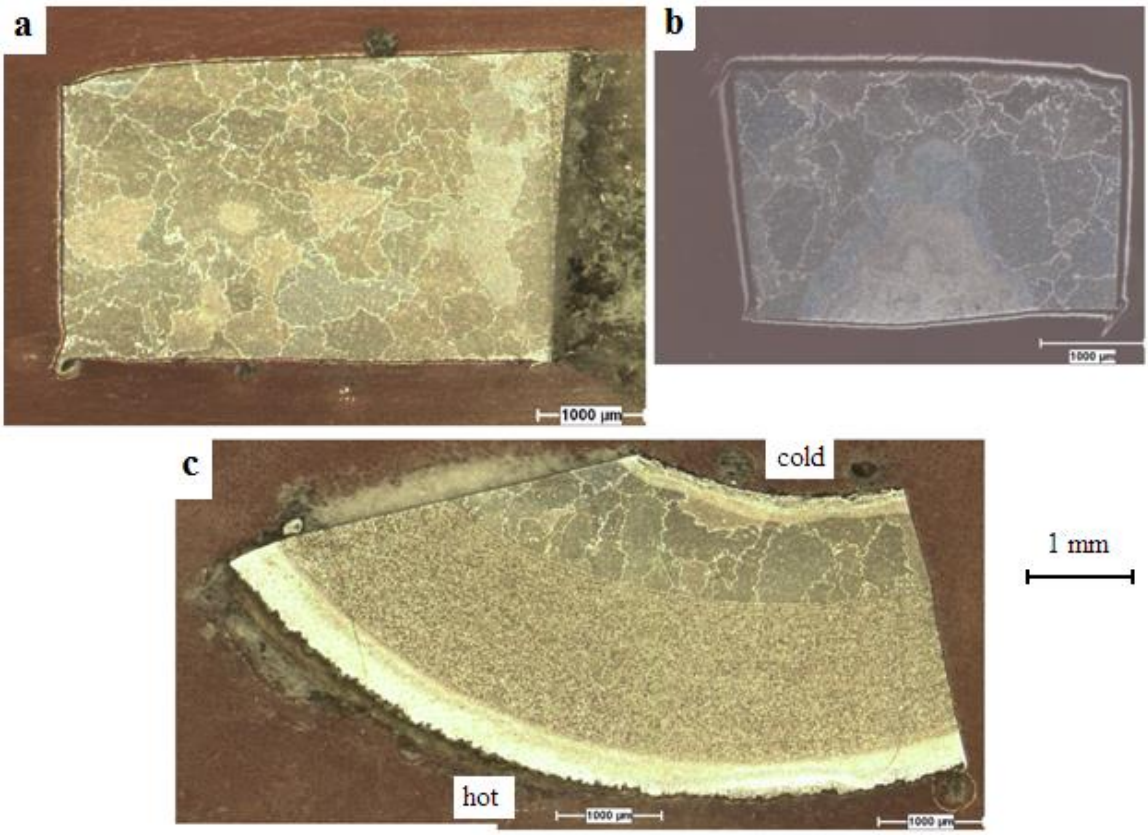

Figure 3.38. Grain morphology in OTL (stagnation point Tip section Leading edge), a) cold surface, b) hot surface, and c) z surface specimens.

3.2.2.5. B80-SP-MM (middle section middle position). In Figures 3.41 and 3.42, photographs of the pressure side specimens and suction side specimens are available, respectively.

In the pressure side, both the cold and hot surfaces have equiaxed grains, although the hot surface has finer ones. In the z-surface specimen, the hot surface has elongated

grains, but the cold surface has equiaxed grains. Side surface specimen has coarse elongated grains at the cold surface and fine equiaxed grains at the hot surface.

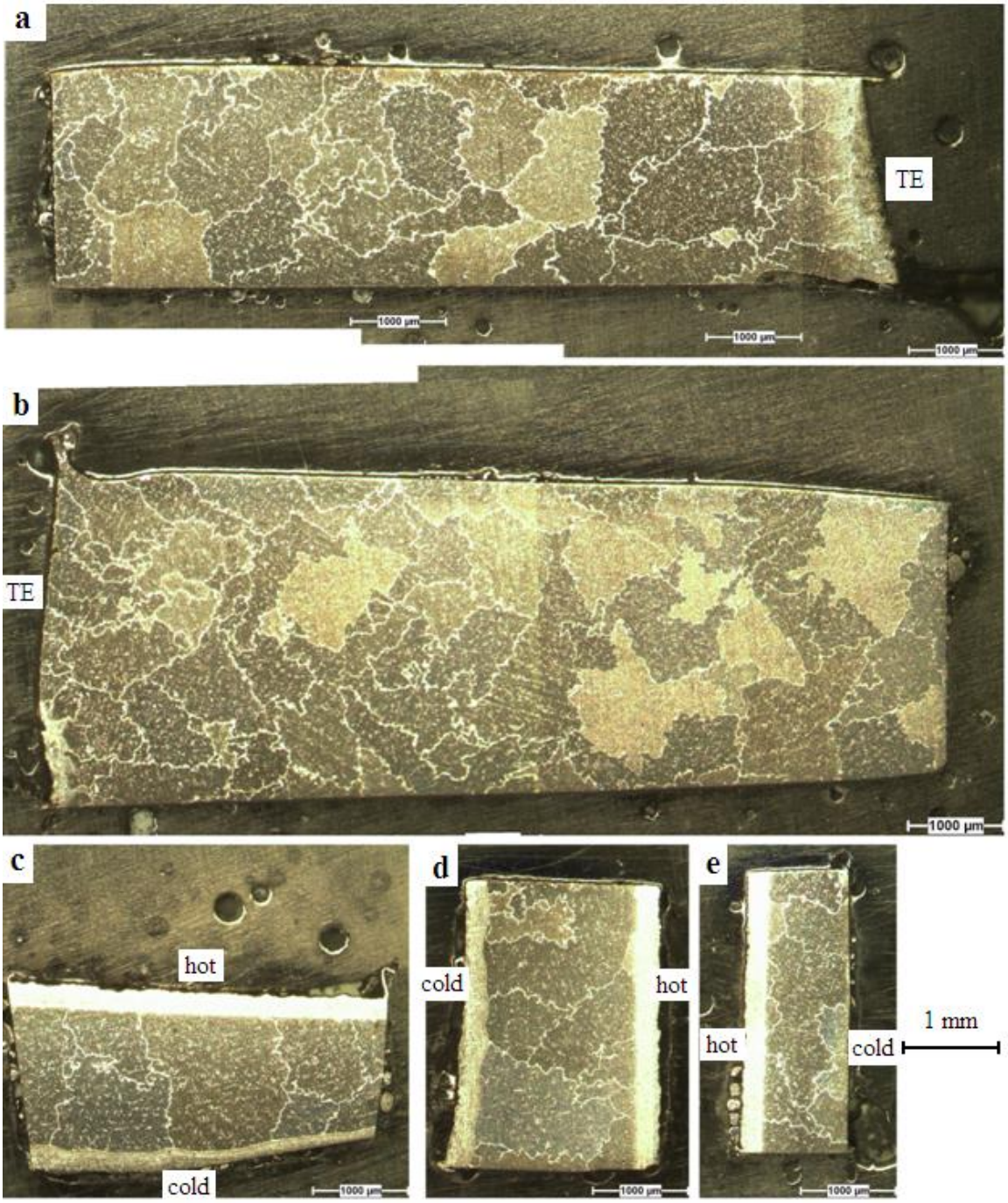

Figure 3.39. Grain morphology in PMT (Pressure side Middle section Trailing edge), a) cold surface, b) hot surface, c) z surface, d) side surface far from trailing edge, and e) side surface close to trailing edge specimens.

In the suction side, the cold surface specimen has coarse equiaxed grains, and grains in the left part are finer than the rest of the specimen. Grains in the hot surface specimen are equiaxed and finer than those in the cold surface specimen grains. The z-surface specimen has elongated grains starting from the hot surface and extending almost to the cold surface. However, the cold surface has equiaxed grains. In the side surface specimen, grains are elongated at the hot surface, but they are coarse and equiaxed at the cold surface.

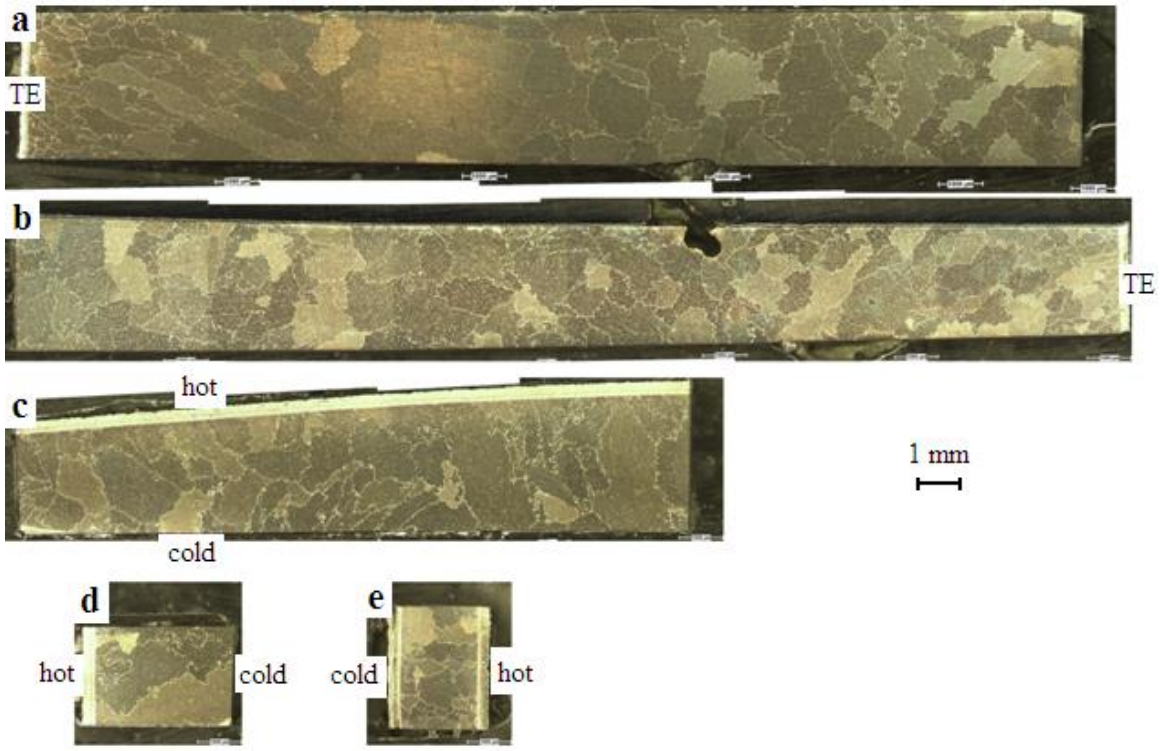

Figure 3.40. Grain morphology in SMT (Suction side Middle section Trailing edge), a) cold surface, b) hot surface, c) z surface, d) side surface far from trailing edge, and e) side surface close to trailing edge specimens.

3.2.2.6. B80-SPO-ML (middle section leading edge). The pressure side, suction side, and stagnation point specimens are given in Figures 3.43, 3.44 and 3.45, respectively.

In the pressure side, equiaxed and elongated grains are available together in all specimens. Grains are coarse at the cold surface and fine at the hot surface in the z surface specimen.

The hot surface specimen of the suction side has equiaxed grains. There are a few equiaxed grains in the cold surface specimen. The z-surface specimen has elongated grains close to the stagnation point. Grains at the hot surface are equiaxed.

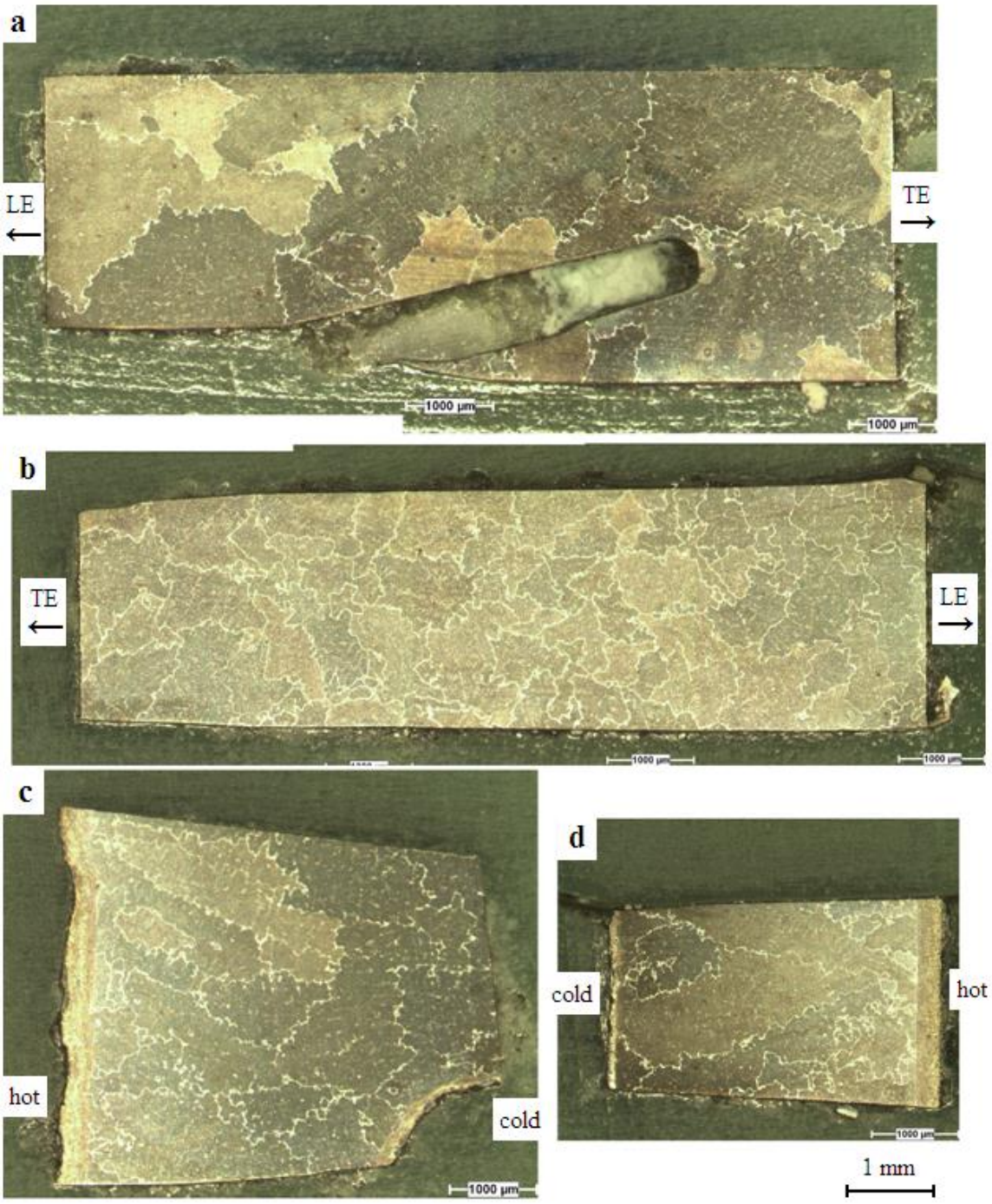

Figure 3.41. Grain morphology in PMM (Pressure side Middle section Middle position), a) cold surface, b) hot surface, c) z surface, and d) side surface specimens.

The cold, hot, and z surface specimens of stagnation point have all equiaxed grains.

3.2.2.7. B80-SP-RT (root section trailing edge). Photographs of the pressure side and suction side specimens are respectively shown in Figures 3.46 and 3.47.

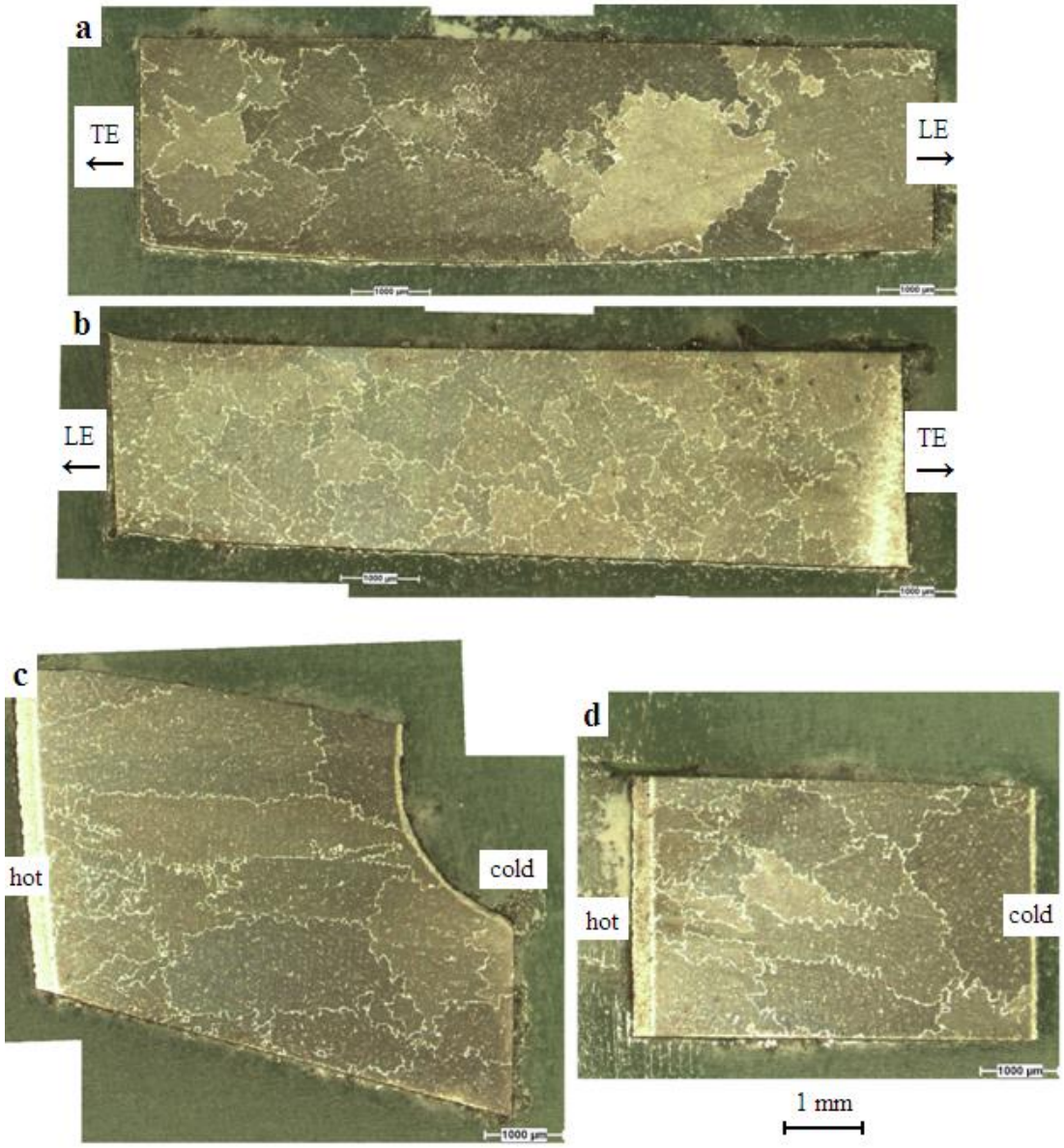

Figure 3.42. Grain morphology in SMM (Suction side Middle section Middle position), a) cold surface, b) hot surface, c) z surface, and d) side surface specimens.

In the pressure side, the cold and hot surface specimens have equiaxed grains, and the hot surface has finer grains than the cold surface specimen. In the z surface specimen, there are both equiaxed and elongated grains. The side surface far from the trailing edge

specimen has elongated grains, and the side surface close to the trailing edge specimen has equiaxed grains.

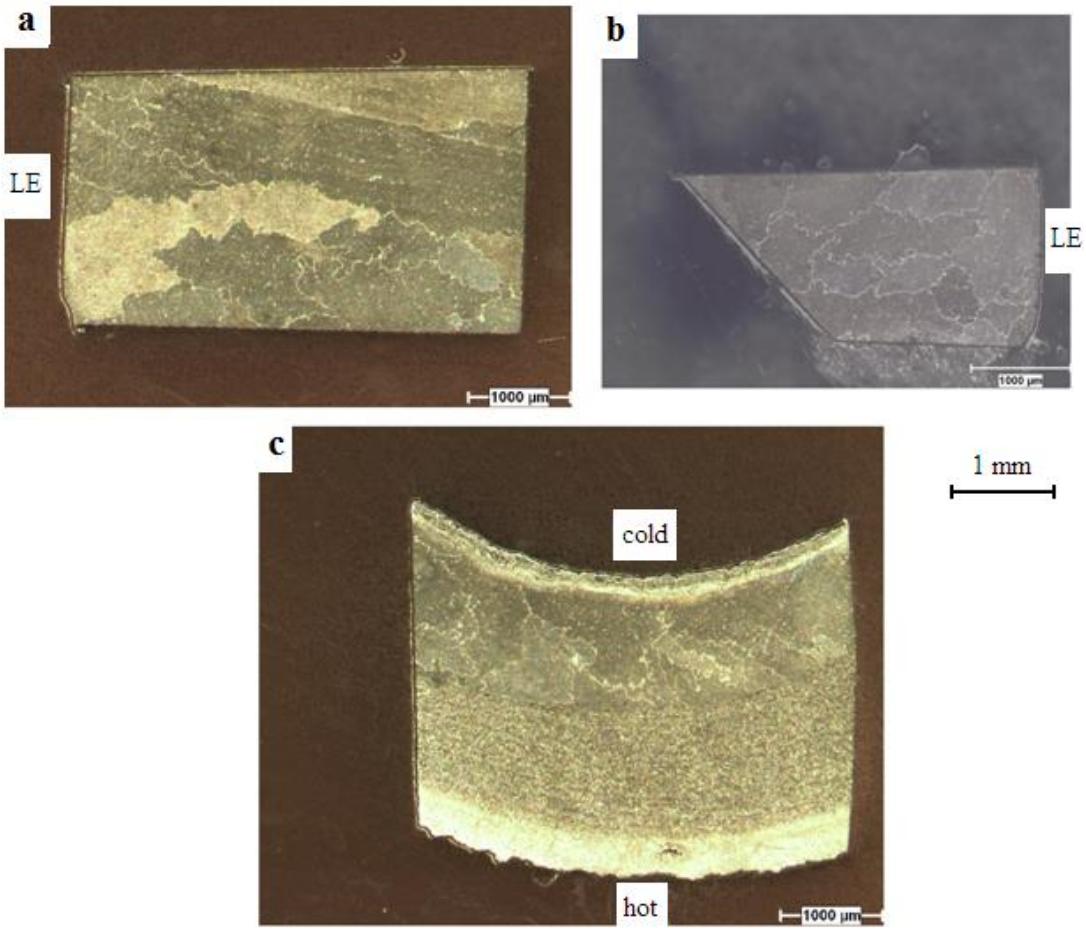

Figure 3.43. Grain morphology in PML (Pressure side Middle section Leading edge), a) cold surface, b) hot surface, and c) z surface specimens.

In the suction side, the cold and hot surface specimens have elongated grains at the trailing edge. In both, remaining parts are composed of equiaxed grains. The hot surface specimen has finer grains than the cold surface specimen. In the z surface specimen, there are both elongated and equiaxed grains. The side surface far from the trailing edge has elongated grains and side surface close to the trailing edge specimen has equiaxed grains. Distance between these two side surface specimens is about 15 mm.

3.2.2.8. B80-SP-RM (root section middle position). In Figure 3.48 and Figure 3.49, photographs of the pressure side specimens and suction side specimens are given, respectively.

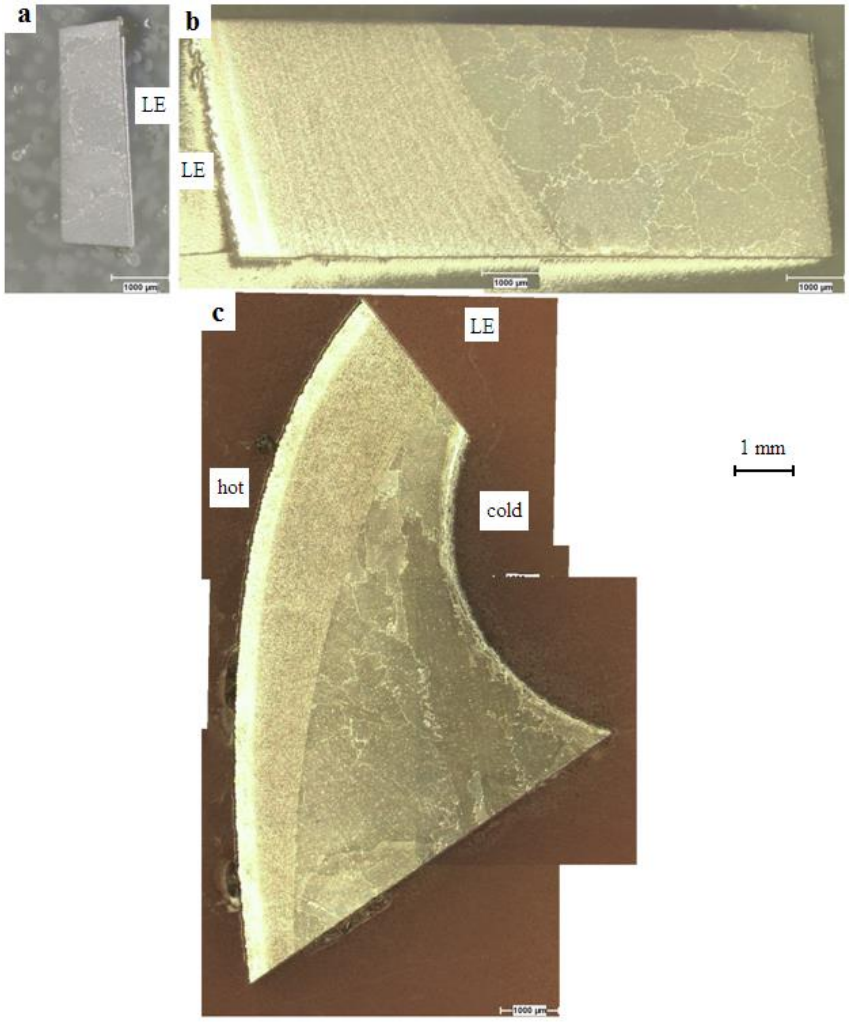

Figure 3.44. Grain morphology in SML (Suction side Middle section Leading edge), a) cold surface, b) hot surface, and c) z surface specimens.

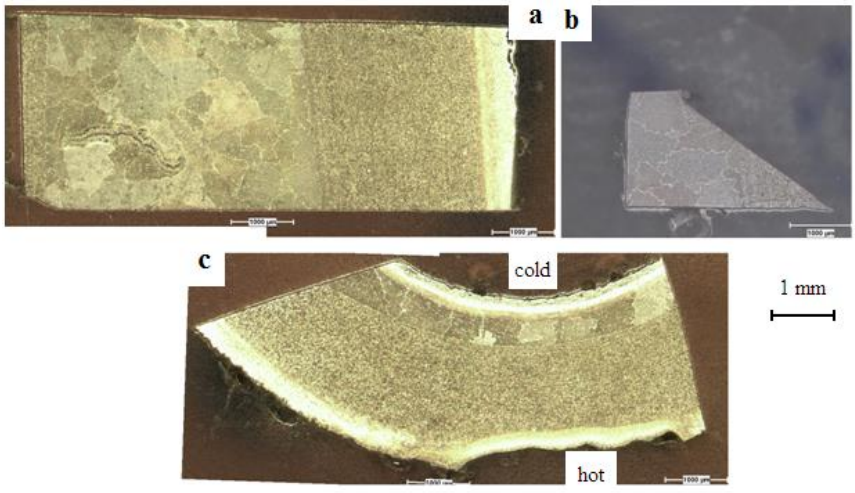

Figure 3.45. Grain morphology in OML (stagnation point Middle section Leading edge), a) cold surface, b) hot surface, and c) z surface specimens.

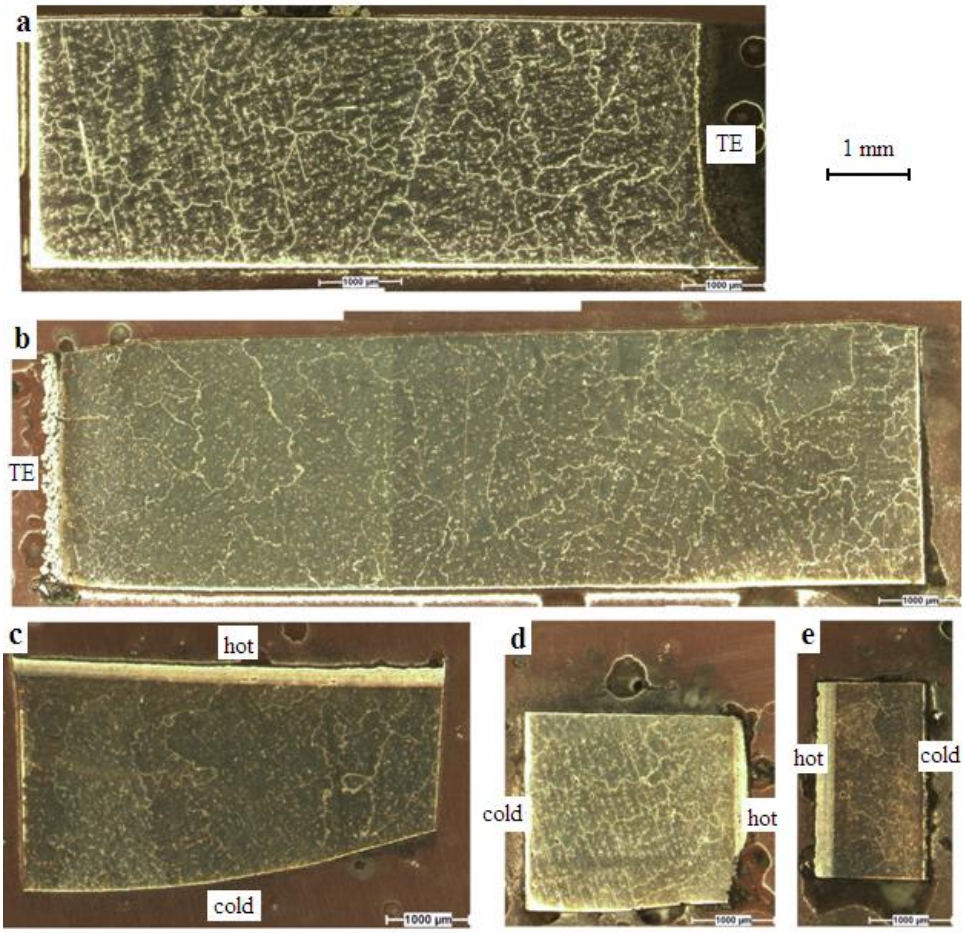

Figure 3.46. Grain morphology in PRT (Pressure side Root section Trailing edge), a) cold surface, b) hot surface, c) z surface, d) side surface far from trailing edge, and e) side surface close to trailing edge specimens.

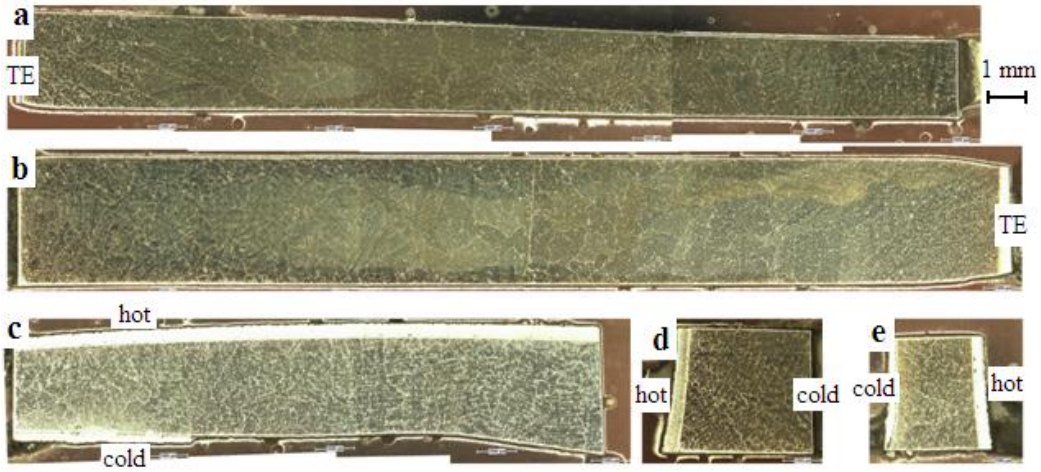

Figure 3.47. Grain morphology in SRT (Suction side Root section Trailing edge), a) cold surface, b) hot surface, c) z surface, d) side surface far from trailing edge, and e) side surface close to trailing edge specimens.

In the pressure side, grains are equiaxed in both the hot and cold surface specimens, and grains are coarser in the cold surface specimen. In the z surface specimen, grains are elongated and extending from hot surface to cold surface. Grains are coarser at the cold side. In the side surface specimen, there is a very coarse grain at the cold surface. Grains at the hot surface are equiaxed and fine.

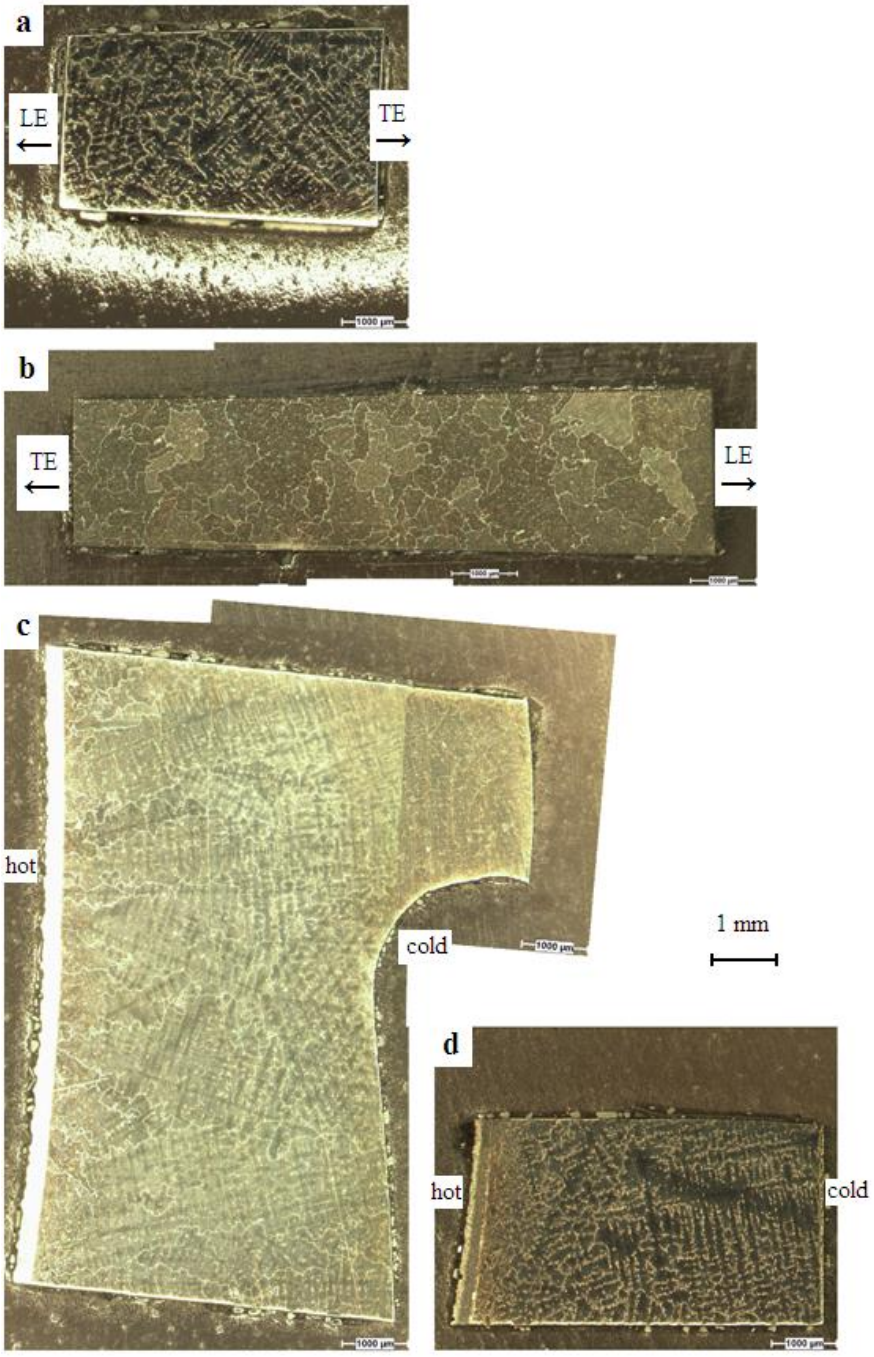

Figure 3.48. Grain morphology in PRM (Pressure side Root section Middle position), a) cold surface, b) hot surface, c) z surface, and d) side surface specimens.

In the suction side, the hot surface has finer grains than the cold surface; the both have equiaxed grains. The z surface specimen has elongated grains. The side surface specimen has equiaxed grains.

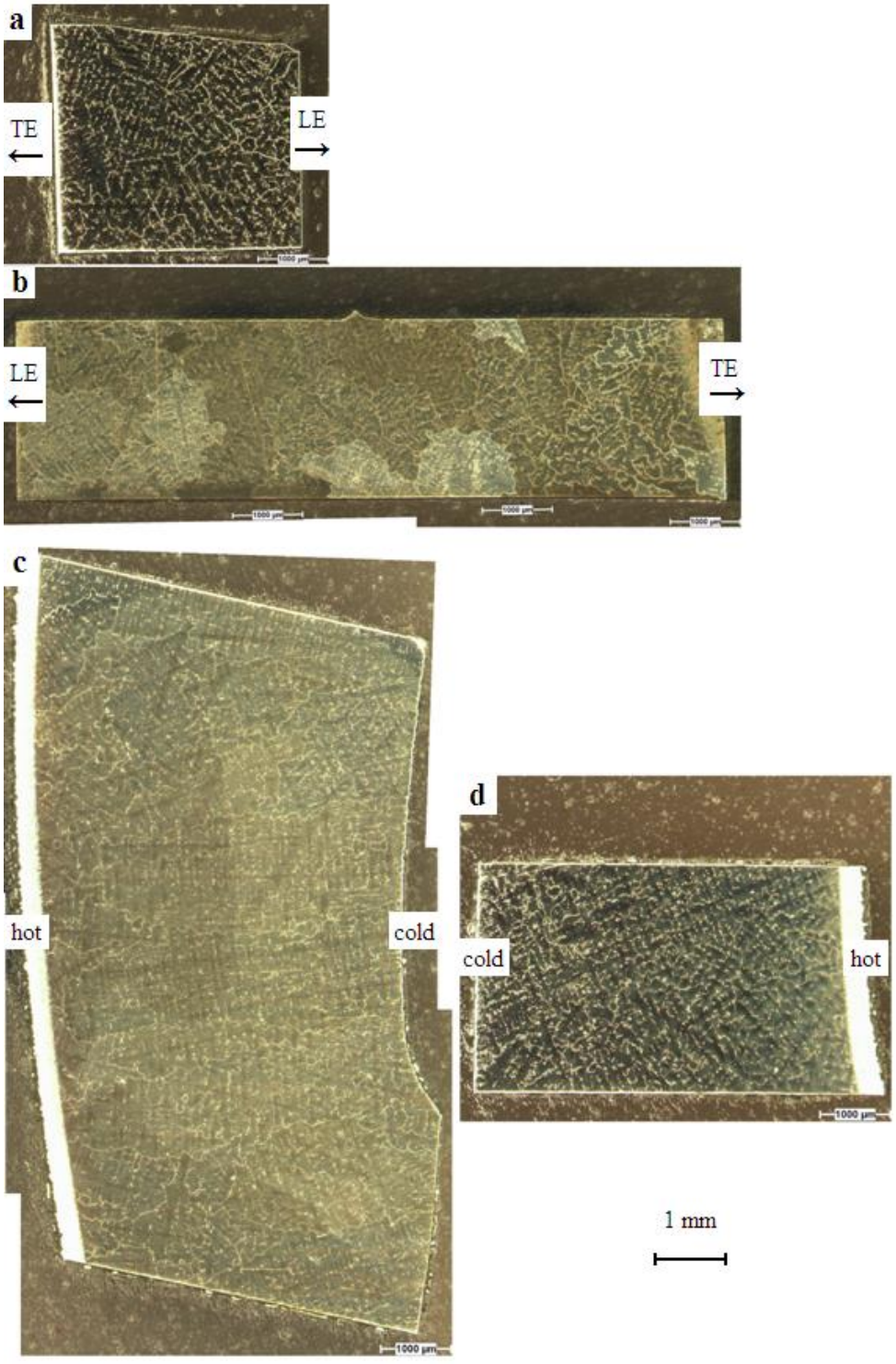

Figure 3.49. Grain morphology in SRM (Suction side Root section Middle position), a) cold surface, b) hot surface, c) z surface, and d) side surface specimens.

3.2.2.9. B80-SPO-RL (root section leading edge). The pressure side, suction side and stagnation point specimens are respectively available in Figures 3.50, 3.51 and 3.52.

In the pressure side, the cold and hot surface specimens have equiaxed grains. The z surface specimen has elongated grains extending from the cold to hot.

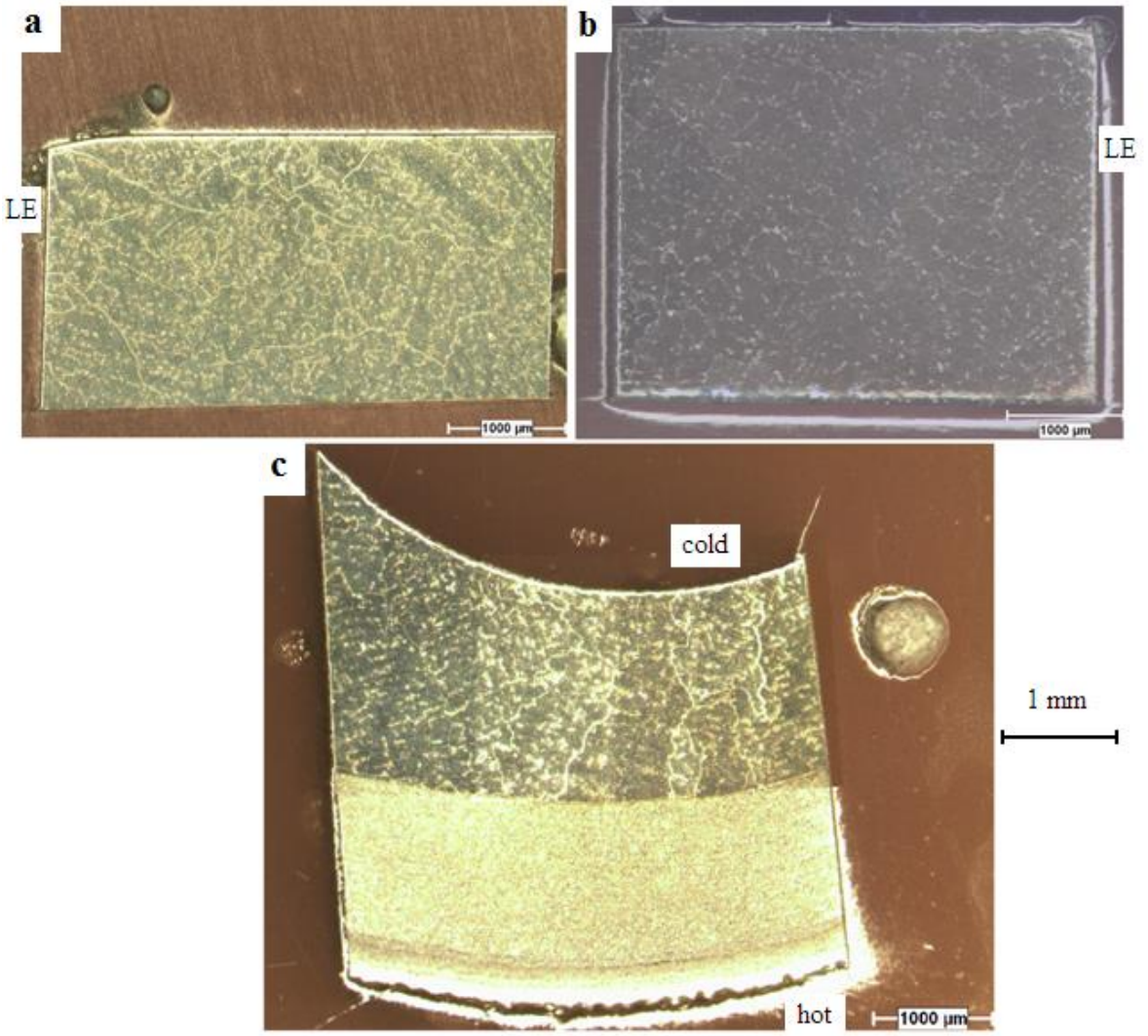

Figure 3.50. Grain morphology in PRL (Pressure side Root section Leading edge), a) cold surface, b) hot surface, and c) z surface specimens.

In the suction side, the hot and cold surface specimens have equiaxed grains. The z surface specimen has equiaxed coarse grains. Cold, hot, and z surface specimens of stagnation point have all equiaxed grains.

3.2.2.10. Firtree Specimen. Figure 3.53 gives the grain morphology in the firtree specimen. Grains of this specimen are equiaxed. Firtree section is assumed to be affected the least from the temperature and stress, so it may be representing the as cast microstructure in the blade. This specimen is at the very bottom of the turbine blade, as it can be seen in Figure 2.2.

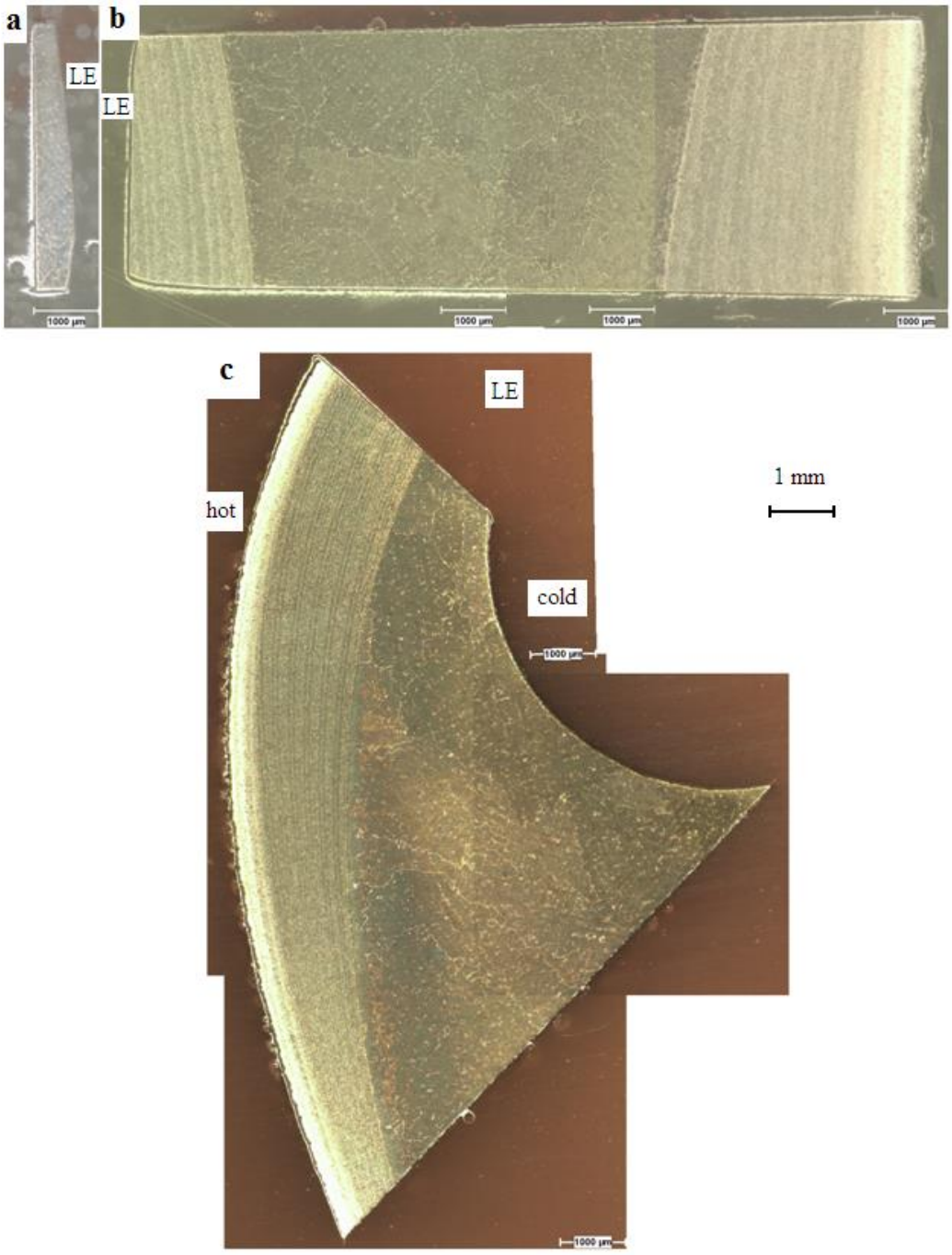

Figure 3.51. Grain morphology in SRL (Suction side Root section Leading edge), a) cold surface, b) hot surface, and c) z surface specimens.

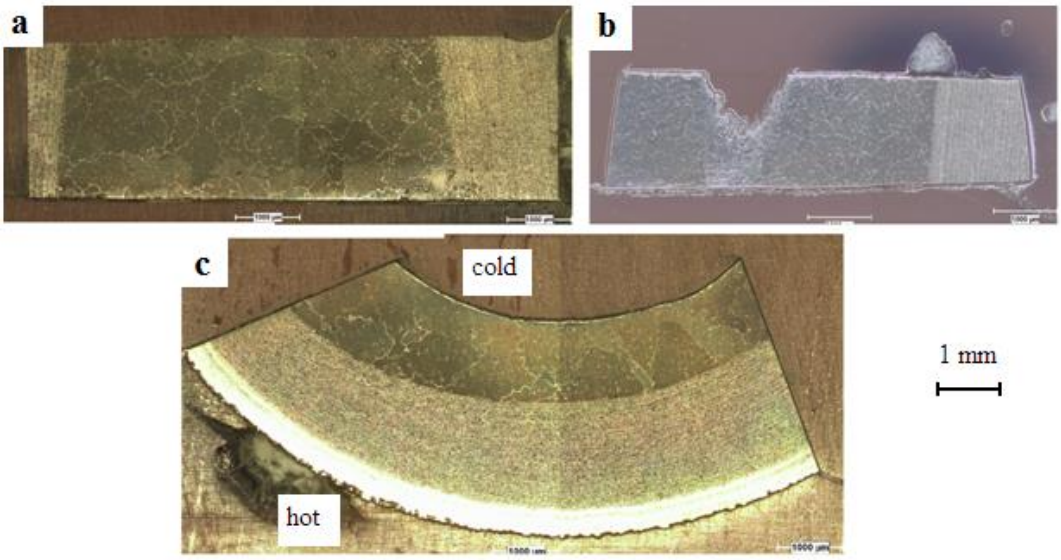

Figure 3.52. Grain morphology in ORL (stagnation point Root section Leading edge), a) cold surface, b) hot surface, and c) z surface specimens.

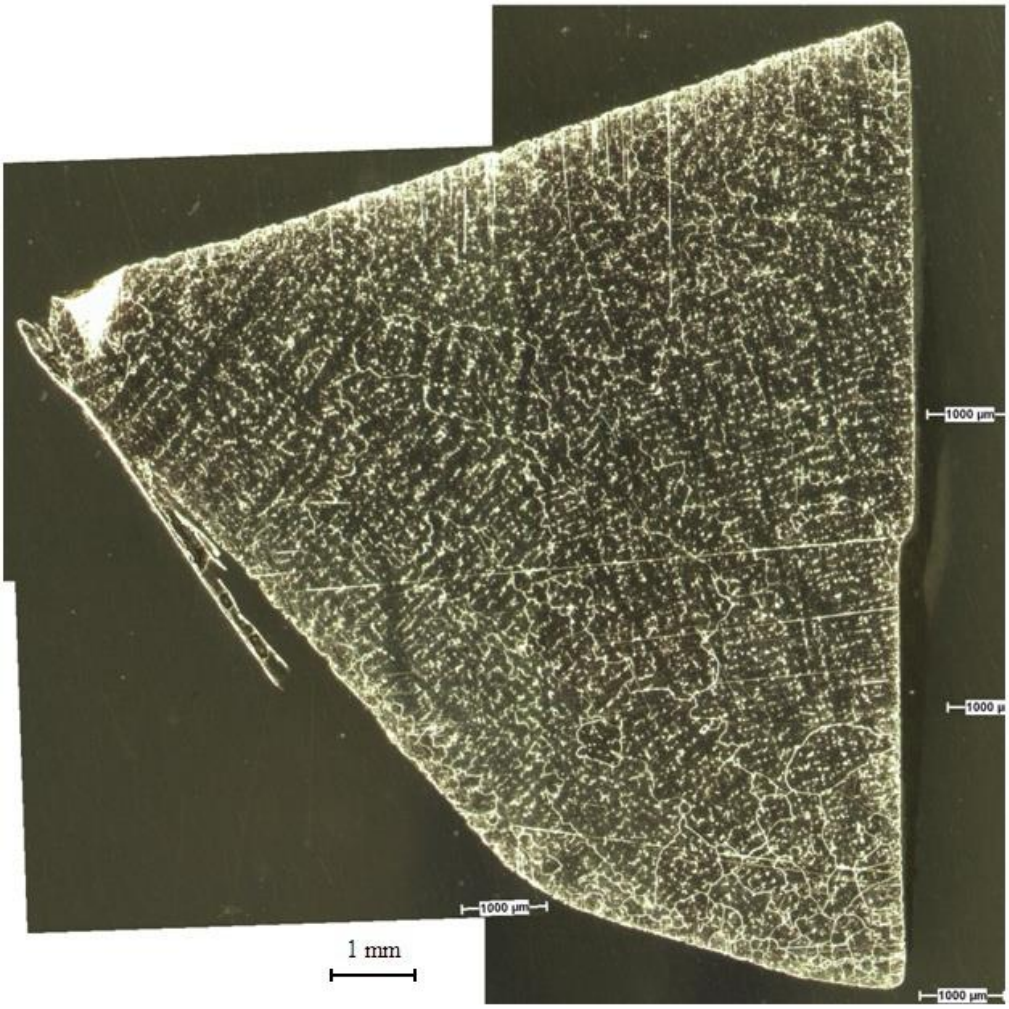

Figure 3.53. Grain morphology in firtree specimen.

3.3. Precipitate Size and Morphology

3.3.1. Precipitate Size

The average precipitate size was determined from the SEM photos using the Image J image processing software. Scanning electron microscope photographs in the hot surfaces and cold surfaces with 15000, 30000, and 60000 magnification were used to determine the precipitate size. The area of each individual precipitate is calculated. Then, with a spherical equivalent shape assumption, the precipitate diameter was calculated for all precipitates in a photograph. Finally, an average precipitate diameter was calculated by averaging diameters of all precipitates in that photograph. The average precipitate diameter at predetermined blade locations can be seen in Table 3.5. Cold surface precipitates are finer than hot surface precipitates except for one position.

Table 3.5. Average precipitate diameter (nm) vs. position.

Side →		Pressure				Suction		
Positions → / Sections ↓		Trailing edge	Middle	Leading edge	Stagnation	Leading edge	Middle	Trailing edge
Tip	Hot	482	620	364	332	393	406	470
	Cold	483	308	289	329	253	281	292
Middle	Hot	431	539	484	464	416	494	299
	Cold	325	316	400	463	273	290	246
Root	Hot	154	155	187	176	235	195	189
	Cold	105	142	141	107	98	131	135
Firtree		179						
Virgin		244						

Figure 3.54 shows the precipitate size for the trailing edge position along the blade span, namely the tip, middle, and root sections. In the pressure side of the tip section, the precipitate size for the cold surface is slightly greater than the precipitate size for the hot surface. It should be noted that this point is the only exception where the cold surface precipitates are coarser than the hot surface precipitates throughout the blade. The hot

surface precipitates are coarser than the cold surface precipitates in the middle, root and suction side of tip section. In the both hot and cold surfaces, precipitate size decreases while going from the tip section to root section.

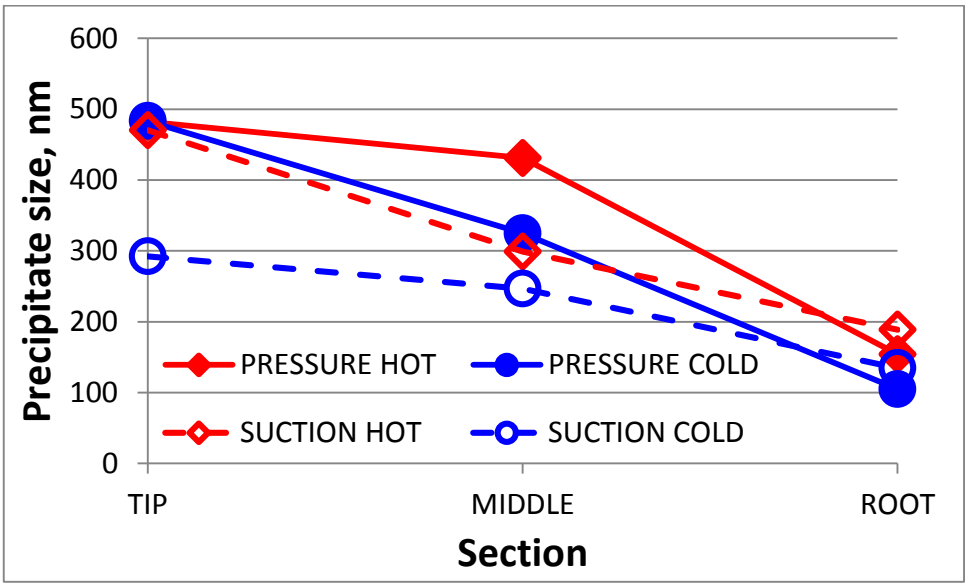

Figure 3.54. Precipitate size for the trailing edge position.

The precipitate size for the middle position is given in Figure 3.55. The cold surface precipitates are finer than the hot surface precipitates in both the pressure and suction sides. The precipitate size in the hot surface decreases while moving from tip section to root section in the pressure side; however, the precipitate size in the hot surface is largest at the middle section and smallest at the root section in the suction side. Precipitate size values for cold surface specimens in the tip and middle sections are almost equal and root section precipitates are finer for both the pressure and suction sides. Difference between the precipitate size values of hot and cold surfaces in root section is less than that in the tip and middle sections. In all sections, cold surface precipitates of suction side are slightly finer than cold surface precipitates of pressure side.

The precipitate size for the leading edge position is shown in Figure 3.56. The hot surface precipitates are coarser than the cold surface precipitates in the pressure side, suction side, and stagnation point. For both the hot and cold surfaces, precipitate size is the greatest at the middle section and the smallest at the root section. For both the hot and cold surfaces in the suction side, the precipitate size values in the tip section and middle section

are close, although the middle section precipitates are slightly coarser than the tip section precipitates. In stagnation point, the hot surface precipitate size and cold surface precipitate size values are very close in the tip and middle sections, although the hot surface precipitates are slightly coarser than the cold surface precipitates. However, in the root section stagnation point, the hot surface has larger precipitates.

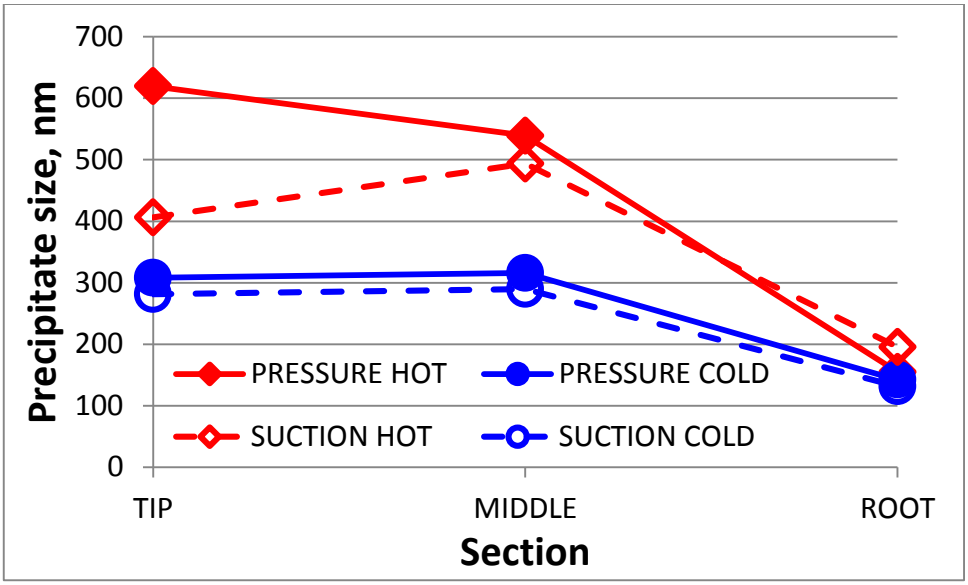

Figure 3.55. Precipitate size for the middle position.

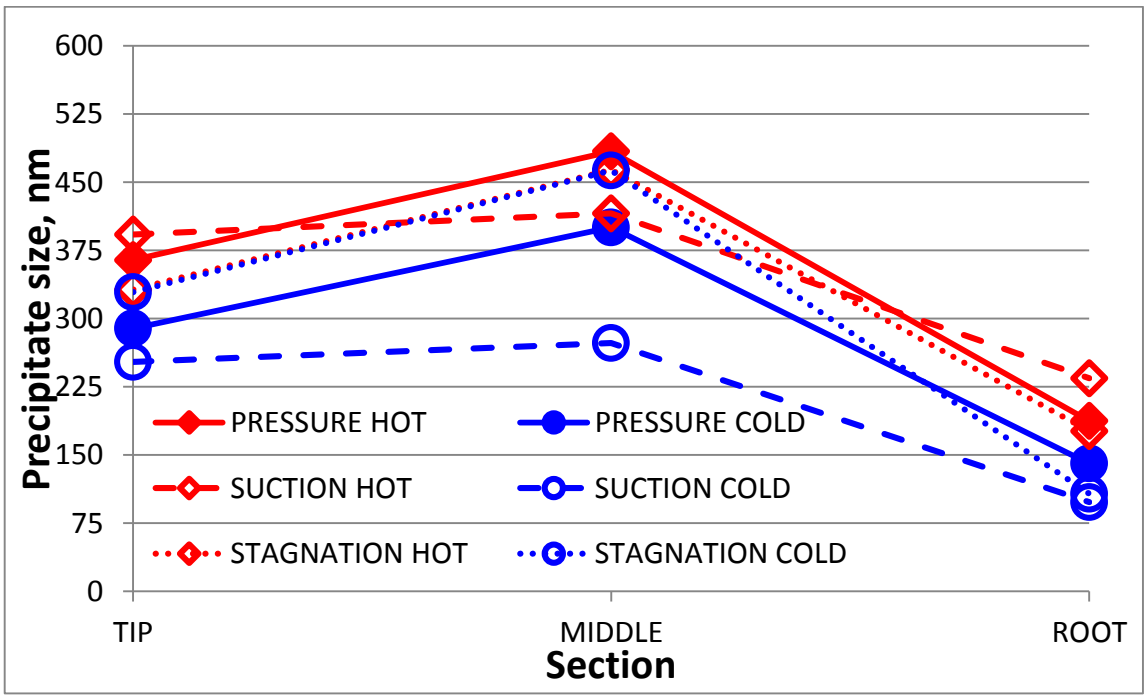

Figure 3.56. Precipitate size for the leading edge position.

Figure 3.57 shows the precipitate size for the tip section specimens. The hot surface precipitates are coarser than the cold surface precipitates, except for the trailing edge position of the pressure side. For the hot surface, the precipitate size is the largest at the pressure side middle position. For cold surface, pressure side trailing edge specimen has the largest precipitate size. At the stagnation point and the pressure side trailing edge positions, the precipitate size for the hot and cold surfaces is very close.

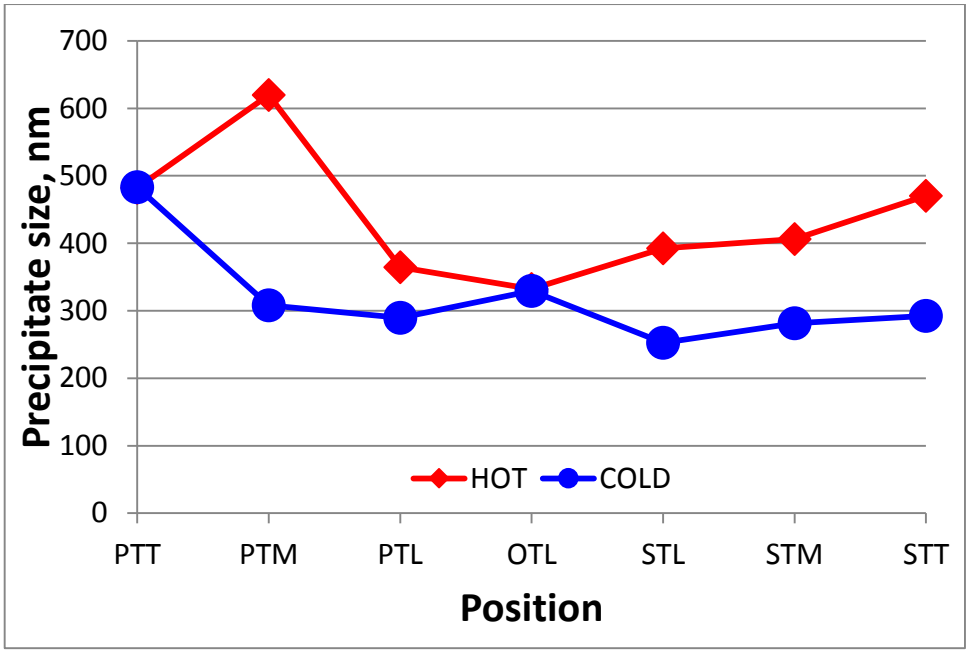

Figure 3.57. Precipitate size for specimens in the tip section.

The precipitate size for middle section specimens is given in Figure 3.58. Cold surface specimens have finer precipitates than hot surface specimens. Pressure side middle position specimen has the largest average precipitate size in hot surface. Stagnation point specimen has the largest average precipitate size in the cold surface. Hot surface and cold surface precipitates have almost equal size in stagnation point. In both pressure and suction sides of hot surface, middle position precipitate size is the largest and trailing edge precipitate size is the smallest.

Precipitate size for specimens in root section is shown in Figure 3.59. Cold surface specimens have finer precipitates than the hot surface specimens. In root section, precipitates are finer than tip section and middle section for both hot surface and cold surface. Hot surface precipitates are coarser than cold surface precipitates. Also, precipitate

size in the firtree specimen is 179 nm. This value is greater than cold surface values and close to hot surface values. Also, the precipitate size was analyzed on a virgin blade. The size was determined as 244 nm. This value is greater than all of the precipitate size values in the root section.

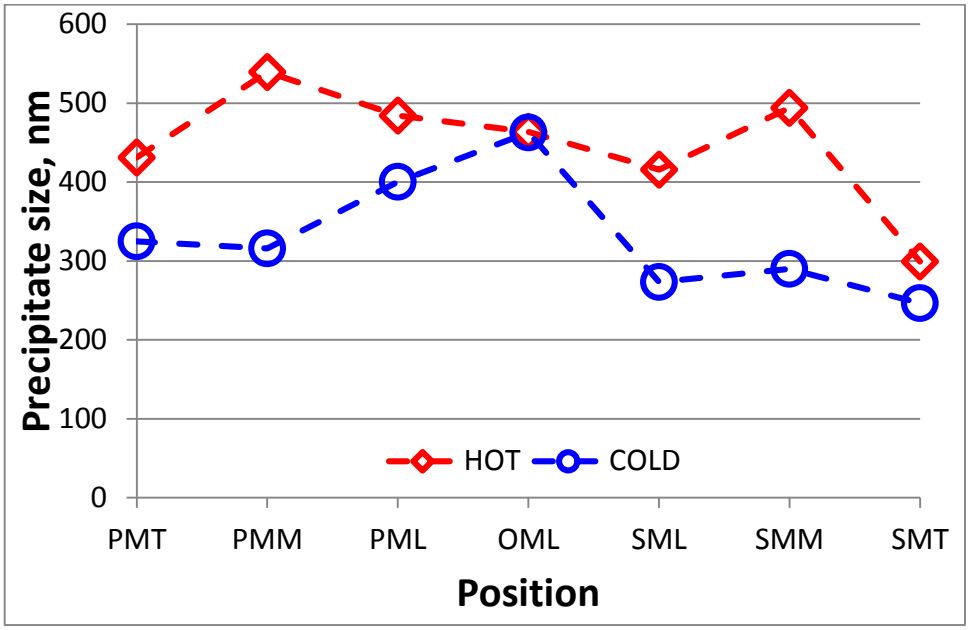

Figure 3.58. Precipitate size for specimens in the middle section.

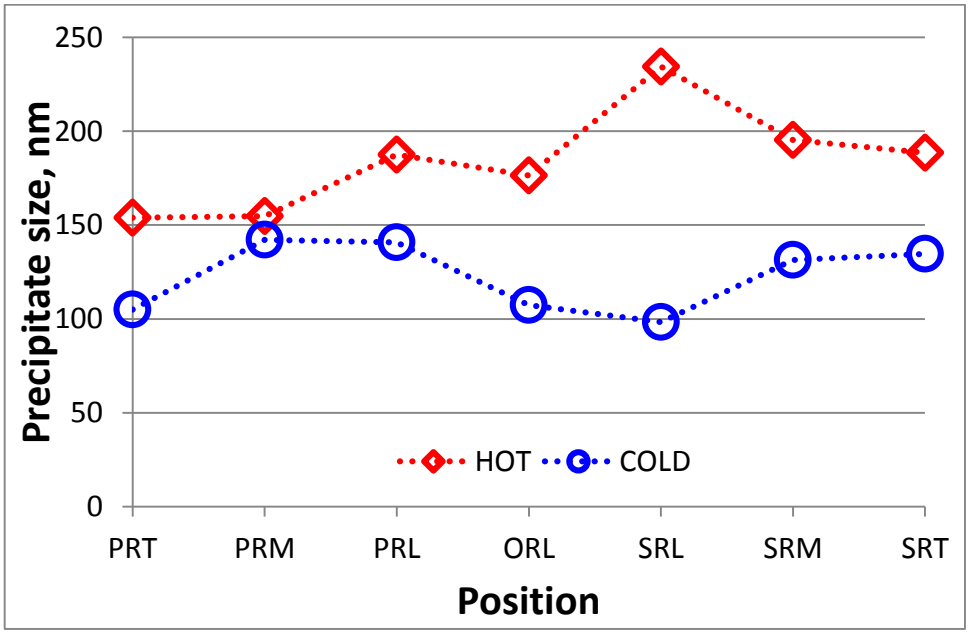

Figure 3.59. Precipitate size for specimens in the root section.

Data given in Figures 3.57, 3.58, and 3.59 are collected in Figure 3.60.

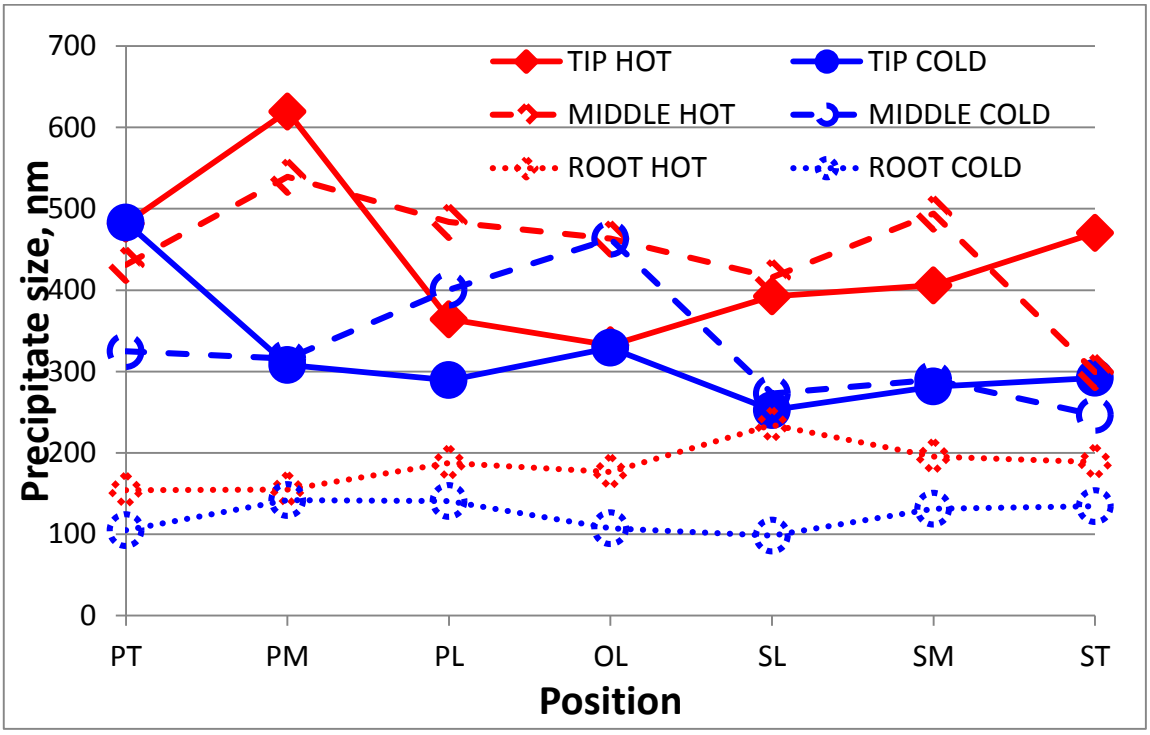

Figure 3.60. Precipitate size for specimens in the tip, middle, and root sections.

3.3.2. Precipitate Morphology

The precipitate microstructures of the tip section, middle section, and root section are respectively given in Figure 3.61, Figure 3.62, and Figure 3.63.

In the tip section, cold surface precipitates are cubic except for the trailing edge. Other specimens have sphere like precipitates in which corners of the cubes are lost.

In the middle section, the cold surface specimens of the leading edge have lost their cubic shape and become sphere. Cubic shape remains in other cold surface specimens in this section. In the leading edge, hot surface specimens of the pressure side and suction side show raft formation. Other hot surface precipitates have spherical shape.

In the root section, precipitates are almost cubic. Formation of very fine precipitates was observed in the cold surface specimens of this section except for pressure side middle position and stagnation point specimens. However, in these two positions, formation of very fine precipitates can be seen in z surface specimen photographs close to the cold surface. It is understood that the very fine precipitates could not be seen on the cold surface

due to overgrinding in these two positions. Formation of the very fine precipitates is not observed in the hot surface specimens except for both the suction and pressure sides of the trailing edge. In z surface specimen photograph of these two positions, the pressure side does not show the very fine precipitates, but the suction side does. Number of the very fine precipitates at these locations is less than that in the cold surface specimens.

In the tip section, the raft formation was observed in both the hot and cold surfaces and both the pressure and suction sides of the trailing edge, hot surfaces of both the pressure and suction sides of the middle position; and the hot surfaces of the suction side and the stagnation point of the leading edge.

Among four photographs, two of them have cubic precipitates with no raft, one of them have new formed rafts, and one have full rafts in the suction side tip section middle position hot surface specimen. Photo of this position in Figure 3.61 is given as full rafts.

Raft formation was not observed among three of four photographs in the suction side tip section trailing edge position hot surface specimen. The other photo has rafts and is used in Figure 3.61.

In the middle section, the raft formation was observed in the hot surfaces of both the pressure and suction sides of the middle position, and both the hot and cold surfaces of the pressure and suction sides and the stagnation point of the leading edge.

Raft formation was not observed in the root section.

As stated before, in the root section, a very fine precipitate formation occurs. This formation is especially observed in cold surface specimens. This formation is illustrated in Figure 3.64. Also, it can be seen that some coarser precipitates come together and try to merge.

It was mentioned that suction side root section trailing edge hot surface specimen included very fine precipitates. Figure 3.65 gives Z surface specimen photograph of this position.

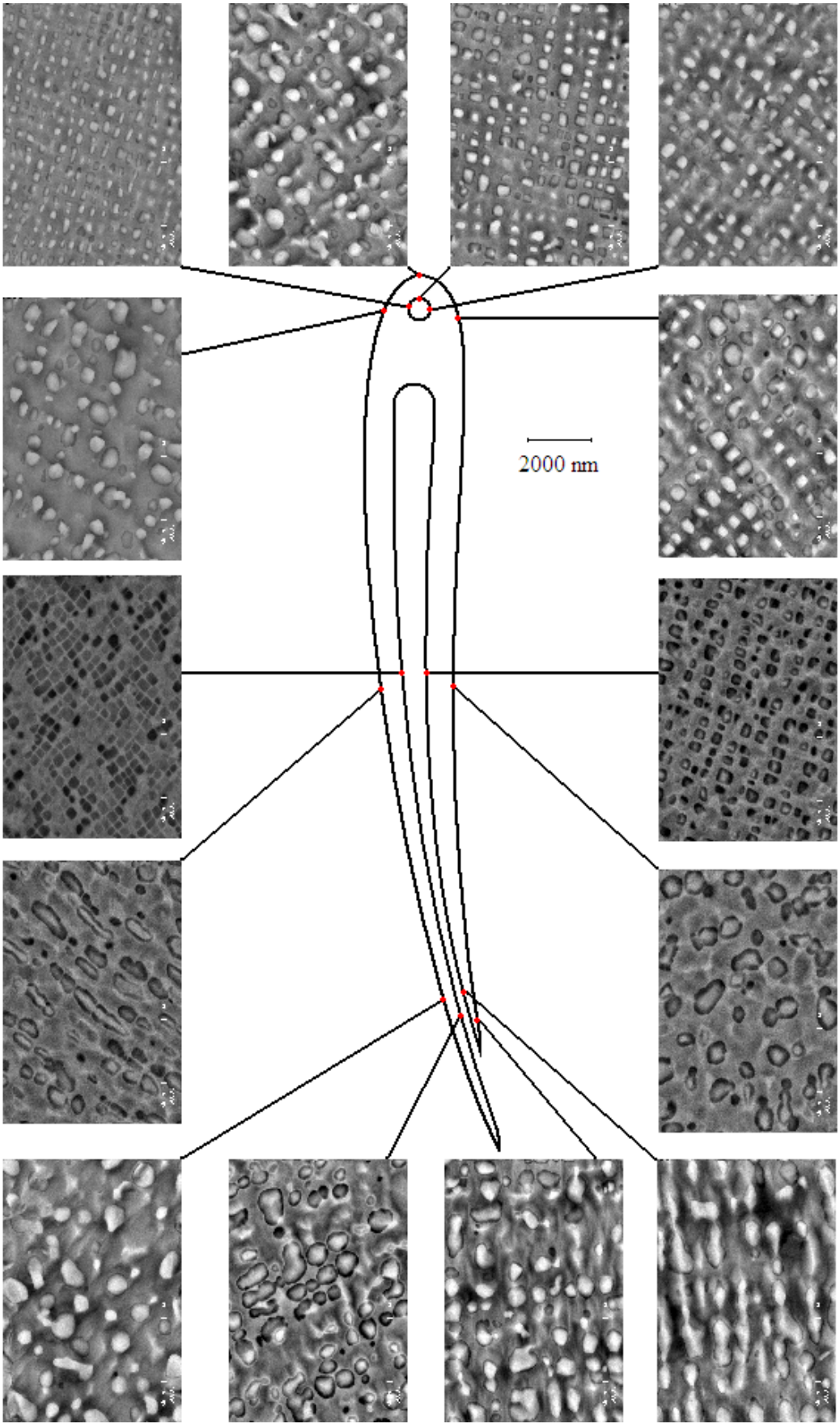

Figure 3.61. Precipitate microstructure in the tip section specimens.

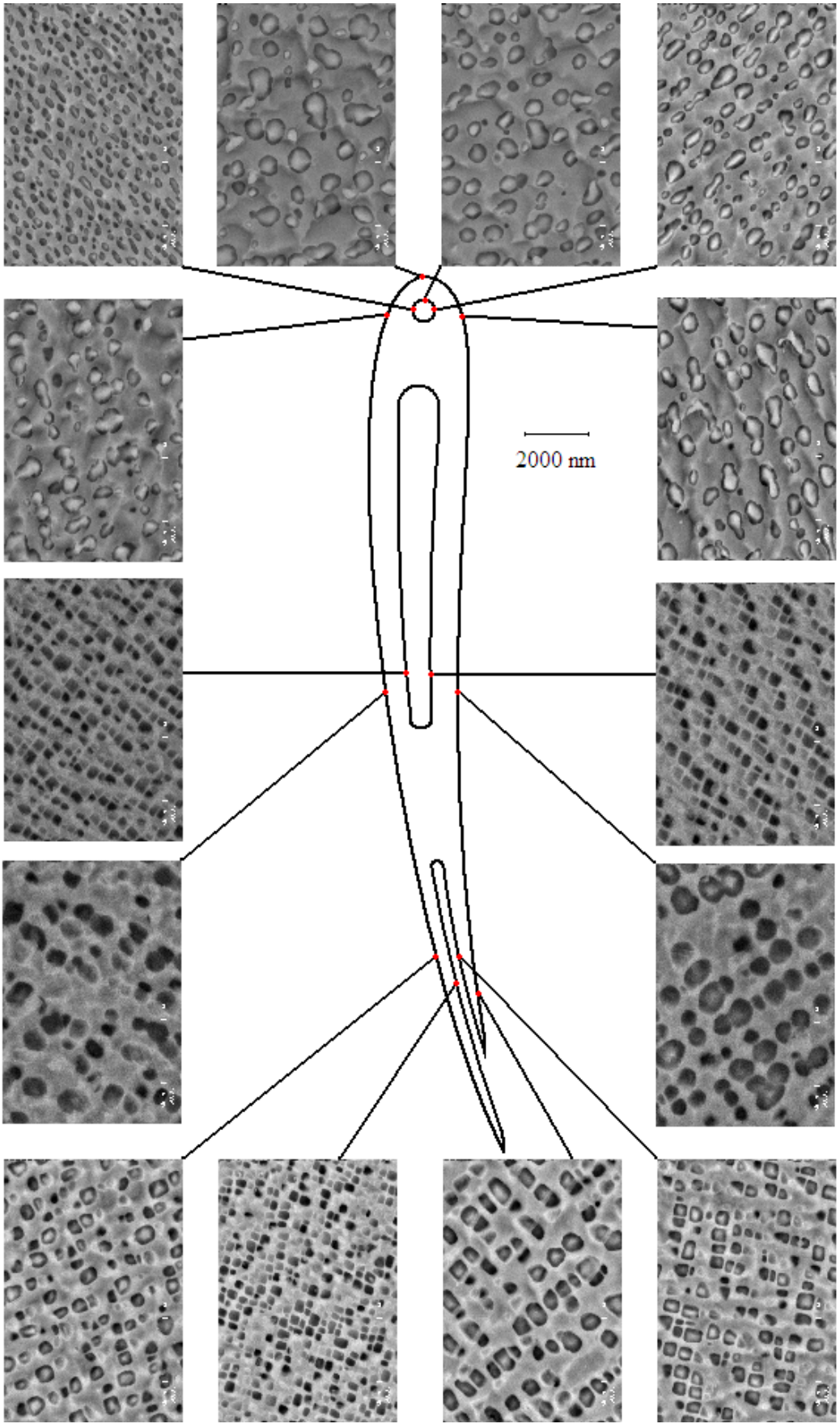

Figure 3.62. Precipitate microstructure in the middle section specimens.

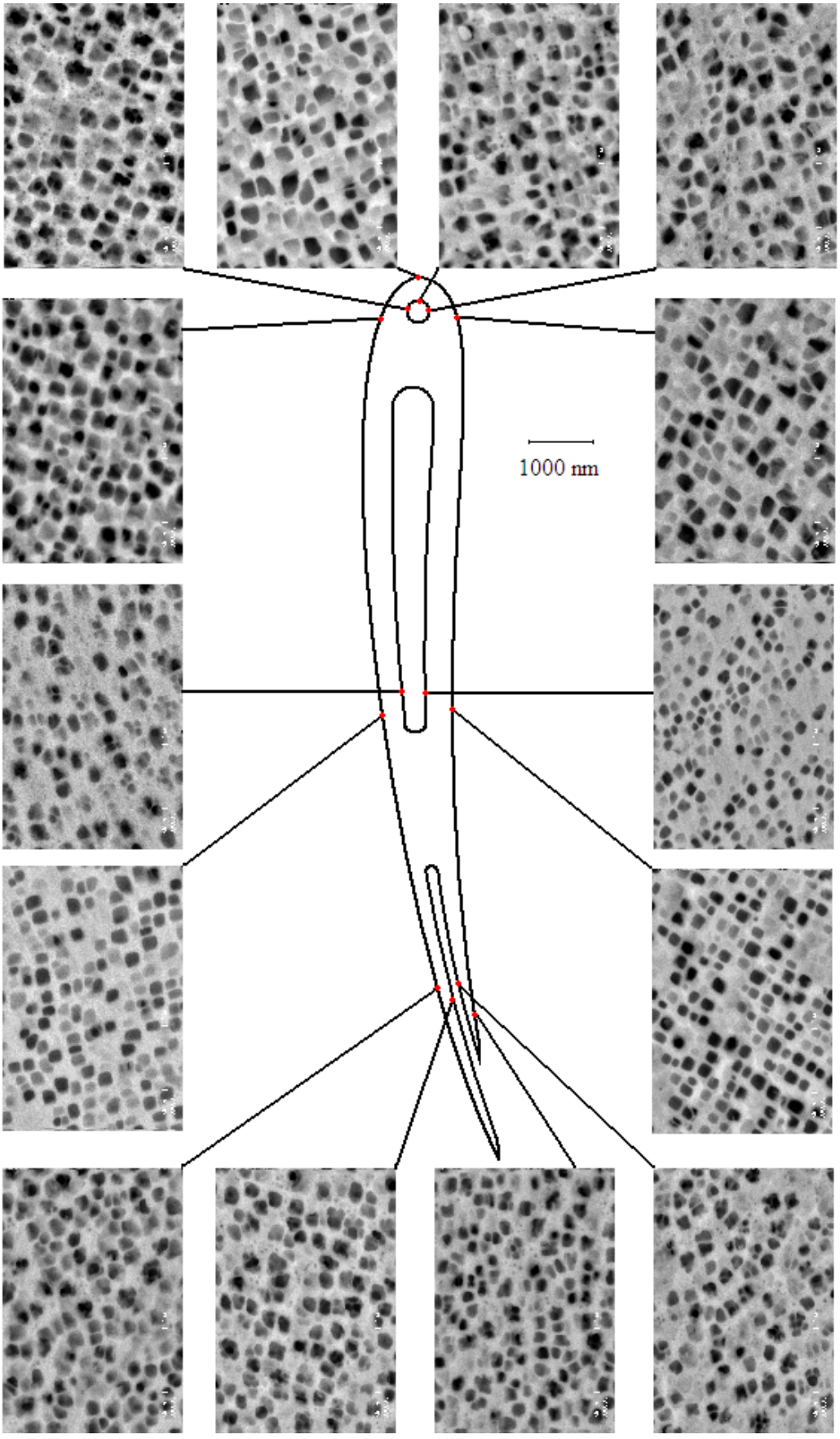

Figure 3.63. Precipitate microstructure in the root section specimens.

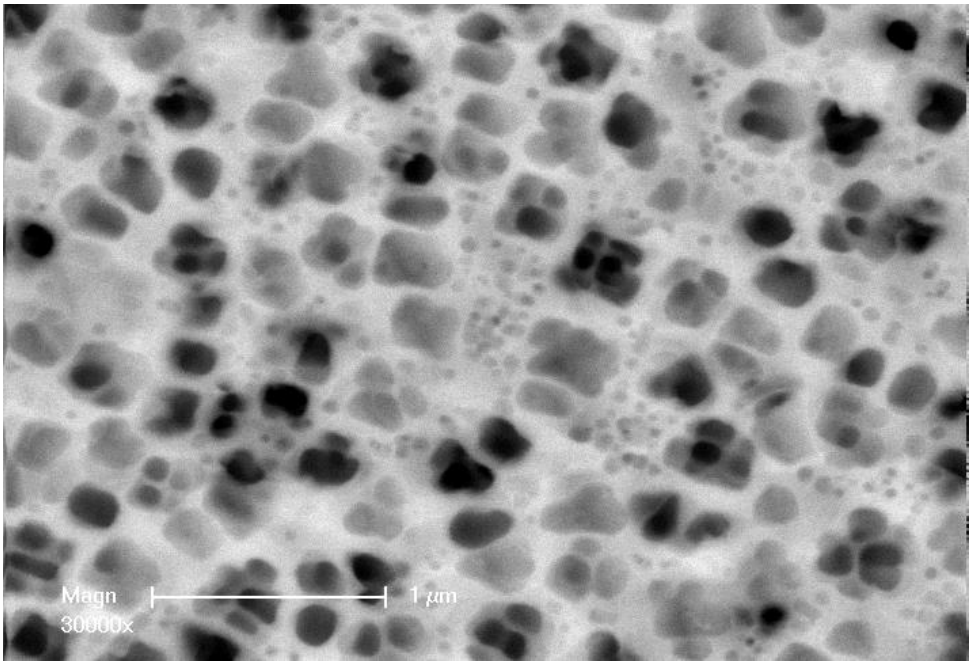

Figure 3.64. Formation of very fine precipitates in suction side, root section, trailing edge, cold surface.

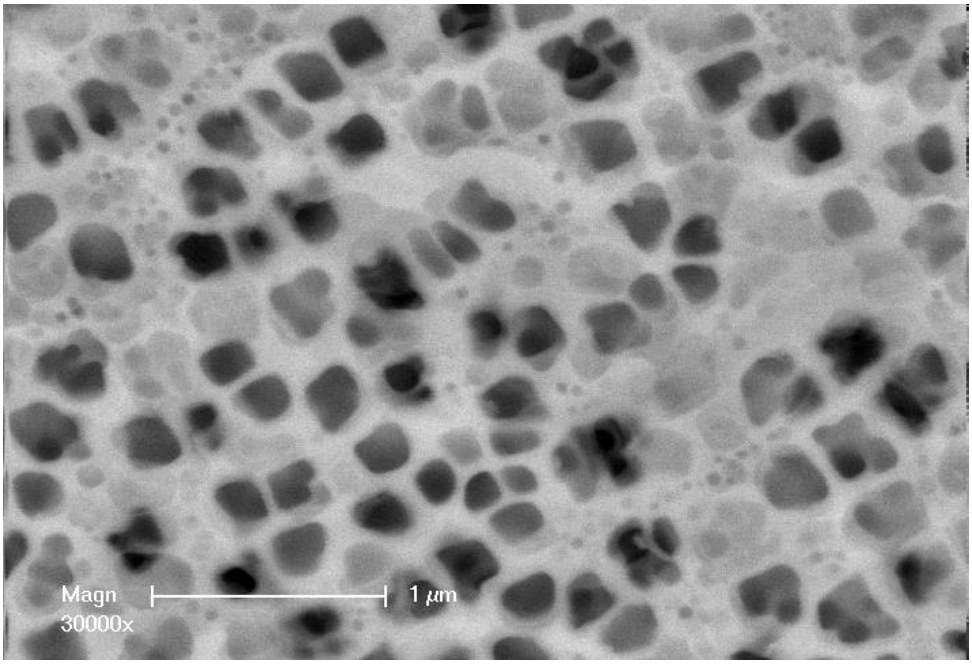

Figure 3.65. Formation of very fine precipitates in suction side, root section, trailing edge, hot surface.

Pressure side root section trailing edge outer side surface specimen microstructure is shown in Figure 3.66. In the center of the figure, precipitates look like seperated from a very big precipitate.

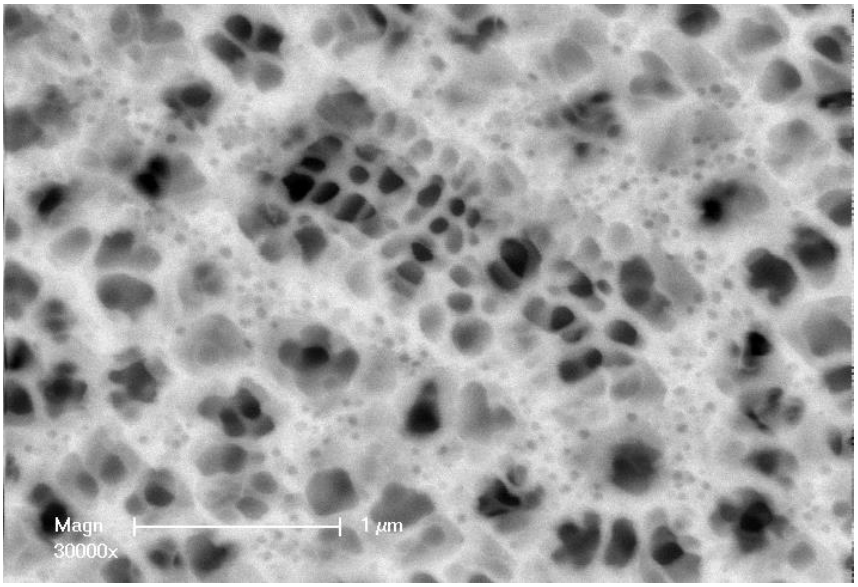

Figure 3.66. Microstructure in pressure side, root section, trailing edge, outer side surface specimen.

In Figure 3.67, precipitate microstructure of the firtree specimen is given. There are some very fine precipitates in the microstructure as seen in Figure 3.67.

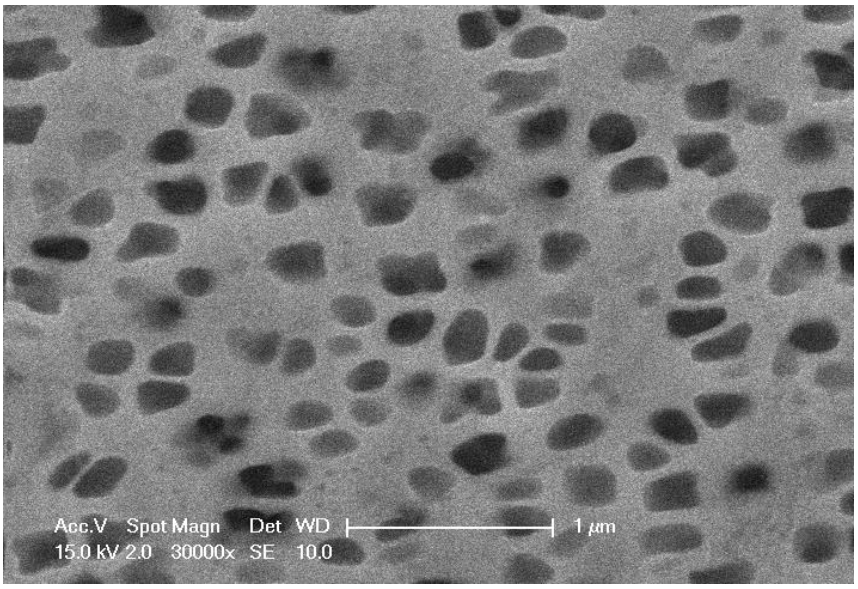

Figure 3.67. Microstructure in the firtree specimen.

3.3.3. Precipitate Area Fraction

Percentage values for precipitate area fraction are given in Table 3.6. Also, those values are given in a graphical form in Figure 3.68.

Area fraction in cold surfaces is generally larger than that in hot surfaces. While moving from the tip section to the root section, an increase is usually observed in the value of the area fraction.

Table 3.6. Precipitate area fraction vs. position.

Side →		Pressure				Suction		
Positions → / Sections ↓		Trailing edge	Middle	Leading edge	Stagnation	Leading edge	Middle	Trailing edge
Tip	Hot	39	34	34	38	31	35	29
	Cold	36	43	36	41	38	50	38
Middle	Hot	40	34	34	35	32	37	37
	Cold	42	43	35	34	39	44	48
Root	Hot	51	37	50	41	52	43	54
	Cold	48	35	50	47	46	48	53
Firtree		38						

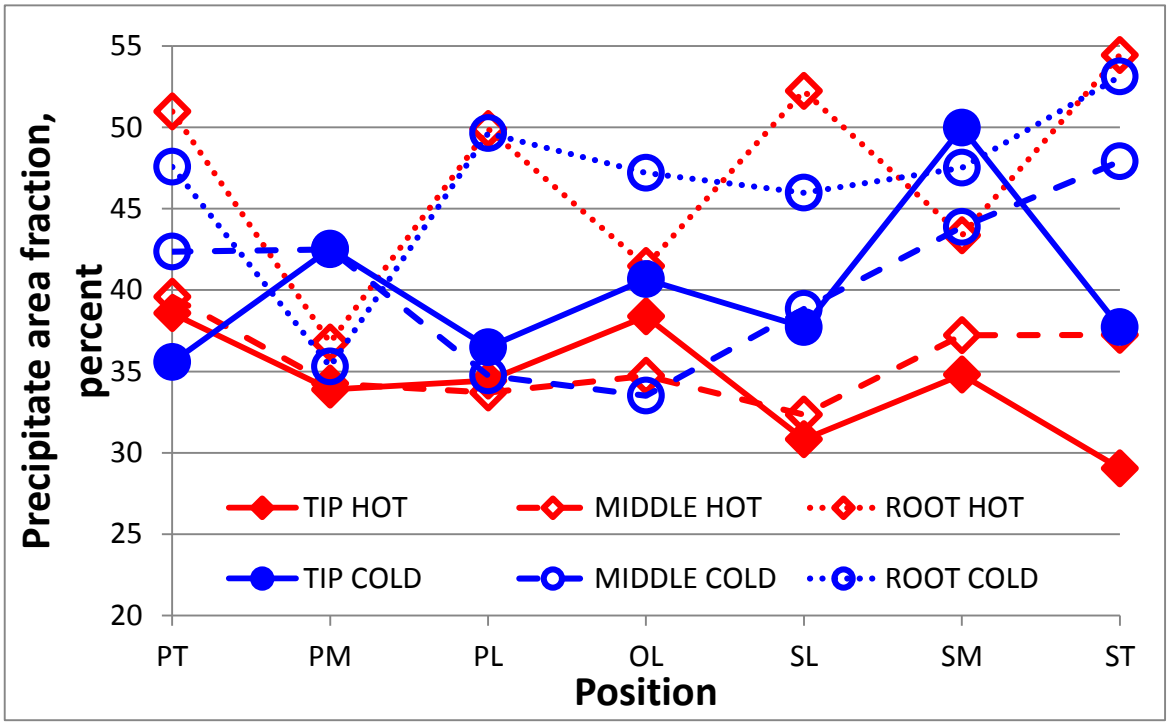

Figure 3.68. Precipitate area fraction vs. position.

4. DISCUSSION

Figure 4.1 gives the cross section of the unused (virgin) blade for the pressure side tip section. As mentioned in the section 3.2, grains in the z surface are usually elongated from the hot surface to the cold surface. Similarly, elongated grains are observed in Figure 4.1. Besides elongated ones, there are also equiaxed grains in the z surface of the virgin blade as seen in Figure 4.1.

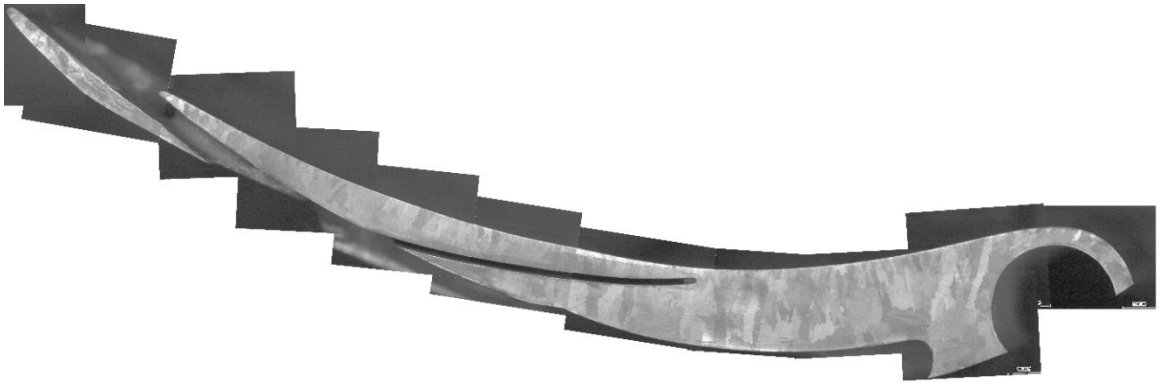

Figure 4.1. The cross section of the unused blade for the pressure side tip section.

Figure 4.2 shows the pressure side tip section leading edge position for the unused blade and gives the thickness of the base metal. When Figure 3.2 and Figure 4.2 are compared, it is seen that coating is not applied on the unused blade. The thicknesses of the base metal in both Figures 3.2 and 4.2 are almost the same and about 1.2-1.3 mm.

Figure 3.37c and Figure 4.2 show the same positions for the used and virgin blades, respectively. When these figures are compared, their grain morphologies are observed to be similar, since there are equiaxed and elongated grains together.

4.1. The Coatings

Coatings are required to protect the base metals from environmental degradation. Type of the applied coating shows variations with respect to the degradation process. These processes are Type II hot corrosion, Type I hot corrosion and high temperature oxidation.

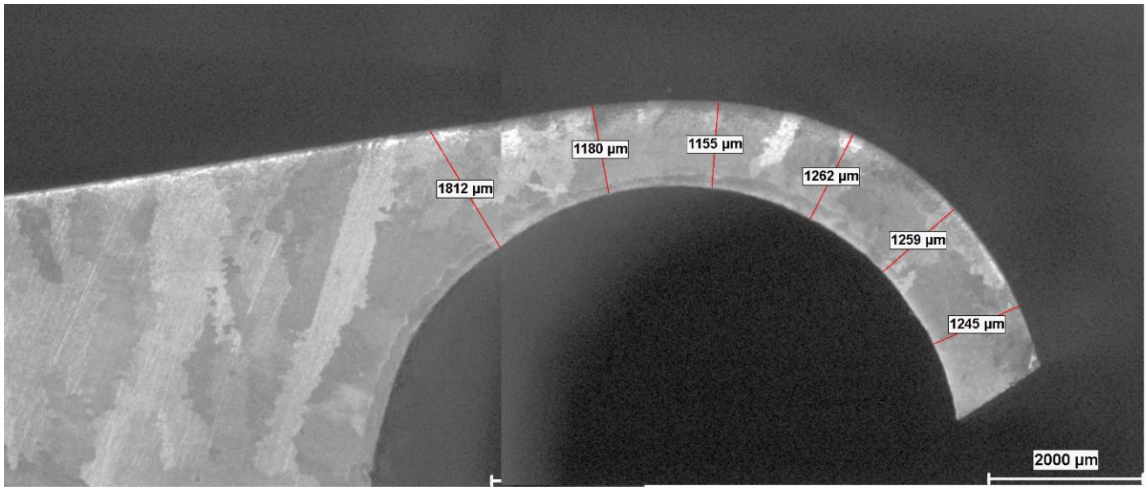

Figure 4.2. Base metal thickness in the pressure side tip section leading edge position for the unused blade.

Temperature interval for the Type II hot corrosion is about 600-850 °C [5, 33]. A certain value of partial pressure of sulphur trioxide forms and stabilizes base metal sulphates. These sulphates (ie, $NiSO_4$) and alkali metal sulphates (ie, Na_2SO_4) react and cause formation of compounds with low melting temperatures. These compounds do not allow protective oxide formation and cause Type II hot corrosion [5, 34, 35].

Temperature interval for the Type I hot corrosion is about 750-950 °C [5, 33]. Sulfur from a sulphatic deposit (ie, Na_2SO_4) diffuses inside, reacts with a stable sulphide former metal (ie, chromium), and moves through the preformed oxide layer. When chromium completely reacts with the sulfur diffusing inside, base metal sulphides find opportunity to form. Melting temperatures of these sulphides are about the temperature interval for the Type I hot corrosion [5, 34, 35].

Oxidation is observed for temperatures above 1000 °C. It is related to the speed of anion or cation transport through the crystal lattice or along the grain boundaries in the oxide. As a result, protective or nonprotective oxide scales form [5, 35]. For the temperatures greater than 850 °C, chromium oxide can dissociate to volatile CrO_3. As a result, amount of aluminum in superalloys is increased for oxidation protection [5].

NiCrAlY and NiCoCrAlY are used for oxidation protection, and also for Type I hot corrosion. However, CoCrAlY with high amounts of Cr are used for Type II hot corrosion

[5, 33]. It is understood from the data given in Table 3.1 that base metal of the investigated serviced turbine blade is coated with NiCoCrAlY having a thickness of 1600 microns in the suction side, root section, leading edge, z surface specimen. Then, a NiCrAlY coating with a thickness of 300 microns is applied. These coatings are possibly constructed for protection against Type I hot corrosion and oxidation. On top of these two overlay coatings, a 10-20 micron thick TBC layer is available as a thermal barrier. This layer actually contains NiAl and $NiAl_2$ intermetallic compositions in addition to possibly Al_2O_3 ceramic. The coatings mentioned as the first coating and the third coating in section 3.1 are transition layers.

Probably, the layer including the final point occured because of severe operating conditions. Precipitate free region formation in the matrix on the cooling channel surface was shown in Figure 3.14. This formation represents point 38 in Table 3.1. It is understood from Tables 3.2 and 3.3 that a chromia layer formed on the cooling channel surface. Figure 3.18 shows that diffusion of nickel from the cooling channel surface to the inner parts of the base metal occurs and this explains the formation of the precipitate free layer on the cooling channel surface. Figure 3.18 also shows that diffusion of chromium from the inner part of the base metal to the cooling channel surface occurred to form a chromia layer on the cooling channel surface. When Figures 3.3, 3.4 and 3.5 are compared, the chromia layer on the cooling channel surface is observed to be very thin in the root section and thicker in the tip and middle sections. This shows that temperature is higher in the tip and middle sections than in the root section.

High amounts of Cr (more than 40 wt %) was observed on the surface of the internal cooling channels as seen in Table 3.2. This high Cr layer can protect the cooled internal channels of the turbine blade against Type II hot corrosion.

4.2. Grain Size and Morphology

As already stated in the results section, grains in the cold surfaces are coarser than the grains in the hot surfaces. Morphology is equiaxed for both the hot and cold surfaces. Grains elongate from the hot surface to the cold surface.

High temperature and residual stress may give rise to recrystallization in metallic components. This can yield a refined grain structure. High temperature and plastic deformation are required conditions for recrystallization to occur [36, 37]. If recrystallization occurs during deformation, it is called dynamic recrystallization. Otherwise, recrystallization is static. Plastic deformation required for the formation of recrystallized grains may result from manufacturing and processing of components, and also from service conditions [38-41].

When superalloys are considered, solubility of the γ' phase has an important role in recrystallization. Cellular recrystallization occurs below the γ' solvus temperature. γ' precipitates make the movement of recrystallizing grain boundary difficult. Then, the grain boundary becomes supersaturated with elements that form γ'. Further movement of the recrystallizing grain boundary becomes impossible. Therefore, grain boundary leaves coarse columnar particles behind [37, 38, 42, 43]. Above the γ' solvus temperature, γ' free regions form and new grains form in those regions [37].

High temperature and stress result in formation of a γ' free layer on the surface. Oxidation is initiated due to high temperature. Precipitate former elements Al and Ti diffuse to the surface to form Al_2O_3 and TiO. These oxides take place in the oxide layer formed on the surface. As a result, almost all the precipitates close to the surface dissolve and a γ' free layer is formed [43]. Recrystallization starts on the surface and recrystallization grain boundary can easily move without the existence of the γ' phase [42].

Operations like shot peening and grit blasting result in plastic deformation on the surface [37, 38, 40]. Plastic deformation causes a large concentration of retained energy on the surface, then, recrystallized grains form during exposure to high temperature [40]. Increased temperature, increased stress, and increased duration of service result in an increased recrystallization depth on the surface [37, 38, 40, 44].

Higher strain rate results in a decrease in the recrystallization depth. When strain rate is high, dislocations have limited opportunity to rearrange themselves and move. As a result, formation of recrystallized grains becomes difficult [42].

In order to form a recrystallized grain on the surface, no new grain boundary interface energy is required. Therefore, formation of a recrystallized grain is expected on the surface rather than in the inner part. Higher energy is required to form a recrystallization grain in the inner part than on the surface [39, 42, 44].

Appropriate surface coatings provide protection against recrystallization in addition to hot corrosion and high temperature oxidation protection. Coatings prevent the formation of γ' free surface so that recrystallization during service is avoided [42, 44].

Wang et al. [45] observed grain recrystallization along grain boundaries and they explained this by dislocation activities. Rearrangement of dislocations give rise to formation of subgrains. Then, subgrain boundaries move, emit their dislocations to other grain boundaries and break to coalesce with an adjacent subgrain. If the size and misorientation of the new subgrain becomes more than a critical value, then it becomes a recrystallization nuclei.

Li et al. [41] have investigated geometric properties that may result in recrystallization. They modeled thermal and plastic stresses after investment casting and predicted high stress locations which are possible sources of recrystallization. The analysis suggests that high stress occurs at thin walled sections. Also, recrystallization tends to occur in thin parts of nonuniform cross sections. Therefore, components with uniform wall thickness prevents the recrystallization.

It should be reminded that hot surfaces showed lower grain size than the cold surfaces. However, grain growth is expected at high temperatures. Therefore, it is plausible to claim recrystallization in the serviced blade at hot and strained positions.

Recrystallization in the used blade analyzed in this study was observed more in the tip and middle sections than the root section. There was not a particular difference between the pressure and suction sides. Another observation is that recrystallization is observed more in the hot surface than in the cold surface. According to these observations, it can be said that stress and temperature affect the tip and middle sections more than the root

section. Recrystallized grains were available along the grain boundaries. Recrystallized grains indicated by white arrows can be seen in Figure 4.3.

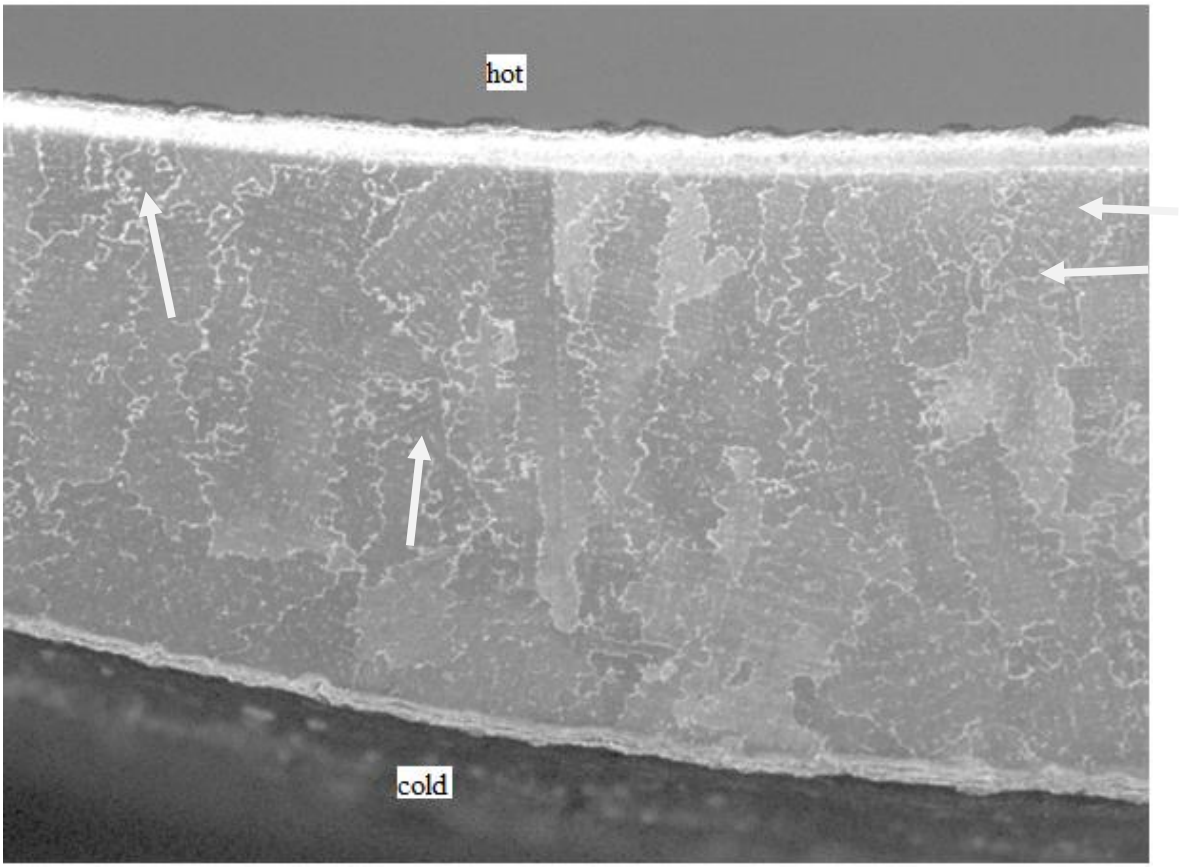

Figure 4.3. Recrystallization in the pressure side, tip section, middle position specimen for the used blade. Recrystallized grains are shown with white arrows.

Table 4.1 gives the grain size values for the used and unused blades in the pressure side tip section. When the grain size for the unused blade and used blade is compared, an increase is observed after the service for both the hot and cold surfaces of the pressure side leading edge, middle position, and trailing edge specimens. Increase in the grain size for the leading edge and middle positions is smaller than that in the trailing edge on the hot surface. This implies that recrystallization is more pronounced for the middle and leading edge positions than the trailing edge position in the tip section. It could be understood that stress and temperature more effectively act at the leading edge and middle position than the trailing edge in the tip section.

Table 4.1. The grain size values for the used and unused blades in the pressure side tip section.

Positions → / Blade ↓		Trailing edge	Middle	Leading edge
Used	Hot	514	554	469
	Cold	624	1060	715
Virgin	Hot	348	482	444
	Cold	566	634	518

It was observed that the grain size difference between the hot and cold surfaces is greater for the middle position specimens than the leading edge and trailing edge specimens. This is understood to be related with the distance between hot and cold surfaces at this position. This distance is small especially for the leading edge specimens and the size difference in this position is lower than the middle position. Thickness of the base metal for the serviced blade is given in Table 4.2. This thickness variation exist because of the thick coating in the leading edge and thin overall cross section in the trailing edge. The thickness of the virgin blade in Figure 4.1 was also measured. The thickness values are 1.1 mm in the pressure side trailing edge position, 4.1 mm in the pressure side middle position, 1.2 mm in the pressure side leading edge position, and 1.2 mm in the stagnation point.

Table 4.2. Thickness of the base metal in millimeters.

Side →	Pressure				Suction		
Positions → / Sections ↓	Trailing edge	Middle	Leading edge	Stagnation	Leading edge	Middle	Trailing edge
Tip	0.7	3.5	1.3	0.8	4.3	4.5	2
Middle	1.4	3.2	1.1	0.5	5.3	4.4	2.8
Root	2.4	4.8	1.8	1.3	6.5	4.8	2.4

4.3. Precipitate Size and Morphology

As mentioned before in section 3.3, the precipitate size for the hot surfaces is usually larger than that for the cold surfaces. Precipitate morphologies in Figures 3.61, 3.62, and 3.63 are given for the hot and cold surfaces in Table 4.3 and Table 4.4, respectively.

Miura et al. have conducted research [46] which is very similar to this current research. They have investigated precipitate morphology in specimens extracted from various regions of serviced single crystal nickel base superalloy turbine blades to determine the temperature and stress state along the blade.

Figures 4.4 and 4.5 show microstructure of the coating on the base metal in the stagnation point of the tip and middle sections, respectively. When these figures and those from the base metal shown in Figures 3.61 and 3.62 are compared, it is seen that number of raft regions is more in the coating than in the base metal. The coating decreases heat flux into the base metal and so prevents precipitate growth and rafting there. This explains the comparatively low precipitate size values in these sections in the base metal. Similarly, rafting was not observed in the pressure side tip section leading edge base metal specimen as seen in Figure 3.61; however, the raft was observed in the coating at this same position.

In the tip section, it is understood from precipitate size values in Figure 3.57, precipitate morphology in Table 4.3, and grain size values in Figure 3.29 that the pressure side specimens of the trailing edge and middle positions exposed to higher stress and temperature than the suction side specimens of the same positions. Also, high temperature and stress act at the tip section leading edge position. Precipitate size values in Figure 3.56 show that the temperature should be higher at the middle section leading edge position than the tip section leading edge position. However, the stress and temperature influence both in the pressure and suction sides of the trailing edge at the middle section is less than the tip section as understood from Figure 3.54. Pressure side trailing edge position is affected more by the temperature than the suction side trailing edge position in the middle section as seen in Figure 3.54. In both the pressure and suction sides of the middle section, temperature and stress should be higher in the middle position than the trailing edge position as seen Figure 3.58 and Table 4.3.

Table 4.3. Precipitate morphology on hot surface.

Side →	Pressure			Stagnation	Suction		
Positions → Sections ↓	Trailing edge	Middle	Leading edge		Leading edge	Middle	Trailing edge
Tip	▪ Deteriorated cuboidal ▪ 1 with **raft** ▪ 1 with very few raft	▪ Deteriorated cuboidal ▪ 3 with **raft** ▪ 1 with very few raft	▪ Cuboidal with no raft	▪ Deteriorated cuboidal with **raft**	▪ Deteriorated cuboidal with no raft	▪ 2 deteriorated cuboidal with **raft** ▪ 2 cuboidal with no raft	▪ 1 deteriorated cuboidal with **raft** ▪ 1 deteriorated cuboidal with no raft ▪ 2 cuboidal with no raft
Middle	▪ 1 deteriorated cuboidal and cuboidal with no raft ▪ 1 triangular and deteriorated cuboidal with no raft	▪ 4 deteriorated cuboidal with **raft**	▪ Deteriorated cuboidal with **raft**	▪ Deteriorated cuboidal with **raft**	▪ Deteriorated cuboidal with **raft**	▪ 2 deteriorated cuboidal with **raft** ▪ 1 deteriorated cuboidal with no raft ▪ 1 cuboidal with no raft	▪ 2 cuboidal with no raft ▪ 1 deteriorated cuboidal and triangular with no raft
Root	▪ Cuboidal with no fine precipitates	▪ 2 cuboidal with no fine precipitates	▪ Cuboidal with no fine precipitates	▪ Cuboidal with no fine precipitates	▪ Cuboidal with no fine precipitates	▪ 2 cuboidal with no fine precipitates	▪ 2 cuboidal with **fine precipitates** ▪ 1 cuboidal with no fine precipitates

Table 4.4. Precipitate morphology on cold surface.

Side →	Pressure			Stagnation	Suction		
Positions → Sections ↓	Trailing edge	Middle	Leading edge		Leading edge	Middle	Trailing edge
Tip	▪ 1 deteriorated cuboidal with **raft** ▪ 1 deteriorated cuboidal with very few raft	▪ 2 cuboidal with no raft ▪ 2 deteriorated cuboidal and triangular with no raft	▪ Cuboidal and deteriorated cuboidal with no raft	▪ Cuboidal with no raft	▪ Cuboidal with no raft	▪ 3 cuboidal with no raft ▪ 1 deteriorated cuboidal and cuboidal with no raft	▪ 1 cuboidal with no raft ▪ 1 deteriorated cuboidal with no raft ▪ 1 deteriorated cuboidal with **raft**
Middle	▪ 1 cuboidal with no raft ▪ 1 cuboidal and triangular with no raft	▪ 4 cuboidal with no raft	▪ Deteriorated cuboidal with **raft**	▪ Deteriorated cuboidal with **raft**	▪ Deteriorated cuboidal with very few **raft**	▪ 4 cuboidal with no raft	▪ 1 deteriorated cuboidal and triangular with no raft ▪ 1 deteriorated cuboidal with no raft ▪ 1 cuboidal with no raft
Root	▪ Deteriorated cuboidal with **fine precipitates**	▪ Deteriorated cuboidal with **fine precipitates**	▪ Cuboidal with **fine precipitates**	▪ Cuboidal with **fine precipitates**	▪ Cuboidal with **fine precipitates**	▪ Deteriorated cuboidal with **fine precipitates**	▪ Deteriorated cuboidal with **fine precipitates**

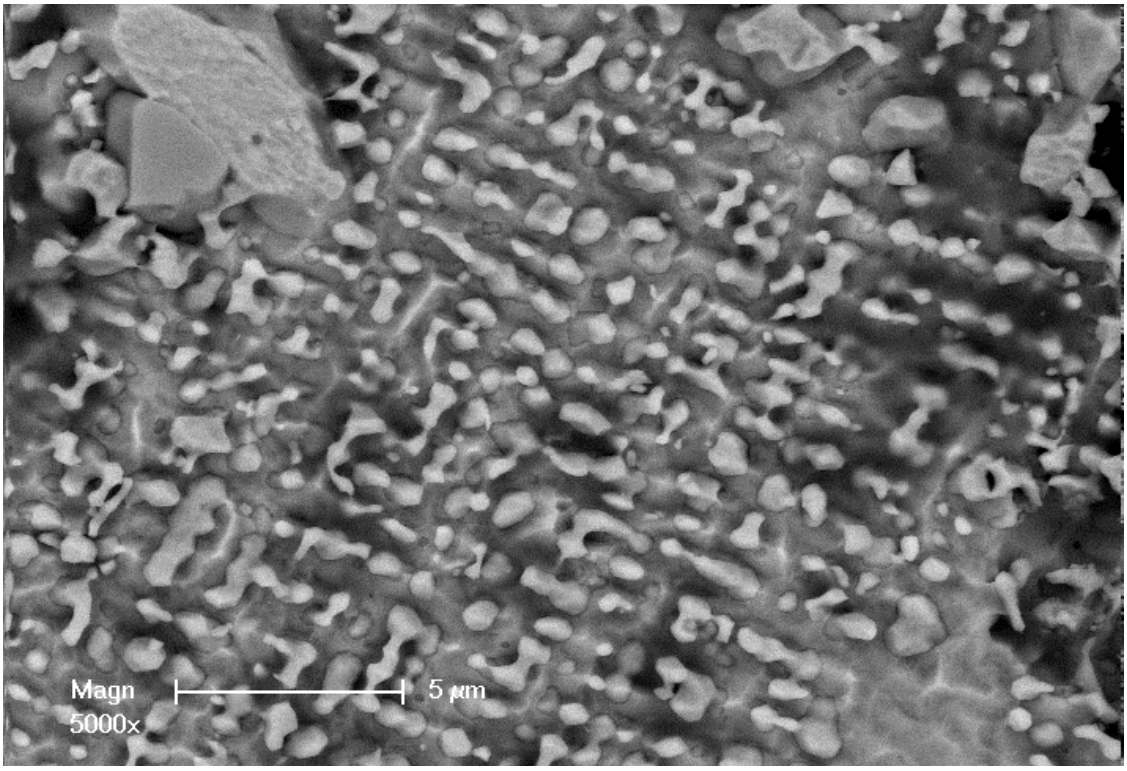

Figure 4.4. Microstructure of the coating on the base metal in the stagnation point tip section.

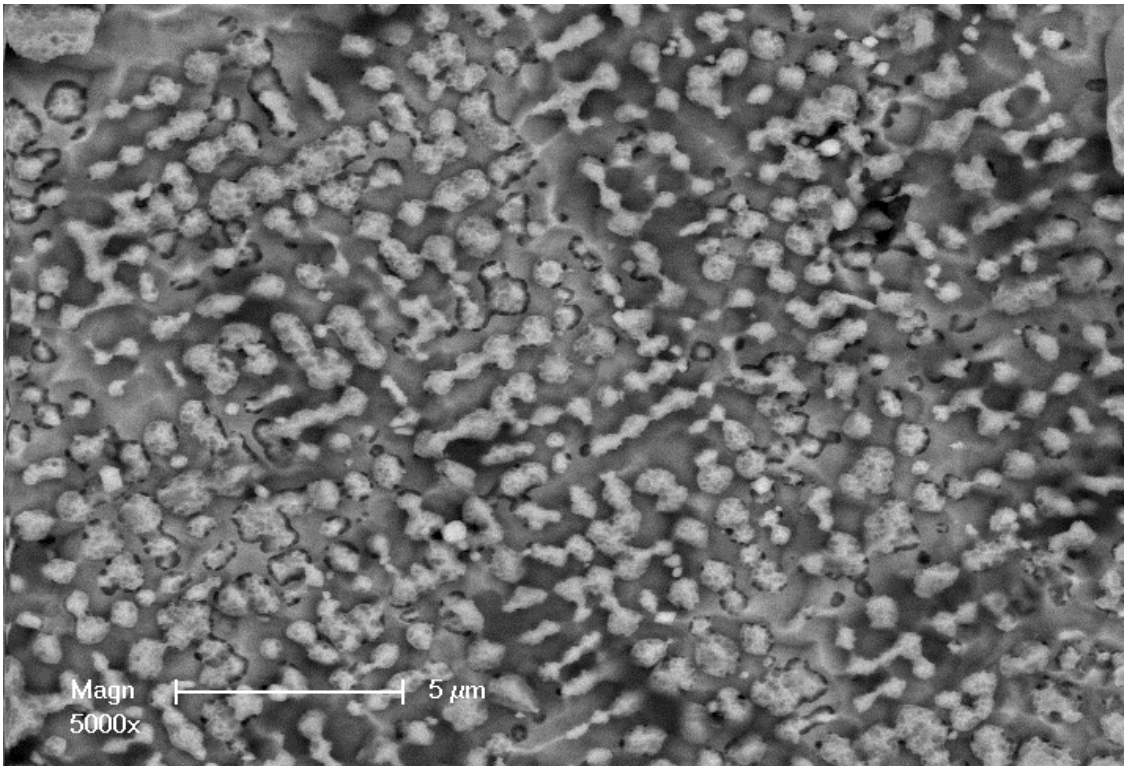

Figure 4.5. Microstructure of the coating on the base metal in the stagnation point middle section.

In the leading edge positions of all sections, precipitate size difference between the hot and cold surfaces is higher in the suction side than the pressure side and the stagnation point. The distance between the analysis points in the suction side is greater than that in the pressure side and stagnation point as seen in Table 4.2.

In the root section, no raft formation was observed and precipitate size is smaller than the tip and middle sections. Temperature and stress in this section are obviously less than those in the tip and middle sections. Additionally, formation of very fine precipitates was observed at the cold surfaces in this section and examples were given in Figures 3.64 and 3.65. These fine precipitates show such a distribution as shown in Figure 4.6.

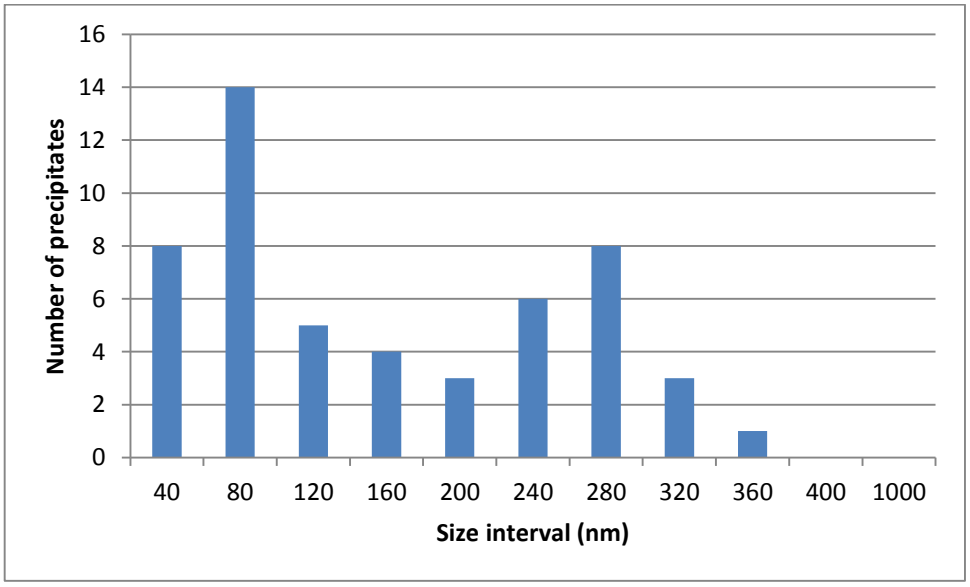

Figure 4.6. Precipitate size distribution in the pressure side root section leading edge cold surface specimen.

Formation of very fine precipitates is usually attributed to cooling from the aging temperature. During aging, precipitates grow and the distance between them increases. When cooling occurs, matrix supersaturation increases. As a result, precipitates form in the matrix due to the increased diffusion distance [47-51]. However, contradictory to this explanation, fine precipitates may form isothermally [52]. During isothermal aging, precipitates reach a critical size. Since strain energy due to mismatch becomes very large, precipitate is not able to grow further and begin to dissolve. Matrix becomes supersaturated

after a while because of this dissolution. This supersaturation in the matrix results in formation of fine precipitates [52-54].

SEM photographs from the cross section of the virgin blade shown in Figure 4.1 were also obtained in order to observe the precipitate morphology. The morphology was observed to be independent of position and one representative picture is given in Figure 4.7. Formation of the very fine precipitates was not observed in the virgin blade.

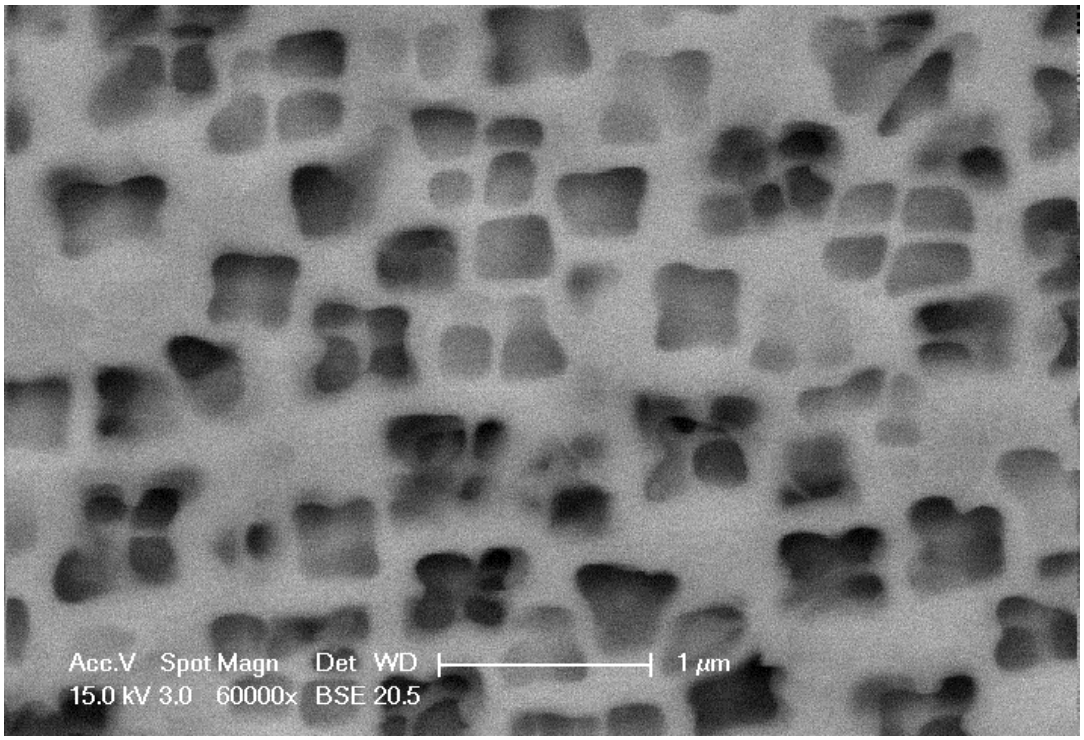

Figure 4.7. Precipitate morphology in the virgin blade.

Size analysis for precipitates was also completed on the virgin blade. Analysis gives the average precipitate diameter as 244 nm, as mentioned before. This size value is lower than that for the hot and cold surface values both in the tip and middle sections. However, it is larger than that for the hot and cold surface values in the root section. This could be because of the inclusion of the very fine precipitates of the root section in the size analysis so that size value in the virgin blade is higher than that in the root section. The precipitate size in the firtree (179 nm) is smaller than that in the virgin blade. It is seen in Figure 3.67 that there are some fine precipitates in the firtree position. Due to these fine precipitates, average precipitate diameter in the firtree position could be smaller than that in the virgin blade.

5. CONCLUSION

Superalloys have good creep resistance and high temperature strength. Thanks to these properties, superalloys are used in many industries such as gas turbine industry, aircrafts and space vehicles. IN738LC is a polycrystalline nickel base superalloy with good creep strength and hot corrosion resistance. Specimens from an IN738LC turbine blade which has serviced 80000 hours in the first stage of the hot section in an electricity producing natural gas turbine were extracted. Morphology and size for the precipitates and grains were analyzed. According to variations in the microstructure, high/low stress/temperature positions were predicted. Following results are drawn from the current research:

- Base metal of the turbine blade was firstly coated with a NiCoCrAlY layer. Then, a NiCrAlY layer was applied. Finally, a TBC was available on the NiCrAlY coating.
- The grain size in the cold surfaces was observed to be larger than that in the hot surfaces. It was understood that recrystallization occured in the hot surfaces.
- Precipitate size in the hot surfaces is larger than that in the cold surfaces.
- In the tip section, raft was observed in both the suction and pressure sides of the trailing edge and middle positions, and in the stagnation point. In the middle section, raft was observed in both the suction and pressure sides of the leading edge and middle positions, and in the stagnation point. These raft points can be associated with high stress/strain.
- Precipitate size in the root section is smaller than that in the tip and middle sections. No raft formation was observed in the root section. Among the three sections, root section is the one exposed least to temperature and stress.
- Formation of very fine precipitates was observed in the root section cold surfaces.
- Temperature and stress in the leading edge are predicted to be higher in the middle section than in the tip section. However, temperature and stress in the trailing edge are higher in the tip section than in the middle section. For the trailing edge and middle positions of the tip and middle sections, stress and temperature are higher in the pressure side than those in the suction side.

6. FUTURE WORK

Some suggestions for future work and improving the current research are given as follows:

- Locally adjusted composition by additive manufacturing can be accomplished.
- Better coatings can be designed to reduce the temperature on the blade.
- Hot corrosion and corrosion studies can be performed assess their influence on the blade life.
- Blades with other service times can be examined for creep life predictions.

REFERENCES

1. Reed, R.C., *The Superalloys-Fundamentals and Applications*, Cambridge University Press, New York, 2006.

2. Sims, C. T., and W. C. Hagel (editors), *The Superalloys*, Wiley-Interscience, New York, 1972.

3. Singh, K., "Advanced Materials for Land Based Gas Turbines", *Transactions of the Indian Institute of Metals*, Vol. 67, Issue 5, pp. 601-615, 2014.

4. Benini E. (editor), *Advances in Gas Turbine Technology*, InTech, Rijeka, 2011.

5. Pomeroy, M. J., "Coatings for Gas Turbine Materials and Long Term Stability Issues", *Materials and Design*, Vol. 26, pp. 223-231, 2005.

6. Sims, C. T., N. S. Stoloff, and W.C. Hagel (editors), *Superalloys II – High-Temperature Materials for Aerospace and Industrial Power*, John Wiley & Sons, Inc., USA, 1987.

7. Goward, G. W., "Progress in Coatings for Gas Turbine Airfoils", *Surface and Coatings Technology*, Vols. 108-109, pp. 73-79, 1998.

8. Gurrappa, I., "Identification of Hot Corrosion Resistant MCrAlY Based Bond Coatings for Gas Turbine Engine Applications", *Surface and Coatings Technology*, Vol 139, pp. 272-283, 2001.

9. Konter, M., and M. Thumann, "Materials and Manufacturing of Advanced Industrial Gas Turbine Components", *Journal of Materials Processing Technology*, Vol. 117, pp. 386-390, 2001.

10. Gurrappa, I., and A. Sambasiva Rao, “Thermal Barrier Coatings for Enhanced Efficiency of Gas Turbine Engines”, *Surface and Coatings Technology*, Vol. 201, pp. 3016-3029, 2006.

11. Sato, J., T. Omori, K. Oikawa, I. Ohnuma, R. Kainuma, and K. Ishida, “Cobalt-Base High-Temperature Alloys”, *Science*, Vol. 312, pp. 90-91, 2006.

12. Bauer, A., S. Neumeier, F. Pyczak, and M. Goken, “Microstructure and Creep Strength of Different γ/γ’-Strengthened Co-Base Superalloy Variants”, *Scripta Materialia*, Vol. 63, pp. 1197-1200, 2010.

13. Bauer, A., S. Neumeier, F. Pyczak, R. F. Singer, and M. Goken, “Creep Properties of Different γ’-Strengthened Co-Base Superalloys”, *Materials Science and Emgineering A*, Vol. 550, pp. 333-341, 2012.

14. Yan, H. Y., V. A. Vorontsov, and D. Dye, “Alloying Effects in Polycrystalline γ’ Strengthened Co-Al-W Base Alloys”, *Intermetallics*, Vol. 48, pp. 44-53, 2014.

15. Titus, M. S., A. Suzuki, and T. M. Pollock, “Creep and Directional Coarsening in Single Crystals of New γ-γ’ Cobalt-Base Alloys”, *Scripta Materialia*, Vol. 66, pp. 574-577, 2012.

16. Pollock, T. M., J. Dibbern, M. Tsunekane, J. Zhu, and A. Suzuki, “New Co-Based γ-γ’ High-Temperature Alloys”, *The Journal of the Minerals, Metals and Materials Society*, Vol. 62, Issue 1, pp. 58-63, 2010.

17. Pollock, T. M., and S. Tin, “Nickel-Based Superalloys for Advanced Turbine Engines: Chemistry, Microstructure, and Properties”, *Journal of Propulsion and Power*, Vol. 22, Issue 2, pp. 361-374, 2006.

18. Porter, D. A., and K. E. Easterling, *Phase Transformations in Metals and Alloys*, second edition, Chapman & Hall, London, 1992.

19. Ricks, R. A., A. J. Porter, and R. C. Ecob, “The Growth of γ’ Precipitates in Nickel-Base Superalloys”, *Acta Metallurgica*, Vol. 31, Issue 1, pp. 43-53, 1983.

20. Lifshitz, I. M., and V. V. Sloyozov, “The Kinetics of Precipitation from Supersaturated Solid Solutions”, *Journal of Physics and Chemistry of Solids*, Vol. 19, Issue 1-2, pp. 35-50, 1961.

21. Wagner, C., “Theorie der Alterung von Niederschlagen durch Umlosen (Ostwald-Reifung)”, *Zeitschrift für Elektrochemie*, Vol. 65, Issue 7-8, pp. 581-591, 1961.

22. Tian, S. G., H. H. Zhou, J. H. Zhang, H. C. Yang, Y. B. Xu, and Z. Q. Hu, “Directional Coarsening of γ’ Phase in Single Crystal Nickel Based Superalloys during Tensile Creep”, *Materials Science and Technology*, Vol. 16, Issue 4, pp. 451-456, 2000.

23. Sugui, T., Z. Shu, L. Fushun, L. Anan, and L. Jingjing, “Microstructure Evolution and Analysis of a Single Crystal Nickel-Based Superalloy during Compressive Creep”, *Materials Science and Emgineering A*, Vol. 528, pp. 4988-4993, 2011.

24. Zhao, K., Y. H. Ma, L. H. Lou, and Z. Q. Hu, “Directional Coarsening of γ’ Phase Induced by Phase Transformation Stress”, *Journal of Materials Research*, Vol. 20, Issue 9, 2005.

25. Ratel, N., G. Bruno, P. Bastie, and T. Mori, “Plastic Strain-Induced Rafting of γ’ Precipitates in Ni Superalloys: Elasticity Analysis”, *Acta Materialia*, Vol. 54, pp. 5087-5093, 2006.

26. Zhou, N., C. Shen, P. M. Sarosi, M. J. Mills, T. Pollock, and Y. Wang, “γ’ Rafting in Single Crystal Blade Alloys: a Simulation Study”, *Materials Science and Technology*, Vol. 25, Issue 2, pp. 205-212, 2009.

27. Epishin, A., T. Link, H. Klingelhoffer, B. Fedelich, U. Bruckner, and P. D. Portella, “New Teechnique for Characterization of Microstructural Degradation under Creep:

Application to the Nickel-Base Superalloy CMSX-4", *Materials Science and Emgineering A*, Vols. 510-511, pp. 262-265, 2009.

28. Yang, J. X., Q. Zheng, X. F. Sun, H. R. Guan, and Z. Q. Hu, "Morphological Evolution of γ' Phase in K465 Superalloy during Prolonged Aging", *Materials Science and Emgineering A*, Vol. 457, pp. 148-155, 2007.

29. Ratel, N., H. A. Calderon, T. Mori, and P. J. Withers, "Predicting the Onset of Rafting of γ' Precipitates by Channel Deformation in a Ni Superalloy", *Philosophical Magazine*, Vol. 90, Issue 5, pp. 585-597, 2010.

30. Touratier, F., E. Andrieu, D. Poquillon, and B. Viguier, "Rafting Microstructure during Creep of the MC2 Nickel-Based Superalloy at very High Temperature", *Materials Science and Emgineering A*, Vols. 510-511, pp. 244-249, 2009.

31. Altincekic, A., *Evolution of Precipitate Microstructure in the Superalloy IN738LC during Compression Creep*, M. Sc. Thesis, Boğaziçi University, 2011.

32. Rasband, W. S., *ImageJ*, 1997, http://rsb.info.nih.gov/ij/, accessed at May 2016.

33. Nicholls, J. R., N. J. Simms, W. Y. Chan, and H. E. Evans, "Smart Overlay Coatings-Concept and Practice", *Surface and Coatings Technology*, Vol. 149, pp. 236-244, 2001.

34. Khajavi, M. R., and M. H. Shariat, "Failure of First Stage Gas Turbine Blades", *Engineering Failure Analysis*, Vol. 11, pp. 589-597, 2004.

35. Bernstein, H. L., "High Temperature Coatings for Industrial Gas Turbine Users", TAMU, *Proceedings of the 28th Turbomachinery Symposium*, Texas, USA, 1999, TAMU, USA, 1999.

36. Doherty, R. D., D. A. Hughes, F. J. Humphreys, J. J. Jonas, D. Juul Jensen, M. E. Kassner, W. E. King, T. R. McNelley, H. J. McQueen, and A. D. Rollett, "Current

Issues in Recrystallization: a Review", *Materials Science and Emgineering A*, Vol. 238, pp. 219-274, 1997.

37. He, Y. H., X. Q. Hou, C. H. Tao, and F. K. Han, "Recrystallization and Fatigue Fracture of Single Crystal Turbine Blades", *Engineering Failure Analysis*, Vol. 18, pp. 944-949, 2011.

38. Zhang, B., C. H. Tao, X. Lu, C. K. Liu, C. Y. Hu, and M. Y. Bai, "Recrystallization of Single Crystal Nickel-Based Superalloy", *Journal of Iron and Steel Research, International*, Vol. 16, Issue 6, pp. 75-79, 2009.

39. Burgel, R., P. D. Portella, and J. Preuhs, "Recrystallization in Single Crystals of Nickel Base Superalloys", TMS, 9th International Symposium on Superalloys, Pennsylvania, USA, September 17-21, 2000, TMS, USA, 2000.

40. Jichun, X., L. Jiarong, and L. Shizhong, "Surface Recrystallization in Nickel Base Single Crystal Superalloy DD6", *Chinese Journal of Aeronautics*, Vol. 23, pp. 478-485, 2010.

41. Zhonglin, L., X. Jichun, X. Qingyan, L. Jiarong, and L. Baicheng, "Deformation and Recrystallization of Single Crystal Nickel-Based Superalloys during Investment Casting" *Journal of Materials Processing Technology*, Vol. 217, pp. 1-12, 2015.

42. Zhang, B., C. K. Liu, J. Y. Zhou, and C. H. Tao, "Dynamic Recrystallization of Single-Crystal Nickel-Based Superalloy", *Transactions of Nonferrous Metals Society of China*, Vol. 24, pp. 1744-1749, 2014.

43. Xie, G., J. Zhang, and L. H. Lou, "Effect of Heat Treatment Atmosphere on Surface Recrystallization of a Directionally Solidified Ni-Base Superalloy", *Scripta Materialia*, Vol. 59, pp. 858-861, 2008.

44. Li, Y., C. Tao, and W. Zhang, "Dynamic Recrystallization Behavior of a Directionally Solidified Superalloy", *Advanced Engineering Materials*, Vol. 9, Issue 10, pp. 867-871, 2007.

45. Wang, S., L. Wang, Y. Liu, G. Xu, B. Zhang, and G. Zhao, "Nucleation Mechanism of a Nickel-Base Superalloy during Dynamic Recrystallization", *Acta Metallurgica Sinica*, Vol. 24, Issue 4, pp. 295-300, 2011.

46. Miura, N., K. Nakata, M. Miyazaki, Y. Hayashi, and Y. Kondo, "Morphology of γ' Precipitates in Second Stage High Pressure Turbine Blade of Single Crystal Nickel-Based Superalloy after Serviced", *Materials Science Forum*, Vols. 638-642, pp. 2291-2296, 2010.

47. Behrouzghaemia, S., and R. J. Mitchell, "Morphological Changes of γ' Precipitates in Superalloy IN738LC at Various Cooling Rates", *Materials Science and Emgineering A*, Vol. 498, pp. 266-271, 2008.

48. Mitchell, R. J., M. Preuss, M. C. Hardy, and S. Tin, "Influence of Composition and Cooling Rate on Constrained and Unconstrained Lattice Parameters in Advanced Polycrystalline Nickel–Base Superalloys", *Materials Science and Emgineering A*, Vol. 423, pp. 282-291, 2006.

49. Mitchell, R. J., and M. Preuss, "Inter-Relationships between Composition, γ' Morphology, Hardness, and γ-γ' Mismatch in Advanced Polycrystalline Nickel-Base Superalloys during Aging at 800 °C", *Metallurgical and Materials Transactions A*, Vol. 38A, pp. 615-627, 2007.

50. Mao, J., K. Chang, W. Yang, K. Ray, S. P. Vaze, and D. U. Furrer, "Cooling Precipitation and Strengthening Study in Powder Metallurgy Superalloy U720LI", *Metallurgical and Materials Transactions A*, Vol. 32A, pp. 2441-2452, 2001.

51. Sarosi, P. M., B. Wang, J. P. Simmons, Y. Wang, and M. J. Mills, "Formation of Multimodal Size Distributions of γ' in a Nickel-Base Superalloy during Interrupted Continuous Cooling", *Scripta Materialia*, Vol. 57, pp. 767-770, 2007.

52. Balikci, E., and D. Erdeniz, "Multimodal Precipitation in the Superalloy IN738LC", *Metallurgical and Materials Transactions A*, Vol. 41A, pp. 1391-1398, 2010.

53. Balikci, E., R. A. Mirshams, and A. Raman, "Microstructure Evolution in Polycrystalline IN738LC in the Range 1120 to 1250 °C", *Zeitschrift für Metallkunde*, Vol. 90, Issue 2, pp. 132-140, 1999.

54. Balikci, E., and A. Raman, "Characteristics of the γ' Precipitates at High Temperatures in Ni-Base Polycrystalline Superalloy IN738LC", *Journal of Materials Science*, Vol. 35, pp. 3593-3597, 2000.